Development of novel metrology methods for time domain THz spectroscopy systems

by

Fatemeh AMIRKHAN

MANUSCRIPT-BASED THESIS PRESENTED TO ÉCOLE DE TECHNOLOGIE SUPÉRIEURE IN PARTIAL FULFILLMENT FOR THE DEGREE OF DOCTOR OF PHILOSOPHY
Ph.D.

MONTREAL, DECEMBER, 14, 2021

ÉCOLE DE TECHNOLOGIE SUPÉRIEURE
UNIVERSITÉ DU QUÉBEC

BOARD OF EXAMINERS

THIS THESIS HAS BEEN EVALUATED

BY THE FOLLOWING BOARD OF EXAMINERS

Dr. François Blanchard, Thesis supervisor
Department of Electrical Engineering, École de Technologie Supérieure

Dr. Tsuneyuki Ozaki, co-Supervisor
Institut national de la recherche scientifique-Centre Énergie Matériaux Télécommunications.

Dr. Claudiane Ouellette-Plamondon, President of the board of examiners
Department of Construction Engineering , École de Technologie Supérieure

Dr. Bora Ung, Member of the jury
Department of Electrical Engineering, École de Technologie Supérieure

Dr. Denis Seletskiy, External examiner
Department of Engineering Physics, Polytechnique Montréal

THIS THESIS WAS PRESENTED AND DEFENDED

IN THE PRESENCE OF A BOARD OF EXAMINERS AND THE PUBLIC

ON DECEMBER, 1, 2021

AT ÉCOLE DE TECHNOLOGIE SUPÉRIEURE

ACKNOWLEDGEMENTS

I have had the pleasure of meeting and working with many people during my time at the École de technologie supérieure, and I would like to express my deep and sincere gratitude to all of them.

I am very grateful to my PhD supervisor, Professor François Blanchard, for all his support and advice over the past five years, through his countless hours of guidance and help in the lab, in his office, and during the gathering at lunchtime. He was always willing to help with experiments and give advice. Discussions with Prof. Blanchard were always enthusiastic, interesting, and fruitful, and I have benefited both scientifically and personally. Prof. Blanchard has also provided several opportunities for me, including collaboration with other research groups and attendance at both internal and international conferences. It was a pleasure to work with him and learn about terahertz research from him.

Similarly, I would like to thank my co-supervisor, Professor Tsuneyuki Ozaki, for his support and help during my PhD study. I found that the discussions with Prof. Ozaki were always encouraging, interesting and effective. I am really grateful for all his insightful comments on my papers or my work. I would also like to thank him for his help in giving me an opportunity to attend an international conference.

I would also like to thank my colleague Dr. Xavier Ropagnol for his support during my PhD. He has expertise in the terahertz source (antenna), and I have benefited from that. Thanks to him for being there to answer my questions and advise me.

I'm also very grateful to all my colleagues from the research group for their help and collaboration. In particular, Alexandre Robichaud and Mathieu Gratuze for providing their devices (i.e., PMUT array and PM device) and their help and collaboration.

Special thanks to my examiners: Prof. Bora Ung, Prof. Denis Seletskiy, and the president, Prof. Claudiane Ouellet-Plamondon. Thanks for reviewing and evaluating my thesis. I would like to thank to Dr. Richard Cooper for the English revision of this thesis.

A special acknowledgment to Mr. Prasun Lala from Sara writing group at ETS for all his thoughtful and positive feedback and his time during my PhD.

I would like to dedicate this thesis to my parents, Shekoufeh and Ismaeil. My dad will always be in my memory. I would like to thank my mom for all her support during this stage of my life. This was simply not possible without her encouragement and unconditional love. Thank you very much, mom, for all of your love.

Développement de nouvelles méthodes de métrologie pour système de spectroscopie THz dans le domaine du temps

Fatemeh AMIRKHAN

RÉSUMÉ

Le système de spectroscopie temporelle térahertz (THz) est un outil puissant car il utilise les propriétés des ondes THz de manière unique pour les technologies de spectroscopie et d'imagerie dans une grande variété d'applications, telles que la science des matériaux, l'ingénierie, la médecine et la chimie. La gamme de fréquences THz se situe entre les bandes micro-ondes et infrarouges du spectre électromagnétique (EM) (c'est-à-dire entre 0,1 THz et 10 THz), ce qui relie la partie électronique du spectre à la partie photonique. Par rapport aux fréquences infrarouges, les fréquences THz peuvent pénétrer les matériaux non métalliques et non polaires avec une énergie suffisamment faible, insuffisante pour ioniser les atomes ou les molécules. En outre, le système THz-TDS peut être utilisé pour mesurer non seulement l'intensité d'une impulsion spectrale, mais aussi le champ électrique transitoire associé, fournissant une méthode de mesure unique pour calculer facilement l'amplitude et la phase d'une impulsion à partir du champ électrique THz mesuré.

Au cours des 30 dernières années, les performances des systèmes de détection THz ont été considérablement améliorées. Cependant, pour faire passer la spectroscopie et l'imagerie THz d'une technique à l'échelle du laboratoire à un outil polyvalent aux nombreuses applications pratiques, des développements techniques sont encore nécessaires au niveau des sources et des détecteurs. Par conséquent, de nombreux scientifiques travaillent actuellement à l'amélioration des sources et des détecteurs THz avec des caractéristiques améliorées, ce qui implique généralement l'utilisation de nouveaux matériaux, méthodes et techniques pour améliorer ces technologies. Cette exigence essentielle motive le sujet de ma thèse : développer de nouvelles méthodes pour améliorer la sensibilité de détection du système THz.

Ce travail vise à contribuer au développement et à l'avancement des connaissances dans le domaine de la technologie de détection THz. En particulier, ce travail se concentre sur la détection THz dans le système THz-TDS. Pour ce faire, une revue de la littérature est d'abord présentée. Elle couvre les propriétés de la fréquence THz et du système THz-TDS, leur génération et leur détection, ainsi que leurs applications.

Suite à cette revue de la littérature, nous présentons une nouvelle méthode de caractérisation des matériaux électro-optiques (EO) en couches minces à l'aide d'un métamatériau (c'est-à-dire un résonateur à anneau divisé (SRR)) et d'une microscopie en champ proche THz intense. La méthode est basée sur la simulation et l'étude analytique de la résolution d'imagerie en champ proche des distributions de champ électrique et magnétique du SRR, qui est conçu pour la gamme de fréquences THz. Le principal avantage de cette méthode est que l'on peut utiliser une électrode sans contact (c'est-à-dire le SRR) dans l'expérience pour caractériser un matériau de film mince inconnu, puis comparer le résultat avec les résultats de simulation fournis dans notre approche.

Nous présentons ensuite une technique simple en testant un nouveau dispositif dans le système THz-TDS qui fournit une onde THz dérivée du temps. Ce dispositif est un réseau de transducteurs ultrasoniques micro-usinés piézoélectriques (PMUT) qui différencie une impulsion THz en effectuant des variations temporelles (à l'échelle de la femtoseconde) dans le trajet du faisceau THz. Le signal THz modulé détecté après le dispositif piézoélectrique est proportionnel à la dérivée de premier ordre de l'impulsion THz. Cette présentation est couplée à la présentation de la caractérisation, des performances de ce dispositif et de sa limitation en tant que modulateur THz. Cette étude permet de comprendre le principe d'utilisation de ce dispositif comme modulateur THz afin d'accroître les connaissances pour choisir ce type de dispositif avec de meilleures performances.

Suite à cette présentation, nous avons testé un autre dispositif ayant les mêmes propriétés que le précédent, mais avec des dimensions et un mouvement plus importants pour améliorer la dérivation des ondes THz. Il s'agit d'un dispositif piézoélectrique micro-usiné (PM), qui est inséré dans le trajet du faisceau THz. Il fournit une modulation de référence pour l'unité de détection à verrouillage, qui à son tour donne accès à l'information dérivée du quatrième ordre du signal THz entrant. Il convient de noter que l'intégration du signal dérivé enregistré conduit à un signal de référence récupéré avec un rapport signal/bruit (SNR) équivalent ou même meilleur, ouvrant la porte à un nouveau type de mesure THz hautement sensible dans le domaine temporel.

Enfin, il y a une conclusion à l'ensemble du travail fourni dans ce sujet de thèse. Elle aborde également les développements futurs potentiels de ce projet de thèse.

Mots-clés: Détection THz, TDS THz, modulateur THz, film mince, imagerie proche par THz, métamatériau, différenciateur THz, spectromètre dérivé THz

Development of novel metrology methods for time domain THz spectroscopy systems

Fatemeh AMIRKHAN

ABSTRACT

The terahertz (THz) time-domain spectroscopy (TDS) system is a powerful tool because it uses the properties of THz waves in a unique way for spectroscopy and imaging technologies in a wide variety of applications, such as materials science, engineering, medicine, and chemistry. The THz frequency range lies between the microwave and infrared bands in the electromagnetic (EM) spectrum (i.e., between 0.1 THz and 10 THz), which connects the electronic part of the spectrum with the photonics part. Compared to infrared frequencies, THz frequencies can penetrate non-metallic and non-polar materials with low enough energy, which is insufficient to ionize atoms or molecules. In addition, the THz-TDS system can be used to measure not only the intensity of a spectral pulse, but also the associated transient electric field, providing a unique measurement method to easily calculate the amplitude and phase of a pulse from the measured THz electric field.

Over the past 30 years, the performance of THz sensing systems has been improved significantly. However, to move THz spectroscopy and imaging from a laboratory-scale technique to a versatile tool with many practical applications, technical developments are still needed in sources and detectors. Therefore, many scientists are currently working on improving THz sources and detectors with enhanced characteristics, which usually involves using new materials, methods, and techniques to improve these technologies. This essential requirement motivates the subject of my thesis: to develop new methods to improve the detection sensitivity of the THz system.

This work aims to contribute to the development and advancement of knowledge in the field of THz sensing technology. In particular, it focuses on THz detection in the THz-TDS system. To do so, a review of the literature is first presented. It covers the properties of the THz frequency and the THz-TDS system, their generation and detection, and their applications.

Following the literature review, I present a new method for characterizing thin-film electro-optical materials using a metamaterial (i.e., a split-ring resonator (SRR)) and intense THz near-field microscopy. The method is based on the simulation and analytical study of the near-field imaging resolution of the electric and magnetic field distributions of the SRR, which is designed for the THz frequency range. The main advantage of this method is that one can use a non-contact electrode (i.e., the SRR) in the experiment to characterize an unknown thin-film material and then compare the results with the simulation results provided in my approach.

I then present a simple technique by testing a new device in the THz-TDS system that provides a time-derived THz wave. This device is a piezoelectric micromachined ultrasonic transducer array (PMUT) that differentiates a THz pulse by performing time variations (on the femtosecond scale) in the THz beam path. The modulated THz signal detected after the piezoelectric device is proportional to the first-order derivative of the THz pulse. This presentation is coupled with the presentation of the characterization, performance of this device and its limitation as a THz

modulator. This study allows understanding the principle of using this device as a THz modulator in order to increase the knowledge to choose this type of device with better performances.

Following this presentation, I tested another device with the same properties as the previous one, but with larger dimensions and motion to improve the THz wave derivation. This is a piezoelectric micromachined device (PM), which is inserted into the THz beam path. It provides a reference modulation for the lock-in detection unit, which in turn provides access up to the fourth-order of derived information of the incoming THz signal. It should be noted that the integration of the recorded derivative signal leads to a recovered reference signal with an equivalent or even better signal-to-noise ratio (SNR), opening the door to a new type of highly sensitive THz measurement in the time domain.

Finally, there is a conclusion to the work provided in this thesis. It discusses potential future developments of this PhD project.

Keywords: THz sensing, THz TDS, THz modulator, thin film, THz near imaging,Metamaterial, THz differentiator, THz derivative spectrometer

TABLE OF CONTENTS

LIST OF TABLES

LIST OF FIGURES

LIST OF ABBREVIATIONS

ETS	École de Technologie Supérieure
INRS	Institut national de la recherche scientifique
THz	Terahertz
TDS	Time domain spectroscopy
THz-TDS	Terahertz time domain spectroscopy
EM	Electromagnetic
EO	Electro-optic
SRR	Split-ring resonator
PMUT	Piezoelectric micromachined ultrasonic transducer
PM	Piezoelectric micromachined device
SNR	Signal-to-noise ratio
fs	femtosecond
RC	Resistor-capacitor
JOSA B	Journal of the Optical Society of America B
FDTD	Finite difference time domain
LN	Lithium niobate
PCA	Photoconductive Antenna
LT-GaAs	Low temprature grown gallium arsenide
DC	Direct current

GaAs	Gallium arsenide
SI-GaAs	Semi-insulating GaAs
OR	Optical rectification
IR	Infrared
ZnTe	Zinc telluride
CdTe	Cadmium telluride
GaP	Gallium phosphide
GaSe	Gallium selenide
$LiNbO_3$	Lithium niobate
$LiTaO_3$	Lithium tantalate
DAST	Diethylaminosulfur trifluoride
GVM	Group velocity mismatch
ph	Phase
gr	Group velocity
opt	Optical pulse
BS	Beam splitter
g	Grating
OAP	Off-axis parabolic
L	Lens
PBS	Polarized beam splitter

WP	Wollaston prism/polarizer
NA	Numerical aperture
CCD	Charge-coupled device
ANSOM	Apertureless near-field scanning optical microscopy
2D	Two-dimensions
MMD	Metallic mesh device
RF	Radio frequency
FTIR	Fourier transform infrared
NIR	Near-infrared
FIR	Far infrared
R	Resistance
LP	Low-pass filter
LC	inductor-capacitor
FFT	Fast Fourier transform
MO	Magneto-optic
GHz	Gigahertz
Al	Aluminium
AlN	Aluminium nitride
SOI	Silicon-on-insulator
LCC	Leadless chip carrier

Si	Silicon
pp	peak-to-peak
SEM	Scanning electron microscopy
MUMPS	Multi-User MEMS processes
DRIE	Deep reactive-Ion Etching
DUT	Device under the test
HPBW	Half power beam width
AlCr	Aluminium chromium
AC	Alternating current
PPEX	Probabilistic Pulse Extraction

LIST OF SYMBOLS AND UNITS OF MEASUREMENTS

mm	millimeter
μm	micrometer
Hz	hertz
THz	terahertz
meV	millielectron Volt
K	Kelvin
fs	femtosecond
nm	nanometer
cm	centimeter
m	meter
s	second
eV	electron Volt
B	Boltzmann
J	Joule
ps	picosecond
cm^{-1}	centimeter$^{(-1)}$
pm	picometer
V	Volt
fF	femtofarad

A	Ampere
MΩ	Megaohms
MV	Megavolt
ns	Nanosecond
MHz	Megahertz
mW	milliwatt
nW	nanowatt
kHz	kilohertz
pW	picowatt

INTRODUCTION

Context of the research work

The last and least studied of the electromagnetic (EM) spectra, terahertz (THz) spectrum, has become available for study and research in recent decades (Tonouchi (2007); O'Hara, Withayachumnankul & Al-Naib (2012); Danciu, Alexa-Stratulat, Stefanescu, Dodi, Tamba, Mihai, Stanciu, Luca, Spiridon, Ungureanu et al. (2019); Park & Son (2021)) because of advances in ultrafast-laser developments as well as THz generation and detection. As a result, scientists and engineers have been investigating and understanding the wide range of phenomena in these frequencies (Sherwin (2002); Baxter & Guglietta (2011); Zhang, Shkurinov & Zhang (2017); Cocker, Jelic, Hillenbrand & Hegmann (2021); Zhang & Wu (2021); Zhang, Hirori, Sekiguchi, Shimazaki, Iwasaki, Nakamura, Wakamiya & Kanemitsu (2021d)), in which THz electromagnetic radiation offers specific advantages that are not available at other frequencies, as will be discussed in more detail here and in the next chapter.

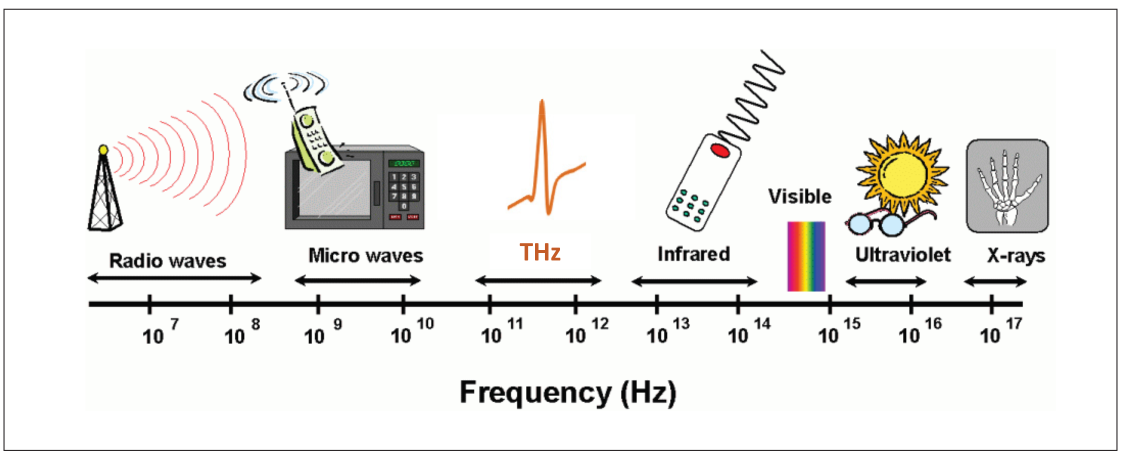

Figure 0.1 The THz frequency range
Taken from Koch (2005)

The THz frequencies lie in the frequency range between the infrared and microwaves from 100

GHz (λ=3 mm) to 10 THz (λ=30 μm) in the EM spectrum, which, in fact, can link electronic devices to photonic devices, as shown in Figure 0.1 (Koch (2005)). One THz frequency is equivalent to a photon energy of 4 meV or a temperature of 48 K (Tonouchi (2007)). THz frequencies have the unique properties of being able to penetrate optically opaque materials such as nonmetallic compounds (e.g., papers, plastics), organic materials, gases, and nonpolar liquids, making them a valuable tool for non-destructive material assessment (Kozlov & Volkov (1998); Nuss & Orenstein (1998); Ferguson & Zhang (2002); Lin, Fischer, Mickan & Abbott (2007); Mittleman (2013)). Furthermore, their low photon energy prevents ionization of materials (unlike x-ray radiation), and their extraordinary sensitivity to water absorption has stimulated research, particularly in characterization and imaging (Blanchard, Chai, Tanaka, Arikawa, Ozaki, Morandotti & Tanaka (2018); Mittleman (2018); Danciu *et al.* (2019)). In addition, the short wavelength and wide bandwidth have created new possibilities for highly controlled and secure point-to-point communication, with the advantage of sufficient data rates up to 10Gbps (Federici & Moeller (2010); Xiao, Yang, Huang, Huang, Zhou, Gao, Shu & He (2018)).

The ultrafast detection of THz waves allows fundamental physics studies, and the THz waves have an increasing number of applications due to their unique properties. More importantly, since THz waves are generated and detected using ultrafast lasers (i.e. femtosecond (fs) lasers), a coherent and phase-locked detection technique is possible. This technique is based on the sampling of the THz field with an fs laser pulse called THz time-domain spectroscopy (TDS). It detects the transient electric field rather than its intensity, allowing amplitude and phase measurements of the THz electric field (Neu & Schmuttenmaer (2018)). This tool is a technique developed analytically for characterizing a wide range of materials, without requiring the use of the Kramers-Kronig dispersion relation (Ueno & Ajito (2008)). Therefore, there exist many sample materials that have been characterized by THz-TDS, many of which have been used to develop new industrial applications (Naftaly, Vieweg & Deninger (2019)). Among them are the investigation of solar cells properties and associated materials (Nagai, Sumitomo, Imaizumi & Fukasawa (2006)), nano-composites materials and dielectric film (Nagai, Imai, Fukasawa, Kato & Yamauchi (2004); Nagai & Fukasawa (2004)). Furthermore, there are various semiconductor materials whose properties are characterized by THz-TDS spectroscopy, such as their conductivity, mobility, and plasma oscillation (Nashima, Morikawa, Takata & Hangyo (2001); Mittleman (2003); Nagai *et al.* (2006); Mittleman (2013)). It is worth noting that the applications of THz-TDS are not limited to the characterization of industrial materials. THz-TDS can also be used in the medical field to sense bacteria (Park, Hong, Choi, Kim, Park, Han, Park, Lee, Kim & Ahn (2014); Berrier, Schaafsma, Nonglaton, Bergquist & Rivas (2012)) and viruses (Park, Cha, Shin & Ahn (2017)) through the use of THz-metamaterials, which are sub-wavelength structures created by engineers (Sarychev & Shalaev (2007); Cui, Smith & Liu (2010)). There are, moreover, potential applications in detecting skin cancer (Yu, Fan, Sun & Pickwell-MacPherson (2012)).

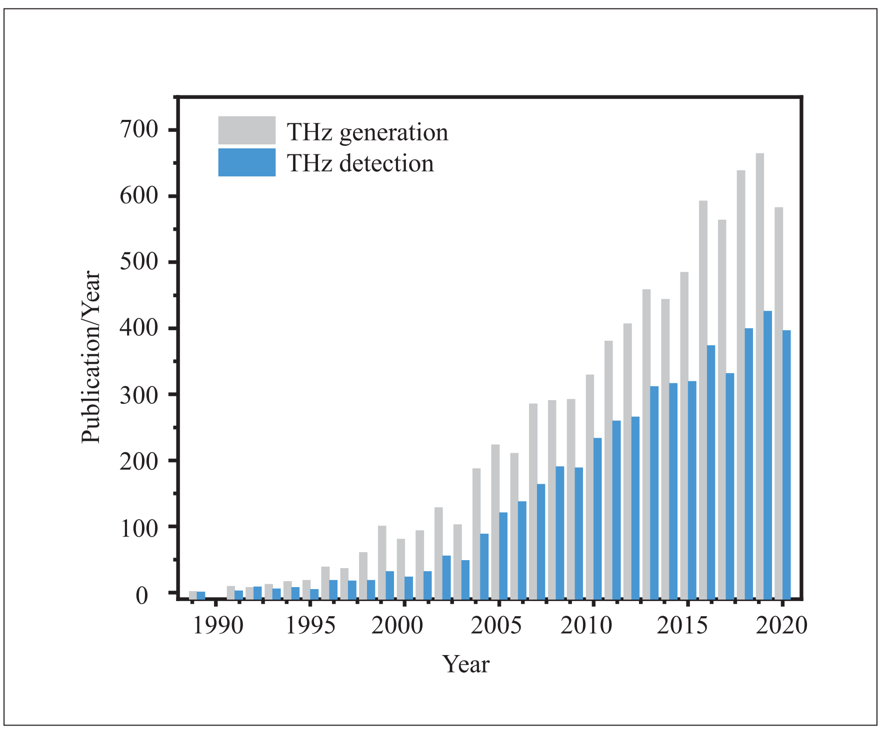

Figure 0.2 Number of publications found by searching two terms of "THz generation" and "THz detection" in the Web of Science database by date of publication

However, the THz-TDS system's abilities depend mainly on its sensitivity, coherent detection, and high signal-to-noise ratio (SNR). As a result, significant research effort is ongoing to identify suitable materials and novel generation and detection techniques to improve the performance of the THz-TDS system for the applications mentioned above, especially for the sensing applications.

Several techniques have been developed during the last few decades to improve the THz-TDS system's characteristics, particularly THz generation and detection techniques. Figure (0.2) shows an intense research focus, as evidenced by the number of published documents related to this research from "Web of Science". According to Figure (0.2), a Web of Science search using the terms "THz generation" and "THz detection" revealed a continuously increasing interest in working on THz detection following the successful development of THz generation in recent years. This figure also shows that THz generation and detection research development increased exponentially from 1990 to 2020. Therefore, research is ongoing for the improvement of the THz-TDS system, and this motivates the subject of my thesis: developing novel methods to improve the detection sensitivity of the system.

Identification of the research problem

The use of electro-optic (EO) sampling as a detector for the THz-TDS system is a required approach in order to reveal essential features of the THz pulse, such as the pulse waveform and spectrum. Furthermore, the EO sampling approach has a broad frequency response and is well suited to THz pulses with high peak intensity, which is especially important for real-time THz image acquisition (Wu & Zhang (1995)). In some cases, a thin EO material with a high EO coefficient is required to achieve near-field detection with high sensitivity (Blanchard *et al.* (2013)). It means using an EO thin-film with a high EO coefficient for the improvement of the SNR in near-field detection systems.

On the other hand, the THz detection bandwidth is fundamentally restricted by the phase mismatch between the THz pulse and the optical beam at 800 nm (Nahata, Auston, Heinz & Wu (1996a)). One way to improve the bandwidth is to use thin crystals, which decrease the impact of the phase mismatch (Kübler, Huber & Leitenstorfer (2005)). In a typical equation, the sensitivity of the EO sampling technique can be described by a phase change of Γ in the EO crystal with an EO coefficient of r_{41}, as defined by (Lee (2009)):

$$\Gamma \propto \frac{1}{\lambda} L\, n_0^3\, r_{41}\, E_{THz}, \tag{0.1}$$

where L is the EO crystal's thickness, λ is the optical beam's wavelength, n_0 is the optical beam's refractive index, and E_{THz} is the THz electric field.

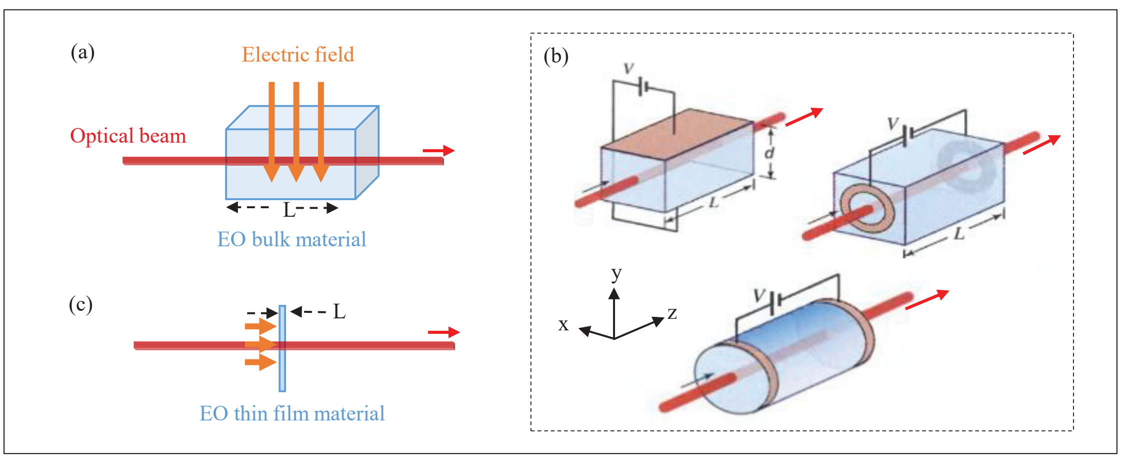

Figure 0.3 (a) Illustrates a fundamental principle of EO material characterization for bulk EO material and (b) a few models for applying electric fields to each orientation of this material using electrodes (taken from Saleh & Teich (1991)) (c) depicts an example of an EO thin-film with L=1μm

The use of EO thin-film decreases the sensitivity of the detection because the thickness of the EO crystal (L) is directly related to the phase changes. One way to compensate for this effect is to select an EO crystal with a high EO coefficient or to increase the THz field (Hirori, Doi, Blanchard & Tanaka (2011)). Characterizing EO thin-film modulators with higher Pockels coefficients is one way to introduce them as a new material for sensing applications.

In general, to characterize EO materials, particularly bulk materials with a length of L (in mm range), one needs to apply an electric field (THz electric field) to the EO sample while an optical beam is passed through it, as shown in figure 0.3 (a). Therefore, an EO sampling technique can be used to measure the EO coefficient of the EO materials. (Aillerie, Theofanous & Fontana (2000); Song, Chai, Liu, Ma, Li, Wang & Hu (2019)). In fact, to reveal all EO responses, one needs to apply the THz electric field in all the different orientations (i.e., x-, y-, and z-directions) of the EO bulk material. Another way to apply an electric field is to place several electrodes on the material in various orientations instead of a THz electric field to reveal all the EO responses, as shown in figure 0.3 (b) (Saleh & Teich (1991)). However, using the EO sampling method to characterize EO coefficients of EO thin-films with L in the μm range, either by applying a THz electric field or providing an electric field in another frequency by putting electrodes on all orientations of the thin-films (see Fig. 0.3 (c)), is extremely difficult.

Furthermore, the interaction range of light traveling through the EO thin-film is also limited. Several methods are applicable to characterize EO thin-films, such as spectroscopy ellipsometry, the Teng-Man method (Schroder (2006); Hansen (1973); Tompkins & Irene (2005); Kang, Xiao, Avrutin, Özgür, Morkoç, Park, Lee, Lee, Wang & Smith (2008); Teng & Man (1990)), and the transmission method (Reitze, Haton, Ramesh, Etemad, Leaird, Sands, Karim & Tanguay Jr (1993); Hoerman, Nichols, Nystrom & Wessels (1999)). They measure the variation of the refractive index by applying an electric field. These methods, however, are challenging to use because of their low sensitivity and inaccurate measurement (Tompkins & Irene (2005); Kang *et al.* (2008)). They are also dependent on the thin-film's thickness (Liu, Mak & Wong (2009)), or are difficult to design and process (Lee, Kim, Kim, Lee, Lee & Steier (2011)). We found that one can use a non-contact visualization of the electric fields to reveal EO thin-film's coefficient by employing EO sampling THz microscopy and using a metamaterial, instead of electrodes with wires (See Chapter 2, Part 2.3).

Derivative spectroscopy is another method to characterize materials by improving the resolution of a reference spectrum and its sensitivity. Because a fundamental feature of a derivative signal is its ability to detect and identify the slope of a signal as well as the position of the peak in a time-varying signal (Skolnik (1962)), this can add an important benefit for sensing purposes by its capability to identify in real-time fixed points such as local maxima and minima with better accuracy, to improve layer detection accuracy (Redo-Sanchez *et al.* (2016)) or changes in refractive indices (Blanchard, Sumida, Wolpert, Tsotsalas, Tanaka, Doi, Kitagawa, Cooke, Furukawa & Tanaka (2014b)) for THz phase-contrast imaging. One way to obtain derivative signals is typically to carry out a variety of schemes, including fibre grating, temporal lensing, and EO effects (Salem, Foster & Gaeta (2013); Slavík, Park, Kulishov, Morandotti & Azaña (2006); Azaña (2010)). Another way to obtain the derivative of an input optical signal is to use a resistor-capacitor (RC) filter in combination with a modulation device in the optical path. This technique is known as derivative spectroscopy (Klein & Dratz (1968); Dubrovkin (1983); Holcomb & Little (1992); Wiley, Tanner, Chandler & Anderssen (2009); Karpińska (2004)).

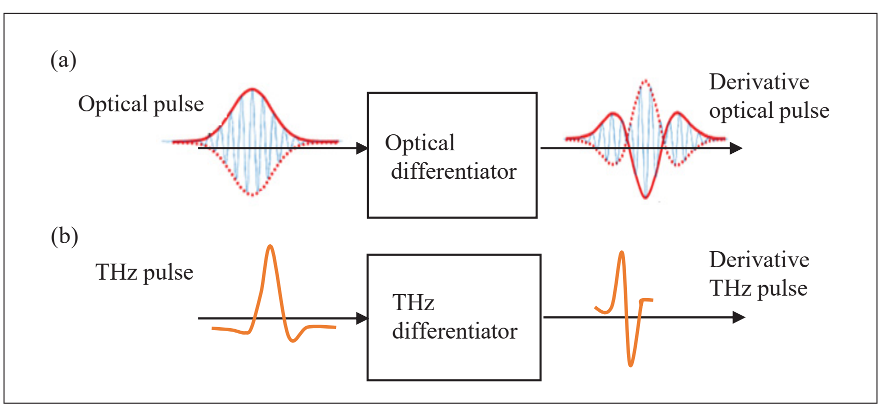

Figure 0.4   A simplified explanation of the differentiator methods shows for (a) optical signals and (b) THz pulses

Many of these methods have been demonstrated in the near-infrared frequency band but not in the THz band. In addition, these approaches deal with the complex envelope of an input signal's intensity profile (see figure 0.4(a)); but THz measurement systems provide a THz electric field (see figure 0.4 (b)) that gives direct access to amplitude and phase. For signal processing in the THz range, this THz feature has many advantages. One advantage is the ability to recover ultra-fast THz phenomena using low-frequency electronic instruments such as a lock-in amplifier (Neu & Schmuttenmaer (2018)). As a lock-in amplifier is already a resistor-capacitor (RC) filter, we realized a THz time-domain derived spectrometer could theoretically be created by adding a suitable THz modulator. To date, however, only a few efforts have been made with a grating and ring resonator (Filin, Stowe & Kersting (2001); Xie, Zhu, Zhang, Zang, Chen, Balakin, Shkurinov & Zhu (2020)) to reveal passive THz differentiators.

Research objective and approaches

This PhD project aims to develop new methods to improve THz sensing in the THz-TDS system. The thesis is divided into two parts: (1) analysis and simulation of THz near-field images to obtain EO thin-film characteristics, and (2) a new type of THz modulator have been tested that are piezoelectric micromachined ultrasonic transducer (PMUT) array and piezoelectric micromachined (PM) device).

Characterizing EO thin-films to find their EO coefficient is one solution for improving the sensitivity of the THz-TDS system. We demonstrate this new method for characterizing EO thin-film material by analyzing and performing simulations of THz near-field images of a split ring resonator (SRR), which is a unit cell of metamaterial placed on top of the EO thin-film to retrieve the EO thin-film's characteristics. THz near-field microscopy with EO sampling is an excellent technique for observing the distribution of all electric and magnetic fields in a THz metamaterial (Blanchard *et al.* (2013); Blanchard, Doi, Tanaka, Hirori, Tanaka, Kadoya & Tanaka (2011)). In addition to this, the local field enhancement of a metamaterial structure (such as SRR) significantly improves the interaction between THz field and the material under the test, allowing the detection of tiny concentrations on the EO thin-film. Therefore, to develop the method to study EO thin-film coefficients, intense THz near-field imaging through EO sampling and a unit cell of metamaterial (SRR) can be used. This development will result in the introduction of a new EO thin film material with a better EO coefficient.

The second objective is using another method for improving the sensitivity of the THz-TDS system is to modulate the THz wave. For example, to obtain a THz time derivative wave, one can use a THz modulator in the THz beam path to delay the THz in the fs time range and measure the differential between these two signals. In this thesis, we tested a device which works on the basis of the piezoelectric effect, which can be placed in the THz beam path to modulate the THz wave in time as a new THz modulator (PMUT array). Development of this method can result in implement a proof of concept for the THz differentiator. Then by improving this method by using a device with better performance (PM device). This method can introduce a novel THz derivative spectrometer (by introducing a THz differentiator).

The following approach was used to characterize EO thin-film. First, we used an intense THz electric field to apply and enhance the interaction inside the material since we can thus generate powerful THz pulses (Hirori *et al.* (2011)). Furthermore, we designed and used a metamaterial called SRR as a subwavelength device. The SRR acts as an electrode and produces resonant responses in all directions simultaneously (as illustrated in Figure 0.5 (a)). We placed SRR on top of the EO thin-film to apply the THz field to all orientations of the EO thin-film, as shown in figure 0.5 (a). We then used EO sampling THz microscopy to measure all EO responses in the x-, y-, and z-directions of the film.

Another approach to improve THz-TDS system sensitivity is to convert the THz signal to a derivative THz signal. We developed a simple method for obtaining THz derivative signals. As a starting point, we used a piezoelectric micromachine device as a subwavelength device

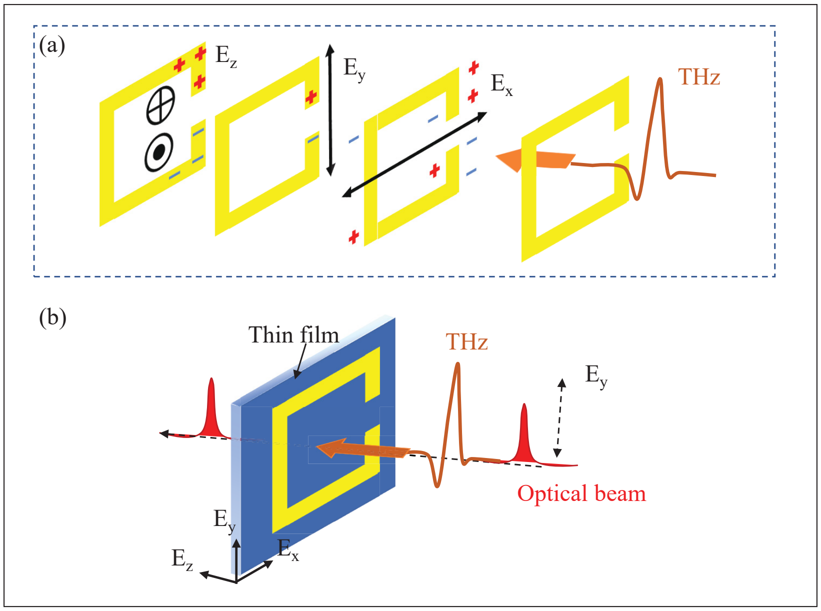

Figure 0.5 An illustration of (a) how SRR serves as an electrode in three orientations and (b) how SRR is being used to apply a THz electric field to an EO thin-film

controlled by an external electric field with a MHz frequency.

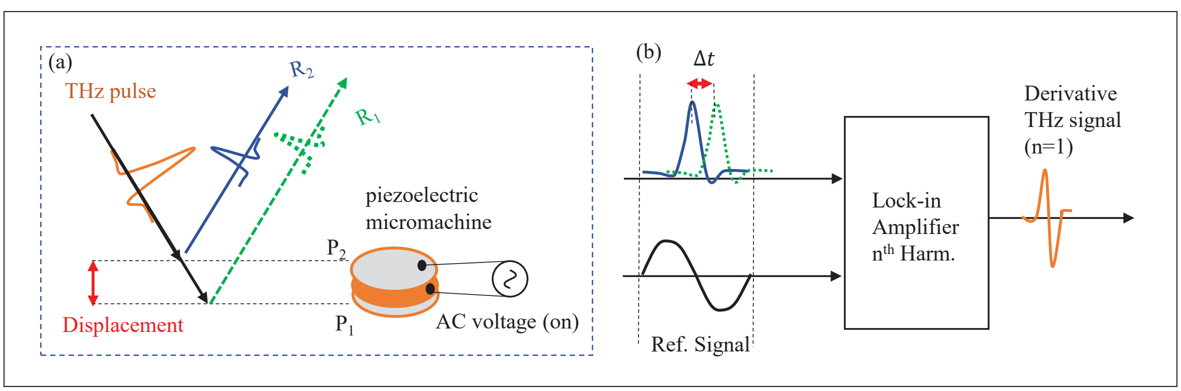

Figure 0.6 Showing (a) how the piezoelectric device works in the THz beam direction and (b) how the piezoelectric device and the lock-in amplifier work together to generate a THz derivative signal

This device acts as a simple mirror in the THz beam path. When it is activated, it reflects two THz waves with a time variation of Δt corresponding to its displacement, as shown in figure 0.6

(a). This method is the first introduction of an active THz time differentiator by using lock-in detection, as presented in figure 0.6 (b). As a first demonstration, this method was limited by the device's small size and motion. Furthermore, the device requires an MHz oscillator, which makes it less suitable for standard THz applications. To overcome these limitations, we used a piezoelectric device with more significant motion and larger dimensions that operate at a low kHz frequency.

The main part of this research work is designed to be an original scientific paper-based thesis, as advised by the submission policy of the École de technologie supérieure (ETS). In order to achieve my research objective, I contributed to the publication of six peer-reviewed academic articles as first author and co-author. I was the first author on three of them, which correspond to the three chapters (2, 3 & 4) of this thesis. I also had the opportunity to collaborate with other groups both inside and outside ETS, resulting in three co-authorships. The chapters from the journal article constitute an abstract, introduction, design and structure, methodology, theoretical and experimental of subwavelength devices as THz modulators, followed by the results and discussion. The main content of the thesis comprises an abstract, introduction with research objectives, literature review, conclusion, and statement of original contribution with future recommendations.

Thesis Structure

Following the **introduction**, the thesis is structured as follows. The next chapter of this thesis, **literature review**, contains no original contribution but provides information (introduction) about different concepts and techniques needed later in this thesis. It mainly explores the related research work and gives details that are not available in the articles. The THz frequency range is introduced, followed by the THz sensing techniques, which consist of several forms of generation, detection, and THz-TDS systems and their principles and concepts. This section includes THz near-field imaging and metamaterials, particularly SRR. The literature review also discusses THz differentiators and derivative spectroscopy. The three following chapters present two methods for the development of THz sensing to achieve the proposed research objectives, which resulted in the journal publications. **Chapter 2** is an article published in the Journal of the Optical Society of America B (JOSA B) in 2019 under the title **"Characterization of thin-film optical properties by THz near-field imaging method"**.

In this chapter, all field distributions of SRRs, including the electric and magnetic fields in three dimensions (x, y, z), are numerically studied as a function of exciting and probing beam polarizations using finite difference time domain (FDTD) simulation in order to develop a method for finding EO thin-films with better performance. Then, we demonstrate that the experimentally found response of the well-known Lithium Niobate (LN) crystal agrees with our simulations. Following that, the sensitivity of the LN crystal as a function of the applied electric field and optical probe polarization is studied analytically to calibrate our approach. This demonstration validates our approach to assessing thin-film EO materials.

Chapter 3 is an article published in Optics Letters in 2020 and has been patented with the title **"Active terahertz time differentiator using piezoelectric micromachined ultrasonic transducer array"**; it is followed by supplementary information regarding this work.

A first-order temporal differentiation in the THz region is achieved utilizing an 8-piece piezoelectric micromachined ultrasonic transducer (PMUT) array driven at its resonance frequency. The properties and functioning of the PMUT are described initially in this chapter. The methodology and results of this research are then discussed. Finally, the influence of PMUT amplitude mobility on derivative signal behavior is assessed.

Chapter 4 is an article published in Optic Express in 2021 under the title **“Terahertz time-domain derivative spectrometer using a large-aperture piezoelectric micromachined device”.**

A piezoelectric micromachined device (PM) with a higher surface area and functioning in the kHz frequency range is used to demonstrate an nth-order THz time-domain derivative spectrometer. The proposed structure for PM devices, as well as their functions, are described in this chapter. The lock-in amplifier's operation to access the multiple-order derivative of the incoming THz signal is also explained. Then, the experimental setup and the resulting findings are discussed. Finally, the excellent agreement between our experimental and simulation results is indicated.

The last chapter, **Conclusion and Recommendations**, briefly concludes the thesis with future research recommendations.

CHAPTER 1

LITERATURE REVIEW

1.1 THz frequency range

The THz frequency range is the part of the electromagnetic (EM) spectrum that lies between the infrared and microwave regions, as shown in Fig. 1.1. Today, the THz frequency range is commonly defined from 100 GHz to 10 THz, and there is a growing range of techniques for its generation and detection (Mittleman (2003); Sakai & Tani (2005); Li & Li (2020)).

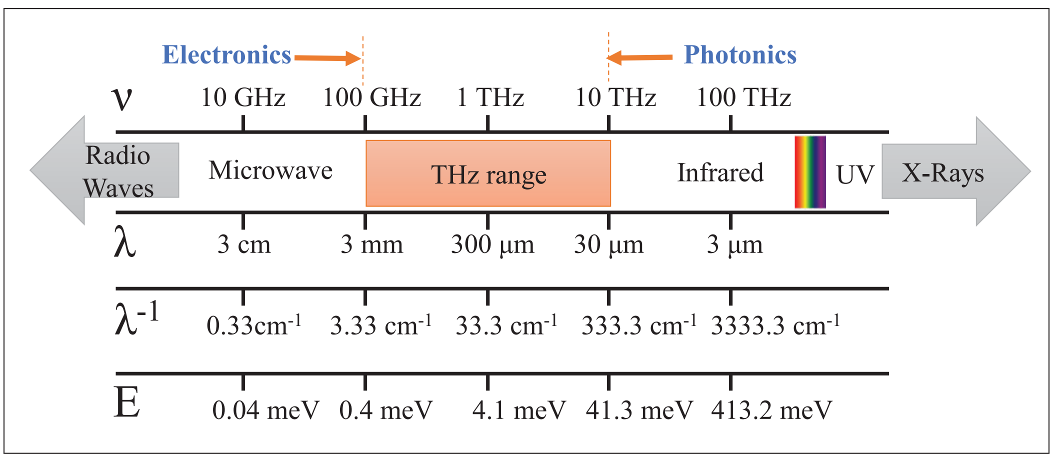

Figure 1.1 THz range in the EM spectrum

As the wavelengths λ of an EM wave are linked to the frequency f_{THz} ($\lambda = \frac{c}{f_{THz}}$, $c = 3 \times 10^8\ m/s$), the boundaries of this spectral range are typically described by wavelengths ranging from 30 μm to 3 mm. Furthermore, the THz range can be defined in terms of wavenumber υ (with the units cm^{-1}) from 3 cm^{-1} to 300 cm^{-1} (where $\upsilon = \frac{1}{\lambda}$). The energy of one THz photon (E with a unit of J) is extremely low and is given by

$$E = h\, f_{THz} = \hbar\omega \simeq 6.6 \times 10^{-22}\, f_{THz}, \tag{1.1}$$

where ω is the angular frequency, and h is Planck's constant ($h \simeq 6.62 \times 10^{-34} J.Hz^{-1}, and\ \hbar = \frac{h}{2\pi}$). So it is preferable to use the electron-volt (eV) as the unit ($1\ eV = 1.6 \times 10^{-19}\ J$):

$$E \simeq 4.125 \times 10^{-3}\ f_{THz} \simeq \frac{1.237}{\lambda_{\mu m}}\ ev. \tag{1.2}$$

Thus, the energy range of THz waves spans from 0.41 to 41 meV. Finally, the THz range can also be defined in terms of equivalent temperature T, in regard to photon energy, as follows,

$$E = h\ f_{THz} = k_B T \ \Rightarrow\ T = \frac{h}{k_B}\ f_{THz}, \tag{1.3}$$

with $k_B \simeq 1.38 \times 10^{-23}\ J/K$ being the Boltzmann constant. Therefore, equivalent temperatures of the THz waves (from 1 THz to 10 THz) lie between 4.8 and 47.8 K. Fig.1.1 illustrates the THz region with different terms.

Since the THz range is associated with low photon energy, heat radiation and temperature are noise sources in THz experiments, and they can completely dominate the THz signal. Furthermore, THz waves will interact with matter only through resonances of molecule rotations and vibrations. While this frequency range is non-ionizing and hence non-destructive, it is known to excite bound charges, charge plasmas, molecular dipoles, and phonons in crystalline materials (Jepsen, Cooke & Koch (2011)).

In summary, the THz range's unique features are as follows (Sakai & Tani (2005); Coutaz, Garet & Wallace (2018)). There is a distinct absorption line in molecular gases due to the interaction of the rotation of the molecule with the THz radiation, and it exists only in gases. Since each molecular species has its own characteristic rotational energy levels that uniquely determine the precise frequencies of the absorption lines, this process is applied to environmental monitoring, atmospheric remote sensing, and analysis of the interstellar medium (Farman, Gardiner & Shanklin (1985); Solomon, Garcia, Rowland & Wuebbles (1986); Albert, Petkie, Bettens, Belov & Lucia (1998)). Furthermore, there is no rotation effect in solid and liquid materials. Since THz waves are longer than visible wavelengths and infrared waves, this means

Mie dispersion has less impact on THz waves. Therefore, this frequency can penetrate through a wide variety of common materials, such as clothes, paper, wood, plastics, and cardboard (Köhler, Tredicucci, Beltram, Beere, Linfield, Davies, Ritchie, Iotti & Rossi (2002); Piesiewicz, Jansen, Wietzke, Mittleman, Koch & Kürner (2007)), which are totally opaque in the visible and near-infrared spectrum. Therefore, these materials appear transparent to THz imaging systems (Lin *et al.* (2007)). In addition, the majority of dielectric materials, such as polymers, silicon, and semiconductors (Podzorov & Gallot (2008); Naftaly, Molloy, Magnusson, Andreev & Lanskii (2016); Shi, Huang, Lu, Zhang, Yue, Qiao & Xiao (2014)), are transparent for THz waves because of their low free charges, which result in poor absorption or low conductivity. In addition to this, the effects of free charges and lattice vibrations in many materials result in significant absorption or reflection of THz waves. THz vibrations, for example, are reflected by free-charged materials (Lloyd-Hughes & Jeon (2012)) such as noble metals (Ag, Cu, Au, Al), which function somewhat as mirrors that can be used for security applications (Ren, Zahid, Fan, Yang, Imran, Alomainy & Abbasi (2019)). In addition, in pure and perfect crystals in the vicinity of 10 THz, phonon lines (caused by lattice vibrations) create substantial absorption peaks. For instance, the GaAs crystal contains phonon absorption lines at 8.1 and 8.8 THz (Shen, Upadhya, Beere, Linfield, Davies, Gregory, Baker, Tribe & Evans (2004)). These absorption peaks showed resonance structures associated with acoustical and optical phonons at various frequency combinations. Another THz characteristic is that polar liquids (Møller, Cooke, Tanaka & Jepsen (2009)), such as water, absorb substantial amounts of THz vibrations, resulting in strong vibrational absorption of water molecules at these frequencies. However, non-polar liquids, such as certain oils, are highly transparent (Pedersen & Keiding (1992)).

Therefore, based on the THz characteristics, this part of the spectrum is suitable for spectroscopy and imaging (Tonouchi (2007); Chan, Deibel & Mittleman (2007); Kampfrath, Tanaka & Nelson (2013)). THz imaging and THz spectroscopy are two essential technologies for THz applications in material characterization, security, diagnostic medicine, non-destructive evaluation, and quality control because of their excellent spatial and temporal resolution compared to microwaves. In addition, THz waves, unlike X-rays, cause a negligible impact on cells because of their low photon energy and may thus be employed for non-invasive detection of organisms and have broad medical applications (Wang, Zhang, Chang & Cui (2019a)). THz technology has also been widely used in the development of semiconductor and superconductor materials (Gu, Singh, Tian, Cao, Xing, He, Zhang, Han, Chen & Zhang (2010)). Simultaneously, these characteristics will probably make this band excellent for rapid data transfer in the future of THz communication (Federici & Moeller (2010); Ma, Geng, Fan, Liu & Chen (2019); Chen, Ma, Zhang, Zhang, Niu, Kuang, Chen, Li & Li (2019)).

1.2 Terahertz sensing techniques

THz sensing techniques include THz-emission (generation) spectroscopy (Huang, Yao, He, Zhu, Zhang, Bai & Xu (2019)), THz-detection spectroscopy, and THz-TDS (Mittleman (2013)). This means that we can characterize a material by placing it either in generation, detection, or at the focus point of the THz beam via THz-TDS. For example, these techniques are exploited to characterize the electronic properties of semiconductor nanowires. They allow engineers and researchers to control and obtain the full potential of the electrical properties of these materials. Researchers have optimized and tailored the performance of these electronic devices by understanding and measuring important properties such as carrier lifetime, electron mobility, electron drift velocity, and dopant concentrations (Grischkowsky, Keiding, Van Exter & Fattinger (1990); Van Exter & Grischkowsky (1990); Seo, Yoo, Dayeh, Picraux, Taylor & Prasankumar (2012); Ketterer, Uccelli & i Morral (2012); Ulbricht, Hendry, Shan, Heinz & Bonn (2011); Van Exter & Grischkowsky (1990)). We can also explain the carrier dynamics of the materials through plasma frequency and scattering rate by making the THz-TDS of these materials and applying the Drude-model. These methods can also be applied to thin-films such as graphene (Jiang, Xu & Zhang (2000b)).

THz emission spectroscopy is comparable to THz-TDS in terms of material characterization. Rather of utilizing a typical THz source, the THz-TDS system generates THz pulses using a material that is currently under investigation (testing). The THz emission method offers many promises for investigating the basic and practical properties of materials (Bell (2017);

Huang *et al.* (2019); Rana & Tonouchi (2020)). An alternative method to characterize material samples is THz detection spectroscopy. This spectroscopy is quite similar to THz emission spectroscopy, but the sample material is placed on the detector section of the THz-TDS system and is characterized via the detection process. The detection process allows characterizing the electro-optic (EO) properties of the material. For instance, the strength of the THz signal is linearly proportional to the linear EO coefficient. Thus we can measure the linear EO coefficient of the material.

To understand how to increase the sensitivity of these approaches, we will discuss the concept and working mechanism of each technique separately in the sections below.

1.3 THz generations

The generation of EM radiation can be described using the wave equation from Maxwell's equations in a medium (Cooke (2007)):

$$\nabla^2 E - \epsilon \mu \frac{\partial^2 E}{\partial t^2} = \mu \frac{\partial J}{\partial t} \tag{1.4}$$

The right-hand side of the Eq. 1.4 presents the fundamental source of emission known as non-uniform motion of charge. Here, ϵ is the permittivity, μ is the permeability of the medium, and E is the electric field. In general, the current, J, can be induced by conduction (J_{cond}) and oscillating bound electrons ($J_{bound} = \frac{\partial P}{\partial t}$) contributions. Therefore, we can take both free and bound charge carriers into account in this equation:

$$\nabla^2 E - \epsilon \mu \frac{\partial^2 E}{\partial t^2} = \mu \left(\frac{\partial J_{cond}}{\partial t} + \frac{\partial^2 P}{\partial t^2}\right) \tag{1.5}$$

Eq. 1.5 is the wave equation with two source terms on the right side: the first derivative of a conduction current ($\frac{\partial J_{cond}}{\partial t}$) and the second derivative of the polarization ($\frac{\partial^2 P}{\partial t^2}$). An emitted $J(t)$ lasting for a few hundred femtoseconds to a few picoseconds duration leads to the generation of EM waves in the THz frequency range. Several different techniques have been used to generate THz radiation. For example, THz emission through photoconductive antennas (Tani, Matsuura, Sakai & Nakashima (1997); Burford & El-Shenawee (2017)), extended photoconductive sources (Kim & Kwok (1995)), optical rectification (Nahata, Weling & Heinz (1996b)), surge current through the depletion field of semiconductor surfaces (Adomavičius, Urbanowicz, Molis, Krotkus & Šatkovskis (2004); Chuang, Schmitt-Rink, Greene, Saeta & Levi (1992)), charge oscillations in quantum well structure (Chuang, Planken, Brener, Roskos & Nuss (1994)), coherent excitation of active phonons (Dekorsy, Auer, Bakker, Roskos & Kurz (1996)), superconductors (Hangyo, Tomozawa, Murakami, Tonouchi, Tani, Wang, Sakai & Nakashima (1996)), and nonlinear transmission lines (NLTLs) (Rodwell, Kamegawa, Yu, Case, Carman & Giboney (1991)). Most of these are based on the excitation of materials with femtosecond (fs) laser pulses. In this research, two THz sources have been used. They are the THz source based on a photoconductive antenna and optical rectification in a nonlinear crystal.

1.3.1 Photoconductive antennas

A photoconductive antenna (PCA) is a fundamental technique for generating THz radiation. It was invented by Austin in 1970 and further developed in the 1980s (Auston, Cheung & Smith (1984)).

Figure 1.2 shows a standard scheme for generating THz radiation from a PCA. The PCA consists of a metal dipole antenna (electrodes) patterned on a photoconductive substrate (semiconductor) to apply DC biased voltage. The substrate properties of the PCA have a critical impact on the generation of THz radiation. As a result, the substrate should have a bandgap energy that is somewhat lower than the laser photon energy, high carrier mobility, a short carrier lifetime, and a high breakdown voltage. Figure 1.2 shows that an 800 nm fs laser pulse (i.e., the emission wavelength of Ti: Sapphire lasers), with a pulse duration of 100 fs, is focused on the gap between the two electrodes and propagates into the semiconductor. The gap size usually varies between 10 μm and 60 μm. Since the photon energy propagated into a semiconductor is slightly higher than the bandgap, photons are absorbed by the substrate. Consequently, electron-hole pairs are created inside the conduction band of the semiconductor crystal. The DC-biased voltage then

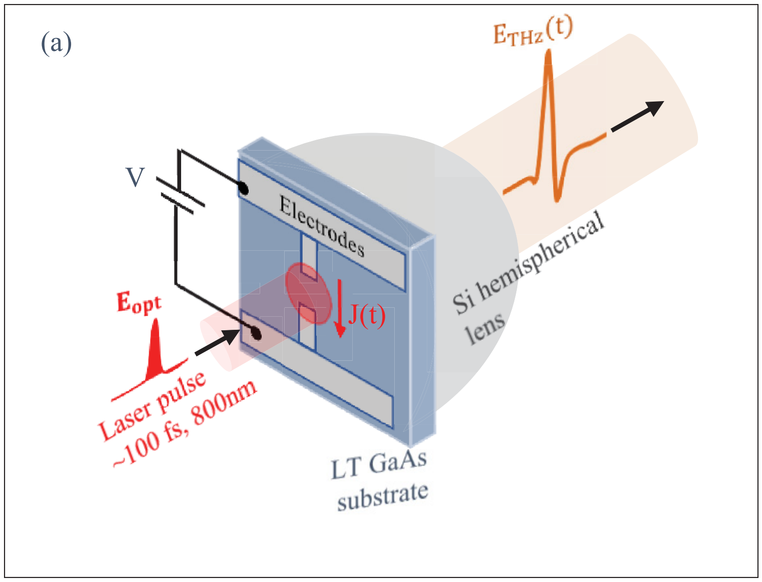

Figure 1.2 THz source illustration based on a low-temperature photoconductive antenna (PCA)

accelerates these free carriers, resulting in a transient photocurrent that drives the dipole antenna and re-emits as a THz pulse, as illustrated in Figure 1.2.

Figure 1.3 illustrates the PCA's transient response, in which the generated carriers are proportional to the laser pulse as it is absorbed into the semiconductor. This means that a transient photocurrent with a time increase is proportional to the rise time of the incident optical pulse on the gap of the antenna. THz radiation by current density time-dependent modulation is described by Maxwell's classical equation as,

$$E(r,t) = \frac{l_e}{4\,\pi\,\epsilon_0\,c^2 r}\,\frac{\delta J(t)}{\delta t}\,\sin(\theta) \propto \frac{\delta J(t)}{\delta t}, \tag{1.6}$$

where l_e and J(t) are the effective length of the PCA and the current in the dipole, respectively. ϵ_0 and c, respectively, are the dielectric constant of vacuum and the velocity of light in a vacuum. In addition, the angle from the direction of the dipole is θ. Equation (1.6) shows that the variation in current density will generate EM waves. Since the variation of the photocurrent occurs on a sub-picosecond time scale, a THz pulse is generated, with the THz electric field

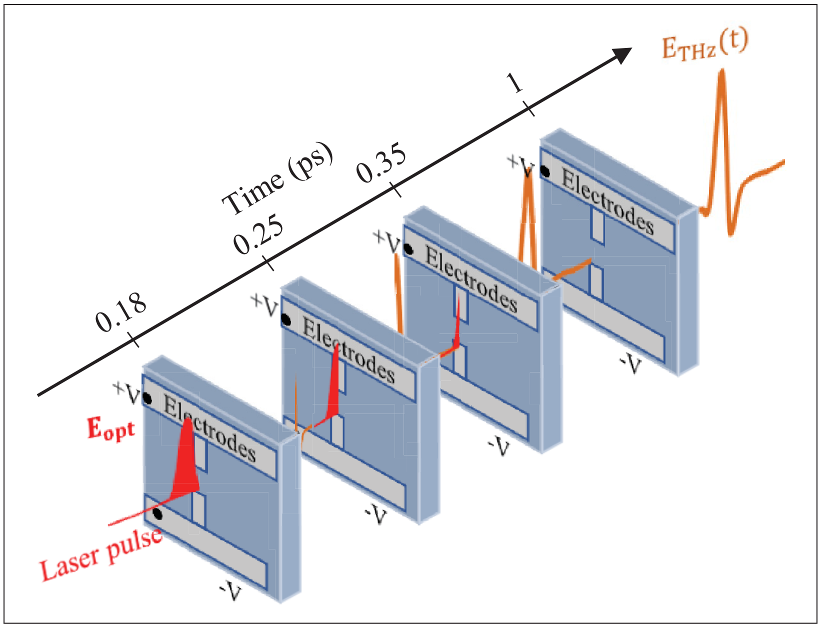

Figure 1.3 An example of pulsed THz generation in a PCA: a femtosecond optical laser pulse propagates into the PCA, creating a transient photocurrent that drives the antenna upon being re-emitted as a THz pulse

being directly proportional to the time derivative of the photocurrent and the biased electric field (Scott, De Araujo & Carlos (1989)).

Compared to other THz sources, the main advantage of the PCA is that THz energy is taken from the DC-biased voltage rather than from the optical pulse energy. As a consequence, even with laser pulses produced by an oscillator laser, it is possible to achieve an efficiency of the order of 10^{-4}. The most often used semiconductor for the emitter is gallium arsenide (GaAs) with a band gap of 1.42 eV, either semi-insulating GaAs (SI-GaAs) or low-temperature grown GaAs (LT-GaAs), because of its high carrier mobility ($\mu \approx 8500\, cm^2/Vs$)(Sze, Li & Ng (2021)) and very short carrier lifetime ($\tau \approx 100$ fs) (Stellmacher, Schnell, Adam & Nagle (1999)). The THz waves generated by the PCA diverge significantly, which might be a concern when collecting THz waves in free space. In general, commercial PCAs feature a hemispherical high resistivity silicon lens connected to the back of the substrate. This connection reduces the number of THz pulse reflections that can occur because of an air gap. Furthermore, at THz frequencies, silicon (n = 3.47) has an excellent refractive index match with GaAs (n = 3.6), reducing reflection losses. At THz frequencies, silicon exhibits low dispersion and absorption.

While LT-GaAs is a commercial emitter suitable for high repetition rate lasers, it has a bandwidth of up to 5 THz. Because its optical phonons exhibit 8.5 THz (Sze *et al.* (2021)), high-frequency THz radiation is absorbed by GaAs. This problem can be solved by using a thin GaAs layer of 1–2 μm. Nevertheless, these thin layers of GaAs are too fragile for the lithography process and practical applications. Therefore, this layer of LT-GaAs must be attached to a substrate, silicon, which has a similar refractive index and is THz transparent. THz pulses of up to 10 THz bandwidth have been demonstrated with this technique (Heiliger, Vossebürger, Roskos, Kurz, Hey & Ploog (1996); Klos, Bartholdt, Klier, Lampin & Beigang (2015)).

1.3.2 Optical rectification

Historically, optical rectification (OR) in a nonlinear medium was widely known in the 1970s to generate light in the far-IR range (Yang, Richards & Shen (1971)). But, Rice et al. (Rice, Jin, Ma, Zhang, Bliss, Larkin & Alexander (1994)) presented experimental and theoretical confirmation of rectification using a Zinc telluride (ZnTe) crystal in 1994. In their work, there was no photocurrent when the incoming light was normal to the nonlinear crystal surface, confirming that the radiation phenomenon was caused entirely by an OR process. Figure 1.4 shows the OR method in which an intense optical beam travels through a second-order nonlinear crystal, inducing transient polarization and generating THz waves.

OR is a second-order nonlinear effect that occurs in a non-centrosymmetric nonlinear crystal when an optical field is applied strongly enough to create significant electron displacements from equilibrium. OR is, in fact, a process in which an optical laser pulse induces a time-dependent polarization change in a crystal, causing it to emit an EM wave. The time dependence of radiated THz field (E_{THz}) is given by the equation (Dexheimer (2007)):

$$E_{THz} \propto \frac{\partial J_{bound}}{\partial t} = \frac{\partial^2 P(t)}{\partial t^2}. \tag{1.7}$$

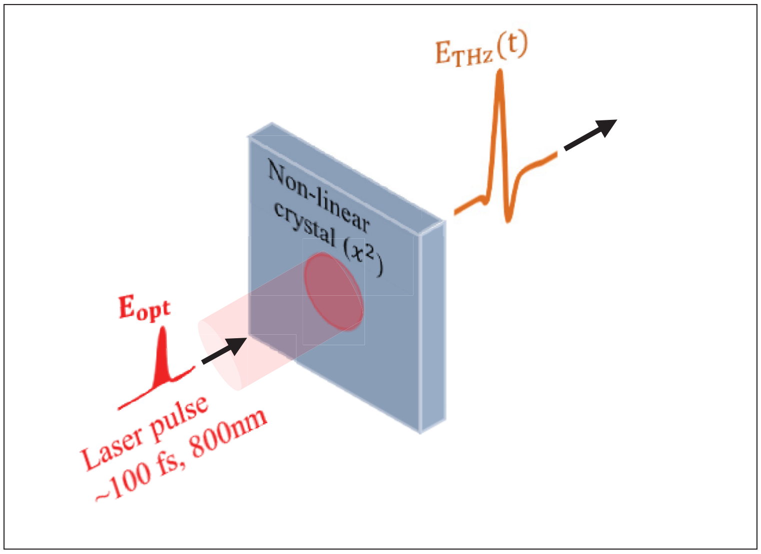

Figure 1.4 The configuration for generating THz pulses via the OR method in a nonlinear crystal

By assuming two frequency components of the driving electric field of the optical pump (E_{opt}) that can be expressed by $E_1(t) = \cos(\omega_1 t)$ and $E_2(t) = \cos(\omega_2 t)$. The second-order polarization, $P^{(2)}(t)$, can be described by:

$$P(t) \propto \chi^{(2)} \cos(\omega_1 t) \cos(\omega_2 t) = \frac{\chi^{(2)}}{2} [\cos(\omega_1 + \omega_2) t + \cos(\omega_1 - \omega_2) t]. \tag{1.8}$$

Here, $\chi^{(2)}$ is the second-order electric susceptibility tensor of the nonlinear crystal. In Eq. 1.8, the first term represents the sum frequency, which presents second harmonic generation; and the second represents the difference frequency, which corresponds to OR. In fact, when the frequencies of these two photons are equal, ($\omega_1 = \omega_2$), a special case of the difference frequency occurs. Equations 1.7 and 1.8 show that the polarization acts as a source that radiates EM waves with a duration proportional to the duration of the fs laser pulse (Dexheimer (2007)). This technique is usually simpler than using a PCA because no external electrical components are needed. Furthermore, this method provides the broad bandwidth that is linked to OR (Reimann, Smith, Weiner, Elsaesser & Woerner (2003); Mu, Zotova & Ding (2008)). In fact, the phase-matching condition between the optical and the THz beam inside the crystal is one of the most important factors to consider for the efficiency of the OR process. If the phase-matching condition is fully satisfied, the THz waves will build up coherently and reach through the whole thickness of the nonlinear crystal. The other factor to consider is the second-order nonlinear coefficient of the crystal.

In summary, several factors influence the efficiency, shape, and frequency distribution in the THz waveform, including the materials used, crystal orientation, nonlinear coefficient, thickness, and absorption as well as dispersion, diffraction, optical pulse duration, phase-matching, and saturation (Nahata *et al.* (1996b)). Table 1.1 shows the comparison of different types of crystals (Dexheimer (2007); Hebling, Stepanov, Almási, Bartal & Kuhl (2004); Nikogosyan (2006)) for THz generation using the OR method.

Table 1.1 Comparison of different materials for THz generation via OR

Type of crystal	**EO coefficent (pm/V) @(μm)**	**Refractive index (n_{opt}^{gr}) @(μm)**	**Refractive index (n_{THz}^{ph}) @THz**	**Absorption coefficient (α_{THz})(cm^{-1})**	**GVM (ps/mm)**
CdTe	r_{41} = 4.5 @0.8	3.73 @0.8	3.23	4.8	0.75
GaAs	r_{41} = 1.43 @0.8	4.18 @0.8	3.4	0.5	0.015
GaSe	r_{22} = 14.4 @0.8	3.13 @0.8	3.7	0.07	0.10
GaP	r_{41} = 0.97 @0.8	3.57 @0.8	3.6	1.9	-
ZnTe	r_{41} = 4.04 @0.8	2.853 @0.8	3.2	1.3	1.1
$LiTaO_3$	r_{33} = 30.5 @0.820 r_{13} = 8.4 @0.820	n_0 = 2.46 @0.633 n_e = 1.70 @0.633	$n_0 \approx 6.5$ $n_e \approx 6.4$	46	14.1
$LiNbO_3$	r_{13} = 6.5 @0.633 r_{33} = 30.9 @0.633 r_{51} = 32.6 @0.633 r_{22} = 3.4 @0.633	n_0 = 2.46 @0.633 n_e = 1.70 @0.633	$n_0 \approx 6.46$ $n_e \approx 6.15$	16	14.2
DAST	r_{11} = 160 @0.820	n_0 = 2.46 @0.820 n_e = 1.70 @0.820	2.3	150	1.22

Cadmium telluride (CdTe), GaAs, gallium phosphide (GaP), ZnTe and gallium selenide (GaSe) are semiconductors, whereas lithium tantalate ($LiTaO_3$) and lithium niobate ($LiNbO_3$) are inorganic EO crystals, and diethylaminosulfur trifluoride (DAST) is an organic EO crystal. ZnTe (Rice *et al.* (1994)) and GaP (Chang, Divin, Liu, Williamson, Galvanauskas & Norris (2006)) crystals are commonly used to generate and detect THz waves. That is because these crystals enable a simple collinear experimental configuration at the optical pump's wavelength, since they match relatively well between the THz phase velocity and the optical group velocity of the optical pump. However, the nonlinear coefficient of the ZnTe crystal is relatively low and high energy THz pulses can only be generated by using a large aperture ZnTe crystal (Blanchard, Razzari, Bandulet, Sharma, Morandotti, Kieffer, Ozaki, Reid, Tiedje, Haugen et al. (2007)). On the other hand, although organic crystals such as DAST possess higher conversion efficiency, they normally suffer from a lower damage threshold compared to inorganic crystals (Kampfrath *et al.* (2013); Wu & Zhang (1995)). $LiNbO_3$ has a higher nonlinear coefficient (r33=30.9 pm/V) (Hebling, Almasi, Kozma & Kuhl (2002)) compared to a standard GaP or ZnTe crystal. Because of the significant difference in the refractive indices, a noncollinear configuration, which is a Cerenkov-type method based on a tilted front laser pulse, must be used to achieve proper phase-matching conditions. This method was proposed by Hebling et al.(Hebling *et al.* (2002)) to achieve a proper phase-matching condition in $LiNbO_3$ for efficient THz generation. Therefore, this crystal is currently being used as a THz source in many THz laboratories for generating intense THz pulses (Hirori *et al.* (2011)).

In fact, all of these factors have an impact on the THz generation efficiency, but phase-matching is the most important factor in a nonlinear process of OR.

1.3.2.1 Phase-matching condition

One way to enhance the sensitivity by increasing the interaction length of the crystal for broadband OR and EO sampling is to match the THz phase velocity and the optical group velocity (Nahata *et al.* (1996b)). One can use the EO sampling approach to detect THz radiation (This will be discussed further in the detection section of this chapter). Since the process is mediated by the non linearity of the material, the phase matching condition for such an interaction with the coherent length of $l_c = \pi/\Delta k$ is

$$\Delta k = k\left(\omega_{opt} + \omega_{THz}\right) - k\left(\omega_{opt}\right) - k\left(\omega_{THz}\right) \tag{1.9}$$

where, ω_{opt} and ω_{THz} are respectively the optical and THz frequencies, and k is the wave vector. The frequencies of $\omega_{opt} + \omega_{THz}$ and ω_{opt} lie in the optical regime. The matching of the THz phase velocity and the optical group velocity is critical for both an efficient OR and the EO sampling technique (Wu, Litz & Zhang (1996b)). The phase-matching condition should be satisfied by the following equation (Nahata *et al.* (1996b)):

$$k\left(\omega_{opt}+\omega_{THz}\right)-k\left(\omega_{opt}\right)=k\left(\omega_{THz}\right). \tag{1.10}$$

With this formula, we can represent radiated THz waves as the superposition of all frequency components in the optical pump beam. Furthermore, ω_{THz} is dependent on the crystal's second-order dispersion coefficient, the pump beam spectrum and the phase shift between the THz waves and the pump. Therefore, one may write, from Eq. (1.10),

$$\frac{k\left(\omega_{THz}\right)}{\omega_{THz}} \approx \left[\frac{\delta k}{\delta \omega}\right]_{opt} \tag{1.11}$$

Eq. (1.11) shows that, to avoid conversion cancellation due to phase mismatch, the crystal thickness must be greater than the coherence length, l_c, to create efficient THz radiation from a bulk crystal.l_c can be calculated as follows:

$$l_c=\frac{\pi c}{\omega_{THz}\left|n_{opt}\frac{dn_{opt}}{d\lambda}\right|_{opt}-n_{THz}\Big|}, \tag{1.12}$$

The EO coefficient of several high-dielectric-constant materials, such as $LiNbO_3$ and other ferroelectric materials, is extremely high. However, in these crystals, collinear velocity matching of optical and THz waves is not possible because the index of refraction in the THz range is more than two times greater than that in the optical pulse range, as shown in Table (1.1). Generating an efficient THz pulse is one of the critical elements in the real-time, near-field imaging system (Blanchard *et al.* (2011)) employed in this research. Therefore, the concept mechanism of generating an intense THz pulse by $LiNbO_3$ is described here as well.

1.3.2.2 Pulse-front-tilt

Hebling et al. developed a very efficient approach for generating intense THz radiation in 2002 (Hebling *et al.* (2002)), as was later demonstrated by the same team (Hebling *et al.* (2004); Stepanov, Hebling & Kuhl (2003)). Figure 1.5 shows the mechanics of the tilted-pulse-front method. The approach includes tilting the optical pump's pulse front to match the optical pulse's group velocity with the THz pulse's phase velocity, originally perpendicular to the optical beam's propagation path.

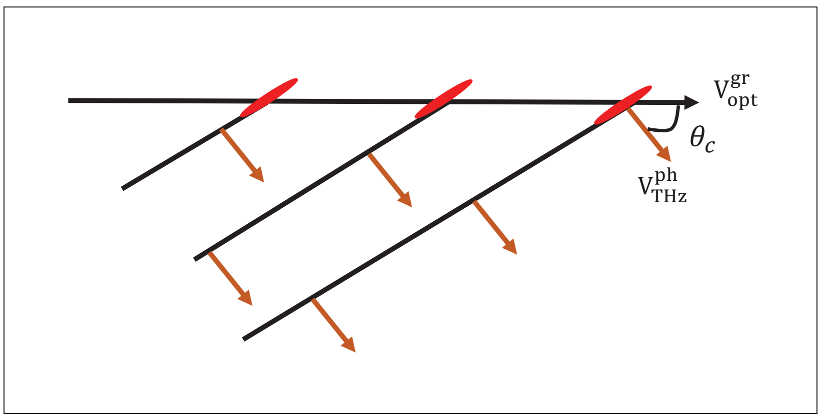

Figure 1.5 Generation of coherent THz radiation using a tilted-pulse-front geometry. This technique corrects the phase mismatch between optical and THz waves by tilting the pulse front of the optical wave, resulting in a new phase-matching condition. Thus, all the created THz radiations are in phase with one another

THz radiation stimulates in the direction of the tilted pulse front. The pump pulse travels at a velocity v_{opt}^{gr}, but this velocity is projected in the direction of propagation of the generated THz as $v_{opt}^{gr} \cos\theta_c$. The θ_c is the tilt angle introduced to match the THz and optical pulses' group and phase velocities, respectively. As a result, the phase-matching condition is represented by

$$v_{opt}^{gr} \cos\theta_c = v_{THz}^{ph}. \tag{1.13}$$

In a material with a large dielectric constant, this technique may be used to match the two velocities by selecting an appropriate tilt angle θ_c. A grating is commonly used to tilt the pulse front of an optical beam with respect to the phase front. Figure 1.6 shows a common grating-based approach for tilting the pulse front. The pulse front tilt angle θ_c is provided by the following formulas.

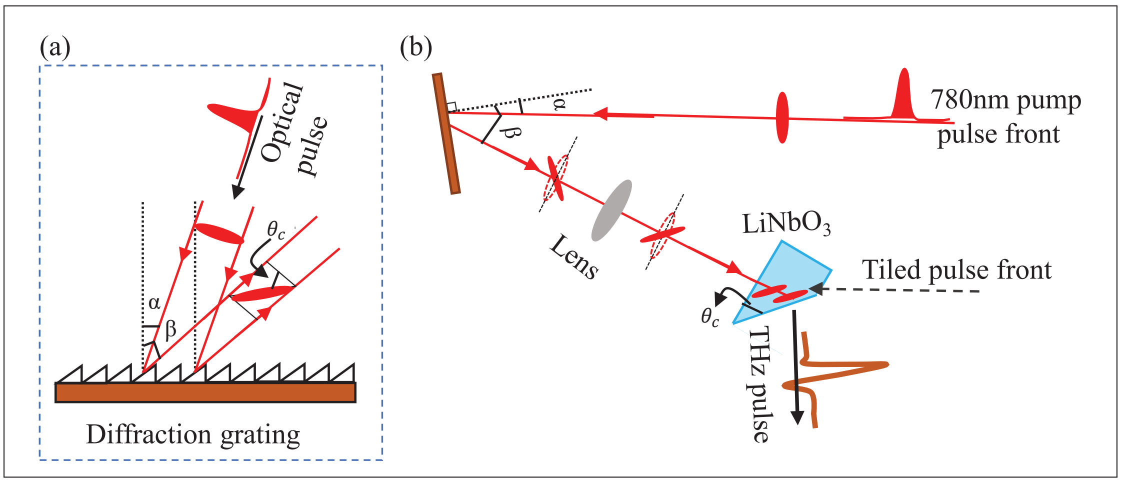

Figure 1.6 Illustration of (a) the scheme of pulse-front-tilt using a grating. An optical beam has an angle of α incident on the grating, with a pulse front and phase front perpendicular to the beam's propagation path. The pulse front of the grating is tilted by an angle θ_c after diffraction at an angle β. (b) shows a schematic diagram of THz generation via a $LiNbO_3$ crystal by the titled-pulse-front method

$$\tan\theta_c = \tan\beta + \frac{\sin\alpha}{\cos\beta}, \tag{1.14}$$

where there is an optical beam incident on the grating with an angle α that is diffracted by angle β. By considering the grating equation $\sin\alpha + \sin\beta = mN\lambda$ in Eq. 1.14 the pulse-front-tilt angle is given by:

$$\tan\ \theta_c \ = \ \frac{m\,N\,\lambda}{\cos\ \beta} \tag{1.15}$$

where α and β are the incidence and diffraction angles, respectively, as shown in Figure 1.6 (a) and (b). N is the number of grooves per millimeter of the grating, m is the order of diffraction, and $lambda$ is the wavelength of the optical beam. If F is the demagnification ratio of the lens used to image the beam spot on the grating at the crystal location, then n_{opt} is the index of refraction of the $LiNbO_3$ crystal with a tilt angle of θ_c.

$$\tan\theta_c = \frac{F}{n_{opt}}\frac{mN\lambda}{\cos\beta}, \tag{1.16}$$

where λ is the optical pump wavelength. To calculate the front tilt induced at the crystal location, one can use Equation (1.16). It is worth mentioning that it is necessary to cut the crystal at an angle, which meets the velocity matching condition within the crystal for the generated THz radiation.

1.4 THz Detectors

THz detection schemes are primarily classified as either coherent or incoherent techniques. The basic difference is that coherent detection measures both the amplitude and the phase of the field, whereas incoherent detection measures the intensity. Coherent detection techniques are linked with generation techniques as much as they share fundamental processes and critical components. THz detectors measure the transition of the electrical field of THz pulses by gating via a fs laser pulse. There are two standard methods to detect and measure THz radiation: photoconductive sampling using LT-GaAs (Ye, Zhang & Shen (2006)) and electro-optic sampling (Wu & Zhang (1996b)) using a nonlinear crystal.

1.4.1 Photoconductive Sampling

THz detection can be performed with a PCA similar to that used for THz generation. Unlike generation, however, there is no external bias for the metal gap fabricated on the semiconductor, as shown in Figure (1.7). The electrical field of the THz EM pulse creates electrical bias. In a way similar to generation, a laser beam focused on a semiconductor gap creates free carriers, that increase the conductivity of the PCA. Thus, a current is generated that is precisely proportional to the THz electric field. The detector's response function is affected by the laser pulse's duration

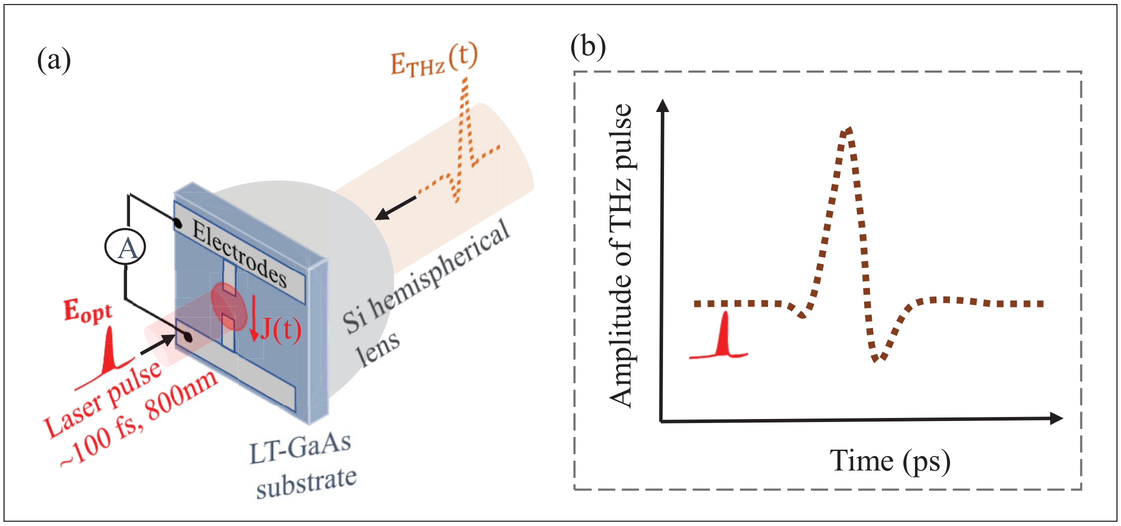

Figure 1.7 Demonstration of (a) THz detection using a photoconductive antenna (PCA) and (b) the THz waveforms are scanned using a fs laser pulse as an ultrafast detector

and the carrier's lifetime. Unlike the situation with generation, where input power also affects the length of the current pulse, here only the carrier lifetime is critical in detection. Short carrier lifetimes produce high temporal responses, resulting in wider THz bandwidths. In LT-GaAs, the carrier lifetime is typically between 100 and 300 fs. The THz-driven current ranges from picoamperes to nanoamperes. Measuring such tiny currents is difficult, mainly because of the thermal noise voltage, which is (Jaeger & Blalock (1997)),

$$U_{noise} = \sqrt{\frac{k_B T}{C}}, \tag{1.17}$$

where C is the capacitance which is approximately around 10 fF (femtofarad) (Jepsen, Jacobsen & Keiding (1996a)). Thus, noise voltage, U_{noise}, is around 650 μV. Since the dark resistance, R, of the PCA is in the order of 1 $M\Omega$, a current noise is up to $I = U/R = 650$ nA. Since such a signal's magnitude is low to detect, an amplifier is needed for the current. A lock-in amplifier can detect the current's amplitude.

1.4.1.1 Lock-in amplifier

Lock-in amplifiers are commonly used to detect weak signals in the presence of a noisy background. A lock-in amplifier is a device that selectively amplifies a signal at a set reference frequency f. The noisy input signal is multiplied by a sine wave at this reference frequency and then passes through a low-pass filter (LP) to retrieve the DC component that is the signal of interest. The time constant (τ) of the LP filter is a critical parameter, because, the lock-in amplifier averages the signal over a period, τ. The advantage of this averaging is to suppress some of the random noise and smooth the output signal. A considerable time constant and the delay line's scanning speed (ν) are important for efficiency of THz pulse. As the delay line moves, the signal changes because it monitors various time point of the THz signal. Therefore, selecting the right combination of lock-in time constant and scanning speed is critical (Neu & Schmuttenmaer (2018))..

When the scanning is done too quickly, the amplitude of the signal is substantially diminished. More crucially, because of the low pass filter properties of the combination of lock-in time constant and scanning speed, the pulse changes shape and becomes considerably longer in the time domain. The effect of this low pass filter on the THz signal can be described mathematically via convolution of the THz time-domain signal with a Gaussian function with a time constant of $\sigma = \tau\nu$. Therefore, when scanning is too fast, the THz pulse will be broadened and attenuated, but when scanning is too slow, there will be no additional improvement.

Using electrical modulation is often recommended with PCAs. Therefore, the THz time-domain signal is modulated by turning the generated THz on and off at the desired frequency, using an electronic chopper to improve the signal-to-noise ratio. However, the capacitance of the antenna, as well as the frequency response of the cables, amplifiers, and other equipment, limit the best possible modulation frequency.

1.4.2 Electro-Optic Sampling

The second detection technique, known as free-space electro-optic (EO) sampling, employs the linear Pockels effect in a nonlinear (EO) crystal to detect the THz quasi-DC electric field in regard to the optical beam (100 fs laser pulse). This scheme was simultaneously demonstrated by different groups in 1995 and 1996 (Wu & Zhang (1995); Wu, Hewitt & Zhang (1996a); Jepsen, Winnewisser, Schall, Schyja, Keiding & Helm (1996b); Nahata *et al.* (1996a). Figure 1.8) shows the working principle of this technique in which an optical beam must overlap spatially and temporally with a THz pulse inside an EO crystal.

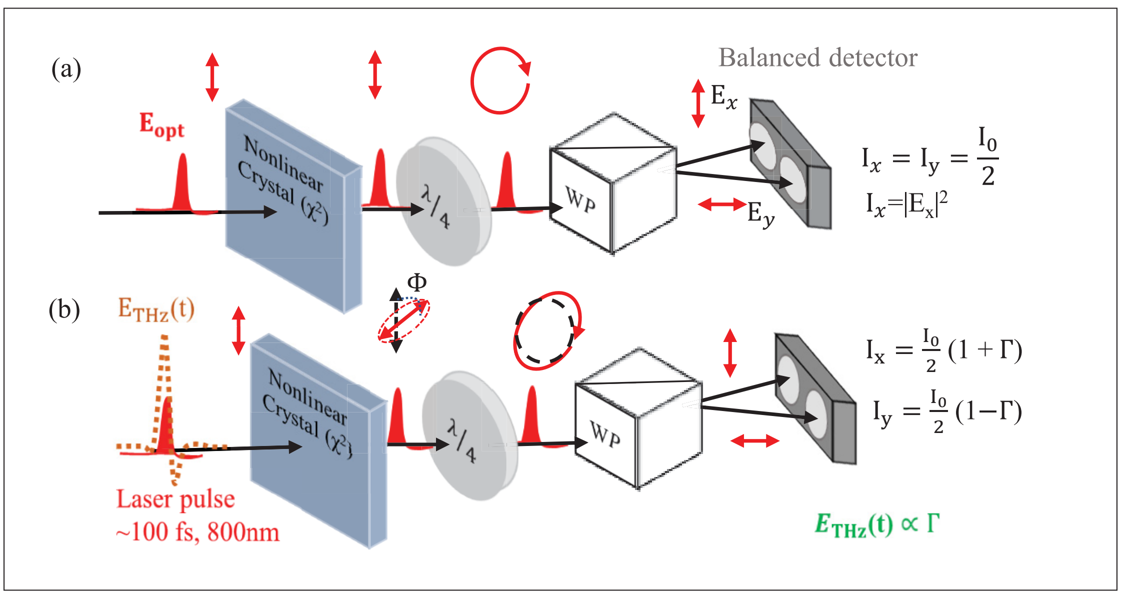

Figure 1.8 The configuration for detecting THz pulses via EO sampling (a) without and (b) with the presence of a THz pulse

Figure 1.8(a) shows a basic situation with the absence of a THz electric field. A quarter waveplate ($\lambda/4$) modifies the linearly polarized optical laser pulse to circular once it passes through an EO crystal. The optical beam is divided into orthonormal polarization components (i.e. S- and P-polarized beams) using a Wollaston polarizer (WP), which is comparable to a polarizing beam splitter (BS). Individual photodiode detectors detect both orthonormal polarization components. As a result of the circular polarization of the pulse, each photodiode detects an identical voltage.

Then it transmits to a lock-in amplifier, which subtracts the two and returns a zero reading. When a THz electric field overlaps with the optical beam in time, as shown in Figure 1.8(b), the polarization of the optical beam is changed by the strength of the THz electric field, which causes the Pockels effect in the EO crystal. This leads to an elliptically polarized optical beam after the quarter waveplate. The two voltage signals are then not equal after separation with WP, and lock-in will detect the differences as a signal by subtracting them, i.e. $I_x - I_y = I_0 \Gamma$. This signal is proportional to the THz electric field induced by phase change Γ. The entire THz waveform can be traced in time by scanning the time delay between the optical pulse and THz beams, as shown in Figure 1.7 (b). This phase changeΓ, for nonlinear detection crystals with an EO coefficient r_{41}, is given by

$$\Gamma \approx \frac{\pi L n_{opt}^3 r_{41}}{\lambda} E_{THz}, \tag{1.18}$$

where L is the thickness of the EO crystal, λ is the wavelength of the optical beam, n_{opt} is the refractive index of optical beam frequencies, and E_{THz} is the THz electric field (Lee (2009)). ZnTe is most widely utilized for OR and EO crystals, as described in the OR section of this chapter. However, GaSe, GaP, InP, GaAs, and DAST have also been utilized for EO sampling.

The bandwidth of the detected THz radiation is not limited only by the duration of the optical pulse. It is also essentially restricted by the phase mismatch between the THz pulse and the optical beam at 800nm (Nahata *et al.* (1996a)), as explained in the OR section. One way to improve the bandwidth is to use thin crystals, which decrease the impact of the phase mismatch. For example, using a very thin ZnTe crystal can increase the detection bandwidth to 100 THz (Kübler *et al.* (2005)). Another way is to perform a short scan by reducing the optical pulse duration via filters (Blanchard & Tanaka (2016); Ilyakov, Kitaeva, Shishkin & Akhmedzhanov (2016); Porer, Ménard & Huber (2014)).

The properties of EO sampling depend on various parameters, such as frequency-dependent phase-matching, reflection, dispersive propagation, and absorption. For example, Bakker et al. show that the oscillatory tail detected through the EO sampling results from the dispersive propagation of THz pulses via the EO crystal. In addition, the absorption and reflection in both generation and EO sampling detection cause this kind of misrepresentation, especially when there is a very broadband THz pulse (Bakker, Cho, Kurz, Wu & Zhang (1998)). Because of these characteristics of EO sampling, much research has been devoted to optimizing the EO sampling devices (Nahata *et al.* (1996b); Wu & Zhang (1997)). For example, Kitaeva et al. introduced the quasi-phase-matching probe energy technique to improve the sensitivity of the EO sampling technique. This method can be used in narrowband detection to measure the absorption and reflection of any material (Kitaeva, Kovalev, Naumova, Akhmedzhanov, Ilyakov, Shishkin & Suvorov (2010)). Because we used real-time THz near-field imaging with the EO sampling method in this work, we will discuss it in this section as well.

1.4.2.1 THz Near-field imaging

The THz frequency range offers new imaging and sensing capabilities for applications in material characterization (Mathanker, Weckler & Wang (2013); Blanchard *et al.* (2018)), microelectronics (Huber, Keilmann, Wittborn, Aizpurua & Hillenbrand (2008)), medical diagnosis (Yu *et al.* (2012)), and environmental control and chemical and biological identification (Walther, Fischer, Ortner, Bitzer, Thoman & Helm (2010)). However, the spatial resolution of the conventional THz imaging techniques is limited by diffraction of THz waves. While the best spatial resolution in a conventional, far-field, imaging set up can be determined by the Rayleigh criterion as

$$\Delta l = 0.61 \frac{\lambda}{n \sin(\theta)} \approx \frac{\lambda}{2NA}, \tag{1.19}$$

with λ the wavelength of the light in vacuum, n the refractive index of the medium, θ half of the opening angle of the focused light beam, and $n \sin(\theta)$ the numerical aperture (NA) of the focusing element. For $\lambda = 300\, \mu m$ (1 THz), the best obtainable spatial resolution in THz far-field microscopy is around $150 \mu m$. This means that the smallest spatial features that can theoretically be resolved are limited by diffraction to values of about half a wavelength.

To overcome this diffraction limit, THz near-field techniques have been developed. Some of these techniques are specific to the THz frequency range, while others are derived from comparable techniques used in other parts of the EM spectrum, such as the visible area. Many of these near-field methods have an unusual characteristic in that they measure the electric field rather than the intensity. This allows for studies of the near EM field with resolving power, defined as the ratio of spatial resolution to wavelength, and bandwidth that are virtually unattainable in the visible part of the EM spectrum. (Yuan, Xu & Zhang (2004); Lin *et al.* (2007); Adam (2011)). One of them is the aperture method, in which a THz wave is focused into a tapered metal-tip aperture while the sample is scanned in the near-field (Hunsche, Koch, Brener & Nuss (1998); Mitrofanov, Lee, Hsu, Brener, Harel, Federici, Wynn, Pfeiffer & West (2001); Chen, Jiang, Xu & Zhang (2000)), leading to a spatial resolution of less than 10 μm. The alternative method is THz apertureless near-field scanning optical microscopy (ANSOM), in which a sharp tip is substituted for the resolving aperture to combine the idea of collecting the optical field at the near-field of the surface of interest with the scanning probe microscopy technique (Chen, Kersting & Cho (2003); Huber *et al.* (2008)), resulting in a spatial resolution of 40 nm (Huber *et al.* (2008)). In addition, there is another method that utilizes the EO sampling technique; it allows the THz wave amplitude to be detected in the near-field region of the sample while the detector is scanned to obtain an image (Seo, Adam, Kang, Lee, Jeoung, Park, Planken & Kim (2007); Adam, Brok, Seo, Ahn, Kim, Kang, Park, Nagel & Planken (2008); Wang, Cui, Hu, Sun, Ye & Zhang (2009)). However, all the existing near-field THz systems, with high spatial resolution, are based on a raster-scanning technique, which requires long measurement times and is not compatible with immediate measurements on samples that are moving or evolving dynamically.

1.4.2.2 Real time THz near-field imaging

Alternatively, real-time THz near-field imaging (Blanchard *et al.* (2011); Doi, Blanchard, Tanaka & Tanaka (2011); Blanchard *et al.* (2013)), is two-dimensional THz imaging based on EO detection (Wu *et al.* (1996a)) and provides instantaneous measurements. The sensitivity of the detection part was traditionally not sufficient and had poor resolution (Wang *et al.* (2009)) because the CCD camera can not work with a lock-in amplifier and THz sources were rather weak at that time. Even though the sensitivity of the detection unit was improved by dynamically subtracting background images (Jiang *et al.* (2000b)), raster-scanning techniques have traditionally been used to obtain THz images (Adam (2011)), in particular, to access near-field information at THz frequency. The recent development of a THz source (Hirori *et al.* (2011); Blanchard, Ropagnol, Hafez, Razavipour, Bolduc, Morandotti, Ozaki & Cooke (2014a); Zhang, Ma, Ma, Wu, Ouyang, Kong, Hong, Wang, Yang, Chen et al. (2021a)) and the invention of a THz polaritons platform permit THz waves to propagate and modulate while being imaged at a frame rate of 1 Hz (Feurer, Stoyanov, Ward, Vaughan, Statz & Nelson (2007); Werley, Wu, Lin, Tait, Dorn & Nelson (2010)).

The THz microscope consists of three main parts, as shown in Figure 1.9: a high-intensity THz pulse generator (Figure 1.9a); an EO crystal for near-field THz detection (Figure 1.9b); and a balanced imaging scheme, which includes a polarization sensitivity analyzer section (Figure 1.9c). The generating part is based on the current optical rectification approach (Hirori *et al.* (2011); Blanchard *et al.* (2011)) in $LiNbO_3$ (LN) through tilted-pulse-front excitation (Hebling *et al.* (2002)). A peak electric field of more than 1 $MVcm^{-1}$ is very important (Hirori *et al.* (2011)) to have a sufficient SNR for near-field imaging using a thin-film.

Free-space 2D EO sampling (Blanchard *et al.* (2011, 2013); Doi *et al.* (2011)) is used to detect the pulse THz waveform in a thin x-cut LN crystal that is placed on a sub-millimeter thick glass, which can be reconstructed using an optical delay stage. Sensor thicknesses have a direct impact on the linear spatial resolution of the EO THz microscope system, as detailed in Blanchard *et al.* (2013) and Doi *et al.* (2011). However, because detection sensitivity is proportional to EO crystal thickness (Yariv (1989); Van Der Valk, Wenckebach & Planken (2004)), for two-dimensional near-field acquisition, a material with a larger EO coefficient is preferred. The sample is put immediately on top of the EO crystal to study the near-field area (Winnewisser, Jepsen, Schall, Schyja & Helm (1997b)). For the probe light at 780 nm, for example, the top and bottom surfaces of the EO crystal must have a high-reflection and anti-reflection coating. The best SNR performance can be attained with data averaging and the dynamic subtraction approach (Jiang,

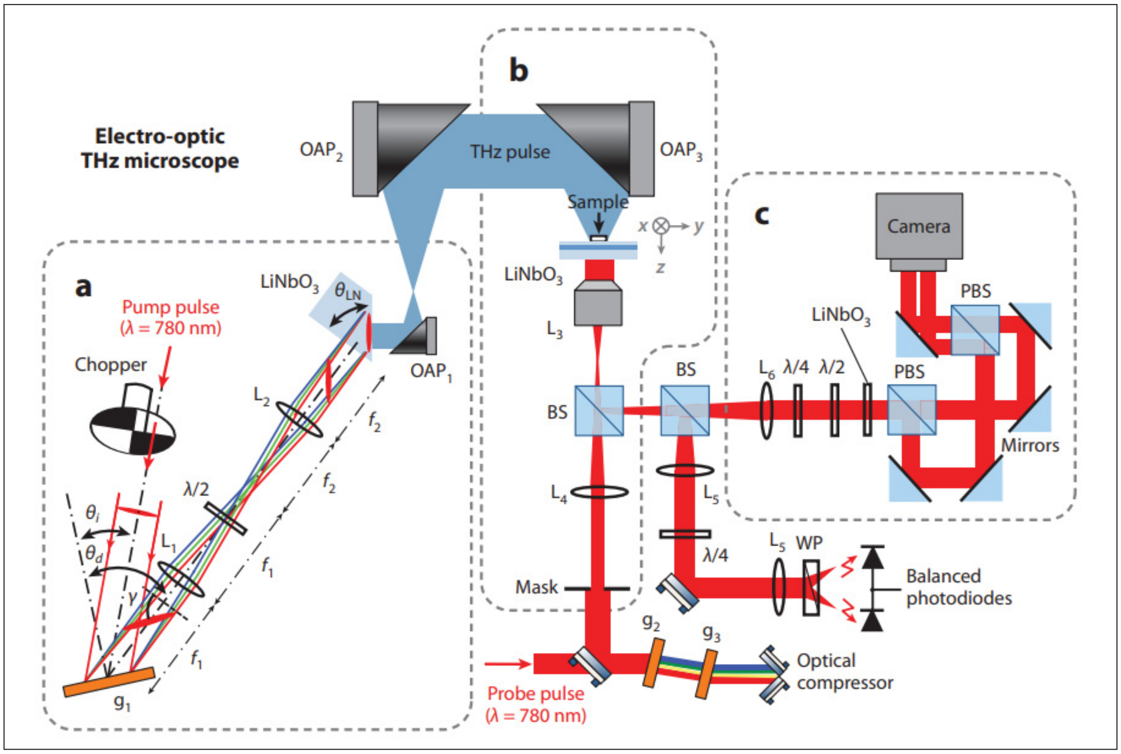

Figure 1.9 THz EO near-field microscope (a) THz pulse produced by tilted pulse front excitation. (b) THz pulse sensing in the near-field area using a thin LN EO crystal. (c) Image splitting for balanced imaging. Other abbreviations include: f, focal distance; BS, beam splitter; g, grating; OAP, off-axis parabolic mirror; L, lens; PBS, polarized beam splitter; γ, tilted angle; WP, Wollaston prism; θ_d, diffracted angle; LN, LiNbO3 cut angle; I, incident angle; $\lambda/4$, quarter-wave plat; $\lambda/2$, half-wave plate Taken from Blanchard *et al.* (2013)

Li & Zhang (2000a)). The time between camera and laser synchronizations must be taken into account. The reflected images are collected by a CCD camera with a non-polarized BS cube and returned to the objective lens. A second 200-mm focal length achromatic lens is employed to send the image to the camera. A combination of a quarter-wave plate, a half-wave plate, and two polarising BS cubes is used to detect THz-induced birefringence inside the EO crystal, as shown in the analyzer section of Fig. 1.9c. In addition, to enhance the SNR and image acquisition time, a balanced imaging technique is utilized. One camera is used to spatially separate and capture the vertically and horizontally polarized probe images concurrently (Blanchard *et al.* (2013)). All the related pixels (from both the S and P polarized images) are grouped together. In real time, all the related pixels (from both the S and P polarized pictures) are subtracted, yielding background-free images per second.

In fact, two requirements must be met for two-dimensional EO THz imaging to obtain high linear spatial resolution. THz pulses must be recorded in the near-field area before diffraction, and the probe pulse imaging unit's performance must match the necessary spatial resolution (e.g., within a wavelength's distance from the sample). All of the probing beams that geographically and temporally coincide with the THz electric field within the EO crystal create an image, according to these conditions. Simple calculations based on Fraunhofer diffraction of a small, square aperture are used to predict the dominating parameter for high-spatial-resolution EO imaging (Doi *et al.* (2011)). The following grating equation can be utilized with a diffraction grating of N grooves (mm^{-1}) (i.e. cycles (mm^{-1})):

$$NA = n_{NIR}\,\sin\theta = N(z)\,m\,\lambda_{NIR}, \tag{1.20}$$

where,θ is the angle between the diffracted and incident light, m is the diffraction order, and λ_{NIR} is the wavelength of the probe beam (780 nm). A point source is assumed at each z position inside the crystal. The NA of the point source is determined by the THz amplitude distribution, and the probe beam is treated as coherent and collimated light propagating along the z-axis to meet the experimental conditions.

One of the applications of real-time EO THz microscopy is to capture immediately the laterally propagating electric field near a sample. This feature is useful for mapping samples with desired dielectric orientation structures such as metamaterials. This potential is widely used to study and map radiation patterns of metamaterials such as the split-ring resonator (SRR) using an EO THz microscope (Blanchard *et al.* (2011); Blanchard, Ooi, Tanaka, Doi & Tanaka (2012)).

Metamaterials can be utilized to increase the sensitivity and resolution of THz microscopy systems since they are resonant devices. To accomplish field enhancement inside of the resonator unit, we can build a metamaterial (such as SRR) with a suitable effective wavelength (Razzari, Toma, Shalaby, Clerici, Zaccaria, Liberale, Marras, Al-Naib, Das, De Angelis et al. (2011)).

This is because this device transforms free-space propagating optical radiation into confined energy and the other way around (Bharadwaj, Deutsch & Novotny (2009)). Such resonator structures are expected to enhance the field at the sample's contact point (Novotny & Van Hulst (2011)), therefore immediately enhancing sensitivity in THz microscopy.

1.4.2.3 Metamaterial-SRR

Metamaterials are artificially engineered materials with distinctive EM properties. They offer a new approach to designing unique material properties that do not exist in nature. These materials consist of unit cells in a uniform matrix (Smith, Pendry & Wiltshire (2004); Yen, Padilla, Fang, Vier, Smith, Pendry, Basov & Zhang (2004)) instead of molecules or atomic structures in ordinary materials. The EM wave interacts with the metamaterial structure in which their unit cells are smaller than the wavelength of the EM wave, which is the fundamental concept. Furthermore, this structure responds to EM waves similarly to a homogeneous medium material, i.e. a crystal structure. The EM properties of a metamaterial are usually characterized by effective permeability (μ) and effective permittivity (ϵ). One can change the response of a metamaterial by manipulating the elements of its structure. Therefore, one can design the desired structure for a particular optical response from the material even though it is not available in nature. Negative refractive index metamaterials were first predicted by Victor Veselago (Veselago (1968)). They are the composite medium which acts as negative μ and ϵ in the microwave range (Smith, Padilla, Vier, Nemat-Nasser & Schultz (2000)), radio frequency (RF) metamaterials (Wiltshire, Pendry, Young, Larkman, Gilderdale & Hajnal (2001)), and THz metamaterials (Yen *et al.* (2004)).

A popular common metamaterial unit cell is SRR, which has a structure size smaller than the wavelength and consists of a metallic ring separated at one point by a gap (Pendry, Holden, Robbins & Stewart (1999)). According to the structure and material of the unit cell, we can have different resonance frequencies. For example, SRRs are usually used as magnetic resonators in metamaterials (Yen *et al.* (2004)) and are generally composed of highly conductive metals (such as gold).

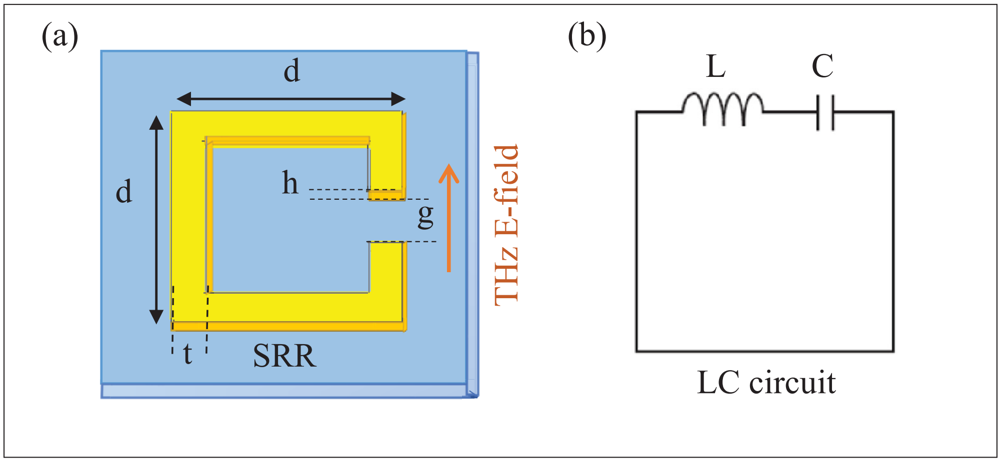

Figure 1.10 Illustration of (a) a single split-ring resonator (SRR) design and (b) the equivalent LC circuit. The polarization of the incident THz electric field is parallel to the gap. It causes the current to flow across the resonator's arms, resulting in a single magnetic dipole for the SRR

The design of a single SRR is shown in Figure 1.10a, where d denotes the length of the arm, t the width of the arm, g the gap width, and h the thickness of the split-ring resonator's metal. An SRR can be represented by an LC circuit, as shown in Figure 1.10b. The capacitance C is proportional to the charge density at the gaps, whereas the inductance L is proportional to the current flowing through the resonator (Azad, Taylor, Smirnova & O'Hara (2008)). A SRR's capacitance (C) is often estimated by the following formula (Linden, Enkrich, Dolling, Klein, Zhou, Koschny, Soukoulis, Burger, Schmidt & Wegener (2006)):

$$C = \epsilon_0 \, \epsilon_g \, \frac{h\,t}{g}, \tag{1.21}$$

where ϵ_g is the effective relative permittivity of the material in the gap, and ϵ_0 is the vacuum permittivity. The dielectric constant of the substrate as well as the medium inside the gap, influence ϵ_g. A SRR's inductance (L) is determined by the geometric form of the ring that is provided for a planar square split-ring resonator by the following (Yen *et al.* (2004)):

$$L = N \, \mu \, \frac{d^2}{h} = \mu_0 \, \frac{d^2}{h} \tag{1.22}$$

Here, N equals one, which is the coil's number. μ is absolute permeability, which equals $\mu_r\mu_0$. And μ_r and μ_0 represent relative permeability and free space permeability, respectively. In this case, μ_r equals 1 for air. The resonance frequency is determined by the following formula (Linden *et al.* (2006)):

$$f_{LC} = \frac{1}{2\pi\sqrt{LC}}. \tag{1.23}$$

Since this SRR's resonance frequency is determined by its dimensions, it can be adjusted by scaling the geometrical parameters of the SRR. The THz electric field couples to the SRR and creates a current in the loop when the incident electric field is parallel to the arm holding the gap of the SRR. In the SRR, the circulating current creates a magnetic field. The magnetic field produced by the current is greatest at the SRR's resonance frequency, which is dictated by the loop inductance and gap capacitance as shown in Figures 1.10(a) and 1.10(b).

1.5 Terahertz time-domain spectroscopy

The study of the energy, wavelength, or frequency of photons passing through a material sample is known as spectroscopy. Since the 1950s, spectroscopy in the far-infrared region has become possible by the development of Fourier Transform Infrared (FTIR) spectroscopy (Loewenstein (1966); Möller & Rothschild (1971)). The FTIR method records the information by the path difference-domain (also known as time difference). This method provides a quick data acquisition process, improves the signal-to-noise ratio, and limits the detector noise level instead of the source noise level (Fellgett (1949)). Nevertheless, the low-energy photons of FTIR sources, low-resolution in the FIR region, and lack of proper optical elements (e.g. BSs) are disadvantages of this method (Storm, Halvardsson, Heurlin, Lindgren, Gustafsson, Wu, Monemar & Samuelson (2012). Moreover, this method cannot directly characterize a material because it provides only the intensity of the light transmission without phase parameter information (Dexheimer (2007)).

In the 1980s fs lasers brought about an alternative spectroscopy method in the THz region which opened a new door to materials characterization. Furthermore, the mode-locked fs laser introduced in the 1990s has significantly improved the usage of time-domain spectroscopy studies on different materials (Han & Zhang (2001)). This method, which is based on the optical excitation of photoconductive dipole antennas, is known as THz-TDS (Van Exter, Fattinger & Grischkowsky (1989)). It is closely connected to the developments of Ti:sapphire fs laser technologies, also known as ultrafast laser technology (Hilton, Prasankumar, Trugman, Taylor & Averitt (2006)).

In this section, the principle of the THz-TDS system will be discussed. As this technique is used mainly for characterization and sensing applications, how to find the properties of a material sample as a function of frequency is explained as well as the concept of using Fourier Transformation. Since derivative spectroscopy is an additional method to characterize materials that has been used in this research project, we also review THz differentiators, which are the key modulators to provide THz derivative spectroscopy. In addition, to understand the concept of THz derivative spectroscopy, the use of this technique at other frequencies for characterization of materials is discussed.

1.5.1 Principles of time-domain spectroscopy

The principles behind THz-TDS are linked to microwave technology alongside the previous developments in FTIR systems. The THz-TDS technique is a convenient spectroscopic method with well-covered wavelengths, sufficient frequencies, spatial resolution, and high sensitivity. THz-TDS methods are able to directly obtain phase-locked field measurements at a high frequency. Therefore, THz-TDS techniques can quickly probe fs changes in different structures owing to their coherent generation and detection techniques.

The time-domain signal in THz-TDS directly detects the transient electric field rather than its intensity. The electric field is generally measured by the detector (Jepsen *et al.* (1996a)) with a time duration of a few picoseconds. Therefore, a fast and sensitive detection method is necessary to measure the electric field. To achieve sub-picosecond resolution, these optical methods use an ultrashort optical pulse (often less than 100 fs) to generate and measure the time-dependent THz field. A fs laser pulse ($\lambda = 800nm$) is used to sample an unknown THz field. For this, the

THz-TDS technique utilizes the convolution of a short optical pulse (e.g. 100 fs) with a longer THz pulse. There are several different methods in the detection part of THz-TDS to perform this convolution. These detectors all have one thing in common: they measure the THz field rather than intensity. When the optical and THz pulses arrive at the same time, all detectors are too slow to measure instantly the signal with a picosecond resolution. Therefore, instead of direct measurement, the measured signal, X(t), is generally determined by the convolution of both pulses as follows,

$$X(t_1) \propto I_{opt}(t) \circledast E_{THz}(t_1), \tag{1.24}$$

where $E_{THz}(t_1)$ is the THz electric field at a single point in time $t_1$and $I_{opt}(t)$ is the intensity profile of the optical laser pulse. As the optical laser pulse is much shorter than the THz pulses, it can be considered a delta function ($I_{opt}(t) \approx \delta(t)$):

$$X(t_1) \propto \delta(t) \circledast E_{THz}(t_1) = E_{THz}(t_1). \tag{1.25}$$

Practically, the detector will be active only if both pulses arrive at the same time and the optical pulse is much shorter than the THz pulse. This enables us to measure the THz field as a function of time. Furthermore, the detector is sensitive to electric field signs. In contrast to previous approaches (FTIR methods) that measure just the intensity $\left|E^2(t)\right|$ of an EO signal without capturing the phase information, we measure the amplitude E(t), which is time dependent. To measure the THz signal at all time-points, we delay the optical laser pulse into the THz electric field with a mechanical delay line.

Figure 1.11 shows a schematic illustration of a typical experimental design for THz-TDS systems. In general, a fs laser pulse is divided into two paths through a BS. One of the beams is used to generate THz radiation, and the other (shown in dashed line) is used for detection. The time delay is created by extending one of the beams' trail lengths. The laser pulse's transmission time is $t = l/c$, where c is the speed of light (30 cm/ns or 300 μm/ps) and l is the length of the optical path. This reduces the fs temporal resolution challenge to one micrometer spatial resolution. Precision micro-positioning is achieved by computer-controlled positioning stages. In general,

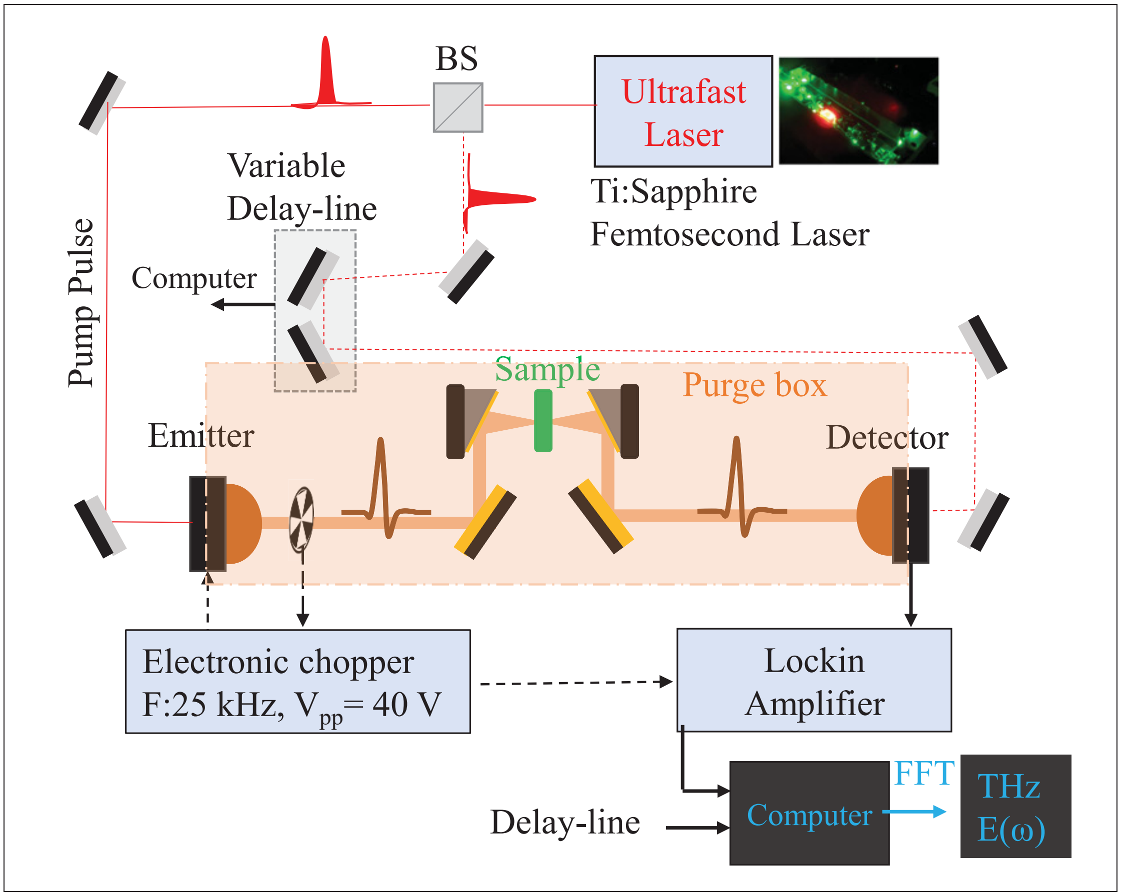

Figure 1.11 A THz time-domain spectrometer (THz-TDS) uses a photoconductive antenna (PCA). The output pulse of a fs laser is split into two beams by a beam spliter (BS). One beam is routed through a delay line and is used to generate THz radiation. The other beam is used to detect the THz beam. The black lines represent signal connections, with the modulation frequency being input by a chopper and the detected signal being sent to a lock-in. A signal from the delay line and the lock-in output is sent to a computer for data analysis

these stages are commonly referred to as delay lines in THz-TDS. For each micrometer of delay line movement, the round trip delay time varies by 6.6 fs (for example). The sampling speed in the time domain is defined by the movement speed of the delay line. As a result, the delay line's speed is commonly expressed as ps/s.

Water vapor in the air has high THz absorption characteristics, which can affect the detection of a THz electric field (Van Exter *et al.* (1989); Xin, Altan, Saint, Matten & Alfano (2006)).

Therefore, in the THz setup the THz beam path is contained in a purge box, as shown in Fig. 1.11; it is purged with dry air or nitrogen to reduce this absorption. Once THz pulses are generated, they pass through a material sample that is placed at the focusing point of off-axis mirrors. After the interaction of the THz pulse with the sample, a detected signal proportional to the THz electric field is recorded. The probe beam is delayed with respect to the pump beam through the transit mechanical stage for probing the THz field at different times.

The THz-TDS system sketched in Fig.1.11 employs the simplest THz-TDS geometries. In alternative geometry, the THz pulse reflected from the sample (Howells & Schlie (1996); Thrane, Jacobsen, Jepsen & Keiding (1995)) can also be measured. Furthermore, THz-TDS can be utilized to identify a sample in the near-field (Neu, Krolla, Paul, Reinhard, Beigang & Rahm (2010); Blanchard *et al.* (2013); Bitzer, Merbold, Thoman, Feurer, Helm & Walther (2009); Blanchard *et al.* (2018)). The THz-TDS technique measures the transition between the time resolved in the electric field of THz waveform transmission via a sample and an equivalent length in free space. The transitions in THz waveform shape depend on the sample geometry, which allows obtaining the complex refractive index of the sample material and characterizing the properties of the sample, such as absorption, the dielectric constant, and surface impedance.

THz-TDS is a highly sensitive, coherent method that is inherently phase-modulated, allowing access to the temporal field pulse of the detected THz. The interaction of an electronic field with a sample is linear. In addition, Maxwells equation (Dexheimer (2007)) describes the propagation through a material with basic parameters given by permittivity and permeability. Therefore, the linear description concept is employed to respond to the time domain pulse in the frequency domain as a superposition of plane waves of frequency ω, all with a κ vector along the THz system's optical Z-axis (Tonouchi (2007)).

1.5.1.1 Fourier transformation

The spectrum information of the THz pulse is obtained by Fourier transformation of the observed THz transient electric field, as shown in Figure 1.12.

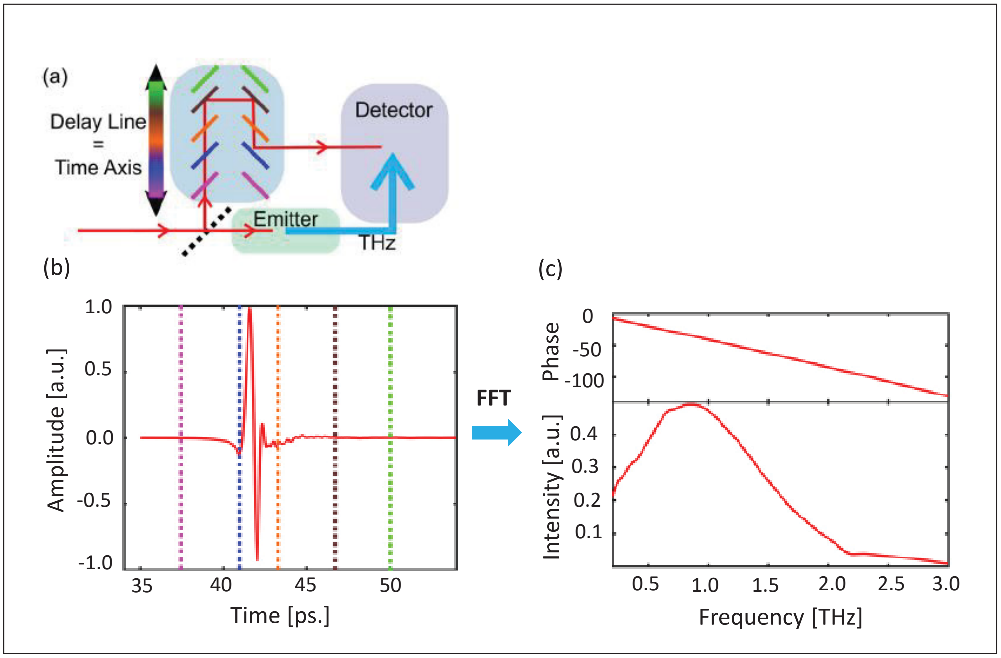

Figure 1.12 Illustration of (a) quasi-dc THz pulse detection at different delay-line positions shown with different colors in TDS; (b) illustrates several time points in the recorded THz time-domain signal that are matched to these places; and (c) shows the unwrapped phase and amplitude, which is obtained by the Fast Fourier Transform (FFT) of a THz signal
Taken from Neu & Schmuttenmaer (2018)

A complex-valued frequency-domain spectrum is the Fourier transform of a real-valued time-domain pulse, as defined by (Mathews & Walker (1970))

$$E(z,\omega) = \frac{1}{2\pi}\int_{-\infty}^{\infty} E(z,t)e^{-i\omega t}\,dt \tag{1.26}$$

where, E(z,ω) is the complex field amplitude and E(z,t) is an experimentally measured THz pulse electric field in the time domain. Figure 1.12(a) illustrates a simplified THz-TDS and (b) a recorded THz time trace with (c) its complex FFT in the frequency domain. The complex spectrum is characterized according to amplitude, $E(\omega)$, and phase, $\Phi(\omega)$, as described by

$$E(z,\omega) = E(\omega)e^{i\Phi(\omega)} \tag{1.27}$$

THz-TDS, in fact, has a significant advantage over broadband infrared, and visible spectroscopy in that it provides amplitude and phase information. This means that one may directly measure the spectrum without using the Kramers-Kronig relationship and determine the complex-evaluated refractive index $n(\omega)$ (Jackson (1999)).

1.5.1.2 Characterize material with TDS

THz-TDS has been used to investigate molecules in the gas phase (Mittleman, Jacobsen, Neelamani, Baraniuk & Nuss (1998); Harde, Katzenellenbogen & Grischkowsky (1994); Xie, Yao & Ying (2014); Mathanker *et al.* (2013)), solutions and liquids (Ikeda, Matsushita, Tatsuno, Minami, Yamaguchi, Yamamoto, Tani & Hangyo (2005); Reinhard, Schmitt, Wollrab, Neu, Beigang & Rahm (2012); Møller *et al.* (2009)), and solid states (Hangyo, Tani & Nagashima (2005); Neu, Nikonow & Schmuttenmaer (2018); Yu, Zeng, Yang, Xing, Chechin, Xin, Zeylikovich & Alfano (2004); Smith & Arnold (2011); Kong, Wu, Wang, Gao, Dai, Wang, Ruan & Miao (2018)). All these applications have the same goal of determining the sample's frequency-dependent complex refractive index. For example, to obtain the refractive index of the material sample via the THz-TDS system, one can record the electric fields of transmitted THz pulses with and without the sample, which permits characterizing the sample's properties. Therefore, the transfer function, $t(\omega)$, calculated is defined by the division of the amplitude of each field, as shown in the equation below:

$$t(\omega) = |t(\omega)|\, e^{i\omega t} = \frac{E_s(\omega)}{E_r(\omega)} \tag{1.28}$$

where $E_s(\omega)$ and $E_r(\omega)$ are the Fourier transforms of the THz field pulse propagation through the sample and air (reference), respectively. From the Fourier transforms of the THz field waveform the transmission of the sample and air, Eq. 1.27, one can access the real part, which is the refractive index $n(\omega)$, and the imaginary part, the absorption coefficient $\alpha(\omega)$,

$$n(\omega) = -\Phi(\omega)\frac{c}{\omega d} + 1 \tag{1.29}$$

$$\alpha(\omega) = \frac{2}{d}\, ln\left(\frac{(n(\omega)+1)^2}{4\,n(\omega)}\,|t(\omega)|\right) \tag{1.30}$$

where,

$$\Phi\,(\omega) = \Phi_r\,(\omega) - \,\Phi_s\,(\omega) \tag{1.31}$$

The full dielectric response of the sample can be determined easily using equations 1.29 and 1.30, where d is the sample's thickness (Dexheimer (2007); Jepsen *et al.* (1996a)). The THz-TDS method is basically used for transmission evaluation of materials. This method provides changes in the phase and amplitude of THz radiation, which is passed through the sample material. The material response to THz EM waves therefore can be measured via these changes. This response of the material helps us to understand and study the properties of the material.

1.5.2 THz differentiators

A simple method to convert a THz time-domain spectrometer to a THz time-domain derivative spectrometer is to place THz differentiators in the THz path to create a derivative THz wave. Differentiators perform mathematical operations of differentiation (Gilat (2013)) in signal processors for signal generation and fast computing (Salem *et al.* (2013); Ashrafi & Azaña (2012)) which are very important for high-speed THz characterization and measurement. A temporal differentiator transforms an input signal into an nth-order derivative output signal that could be a function of time (Ngo, Yu, Tjin & Kam (2004)). For example, a fundamental first-order THz differentiator provides the first-order time derivative of the input signal's electric field.

Figure 1.13 illustrates the operation of a THz temporal differentiator, which can be considered as a high pass filter for performing effective filtering functions on an incoming optical signal. Several techniques for realizing the optical differentiator and obtaining the derivative signal have been proposed, including fiber grating, temporal lensing, and EO effects (Ashrafi & Azaña (2012); Zhang, Wang, Zhang, Ai, Liao, Hsieh, He, Chen, Hu, Zhang et al. (2021c); Azaña (2010)). They are used in the near-infrared frequency. There are, however, only a few THz

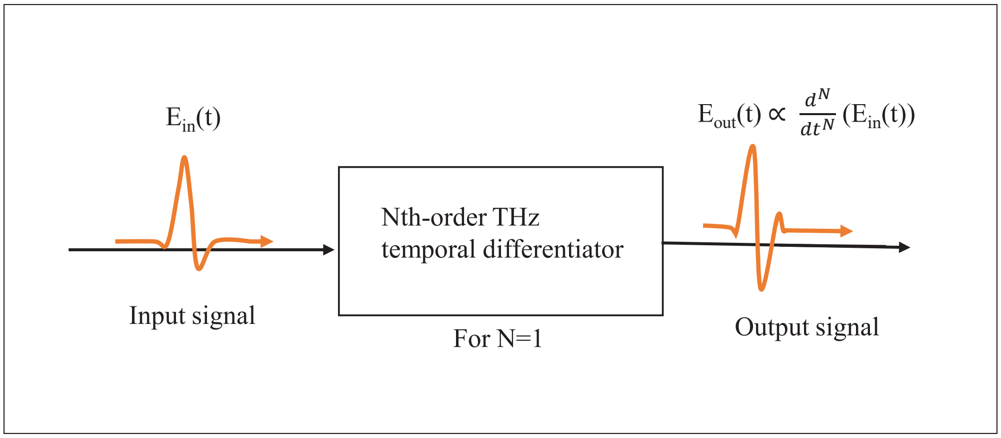

Figure 1.13 Showing a first-order (N=1) optical temporal differentiator schematic

temporal differentiators that are based on a metallic grating and an on-chip high-quality factor silicon resonator (Filin *et al.* (2001); Xie *et al.* (2020)).

1.5.3 THz derivative spectroscopy

Derivative spectroscopy (Karpińska (2004)) is a basic differentiation methodology. It is often used in the UV-visible (Vogt, Klocke, Rebstock, Schmidtke, Wander & Tacke (1999); Karpińska (2004)) and near-infrared (Wiley *et al.* (2009); Ortiz (2011)) frequencies in the literature. In these methods, the wavelength or frequency derivative of an absorption spectrum often enhances the apparent resolution of the spectrum. The time derivative of an absorption characteristic at a fixed wavelength is also commonly used to calculate the rates of chemical or photochemical processes. Derivative spectroscopy is generally defined in the literature as a technique based on spectra derived from a zero-order basic spectrum. It has been used both qualitatively and quantitatively in the study of chemical and medicinal compounds to detect the presence of certain components (Karpińska (2004); Lee (1992)). For example, near-infrared derived reflectance is widely used to increase the resolution of spectral data (Wiley *et al.* (2009)) and can detect wavelengths with significant variations in the contribution of chemical bonds. In reality, however, gain size and moisture content are sensitive to reflectance spectra and can change the shape of reflectance spectra as a result of scattering and absorption. Calculating the derivative of the reflectance spectrum to eliminate these matrix effects could help reduce these effects. Thus, reflectance derivative spectroscopy can detect the presence of certain components both qualitatively and quantitatively.

There are some advantages to using first-, second-, third- and higher-order derivative spectroscopy (O'Haver, Fell, Smith, Gans, Sneddon, Bezur, Michel, Ottaway, Miller, Ahmad et al. (1982)). For the first derivative, zero values precisely determine the wavelengths at which peak maxima and minima occur in the function being differentiated; and because the derivative of a constant is zero, it removes the background constant. For the second derivative, it provides a moderate resolution improvement, since zero values accurately identify the wavelengths at which peak maxima and minima occur in the first derivative, and the background linear trend is removed. The third, fourth, and higher derivatives all offer comparable benefits, with each offering increased resolution.

As the THz frequency (far-infrared) spans between the infrared (IR) and microwave portions of the EM spectrum, it has nearly the same qualities for the characterizing materials as the IR frequency. It may, for example, offer similar advantages as the near-infrared derivative spectrometer. On basic principles, the mathematical differentiation strategy used in spectroscopy differs from the optical differentiation technique. The derivatives are obtained in the optical portion of the instrument, which is known as modulation spectroscopy and is also a useful technique in physics. One can use FFT to study the properties of the differentiation method. There is a method that uses a resistor-capacitor (RC) filter to obtain the derivative of an input optical signal (Klein & Dratz (1968)). Moreover, The technique of derivative spectroscopy is presented as an efficient tool to filter out undesirable components in the source spectrum (Stauffer & Sakai (1968)). However, this method has not been demonstrated in the THz frequency range.

1.6 Summary

This chapter outlines THz sensing techniques and how we can increase their sensitivity. It describes the THz sensing methods that are now available for material characterization applications, their principles, and applications; it ultimately provides a specific way to develop these techniques in this research as well. We highlight that there are several ways to increase the sensitivity of these techniques for sensing applications. The goal of this PhD thesis is to offer new techniques that will definitely allow the development of a range of new uses and will therefore contribute to the enrichment of scientists' knowledge.

The following three chapters of this thesis present the novel THz EO thin-film characterization method, that is, the modulation and optimization method for THz waves to support THz sensing techniques. Chapter 2 discusses all the field distributions of SRRs, including the electric and magnetic fields in three dimensions (x, y, z) as a function of the exciting and probing beam polarizations using finite difference time domain (FDTD) simulation. Then, the use of intense THz near-field microscopy to characterize an LN crystal as a sensor is discussed. This is followed by an analytical study of LN crystal parameters in order to show their sensitivity as a function of the polarization of the applied electric field and optical probe polarizations. Later, using these parameters, an analytical study is presented on how to calibrate the method that has been introduced. In the next chapter, a new method is introduced by using a new device in the THz path to modulate the THz wave. This is followed by an explanation of the characteristics of the device and its function in order to understand how the THz wave is modulated. Finally, the newly introduced method is optimized by using another new device with a better function, which is discussed in Chapter 4, to achieve better performance in the modulation of THz waves that have various derivative orders. These introduced methods could open possibilities for increasing sensitivity in THz sensing in THz systems as needed.

CHAPTER 2

CHARACTERIZATION OF THIN-FILM OPTICAL PROPERTIES BY THZ NEAR-FIELD IMAGING METHOD

Fatemeh Amirkhan[1] , Ryo Sakata[2] , Kenji Takiguchi[2] , Takashi Arikawa[2] , Tsuneyuki Ozaki[3] , Koichiro Tanaka[2] , and François Blanchard[1]*

[1] Department of Electrical Engineering, École de technologie supérieure,
1100 Notre-Dame West, Montreal, Quebec, Canada H3C1K3
[2] Department of Physics, Kyoto University,
Kyoto, Japan
[3] Institut national de la recherche scientifique,
Varennes, Quebec, Canada J3X 1P7

Paper published in Journal of the Optical Society of America B (JOSA B), September 1, 2019.

Résumé

Nous présentons une nouvelle méthode pour caractériser les matériaux électro-optiques en couche mince. Cette méthode est basée sur la résolution des distributions des champs électriques et/ou magnétiques dans la région de champ proche d'un résonateur à anneau divisé (SRR) conçu pour la gamme de fréquences térahertz (THz). Nous validons expérimentalement nos simulations par l'imagerie en champ proche THz de SRRs directement modelés en contact avec un cristal de niobate de lithium en couche mince comme capteur. De plus, nous étudions analytiquement l'effet des différentes polarisations du champ électrique appliqué et calculons la sensibilité du capteur via différentes polarisations des faisceaux de sonde.

2.1 Abstract

We present a new method to characterize thin-film electro-optic materials. The method is based on resolving the electric and/or magnetic field distributions in the near-field region of a split-ring resonator (SRR) designed for the terahertz (THz) frequency range. We experimentally validate our simulations by THz near-field imaging of SRRs directly patterned in contact with a

thin-film lithium niobate crystal as a sensor. Furthermore, we analytically study the effect of the different applied electric field polarizations and calculate the sensitivity of the sensor via various polarizations of probe beams.

2.2 Introduction

The optical properties of thin-film electro-optic (EO) and magneto-optic (MO) materials are important due to their wide range of applications (Wooten, Kissa, Yi-Yan, Murphy, Lafaw, Hallemeier, Maack, Attanasio, Fritz, McBrien et al. (2000); Datta & Das (1990); Tang, Towner, Meier & Wessels (2004); McKee & Walker (2000); Kim & Kwok (1995); Lu, Jin, Cronin-Golomb, Liu, Jiang, Wang, Zhao, Wang & Drehman (1998); Lotspeich, Stephens & Henderson (1982); Von Willisen (1966); Weis & Gaylord (1989); Li, Sullivan & Parsons (1988)). Typical applications include EO modulators and EO tunable filters in telecommunications (Wooten *et al.* (2000); Datta & Das (1990); Tang *et al.* (2004); McKee & Walker (2000)), optical switches and waveguide modulators for high-speed integrated optical devices (Kim & Kwok (1995); Lu *et al.* (1998)), EO tunable filters (Lotspeich *et al.* (1982); Von Willisen (1966)) and MO recording media (Weis & Gaylord (1989); Li *et al.* (1988)) for memory structures. For many of these application devices, the thickness of the active films is normally smaller than or comparable to the wavelength of light. Thus, the optical characterization of thin-film materials can be challenging given their limited interaction range with the electromagnetic (EM) wave propagating through them. In addition, determining all Pockels tensors is complicated because the measurement of their elements' values depends on the relative orientation between the crystal, the applied electric field polarization and the propagation direction of light (Schroder (2006); Hansen (1973)).

There are several methods to overcome these issues and characterize thin-film materials (Hansen (1973); Tompkins & Irene (2005); Kang *et al.* (2008); Teng & Man (1990); Park (2008); Enami, Derose, Mathine, Loychik, Greenlee, Norwood, Kim, Luo, Tian, Jen et al. (2007); Wang, Furman & Haertling (1995); Reitze *et al.* (1993); Hoerman *et al.* (1999); Hunsperger (1995); Rabiei & Gunter (2004); Liu *et al.* (2009); Palmer, Alloatti, Korn, Schindler, Baier, Bolten, Wahlbrink, Waldow, Dinu, Freude et al. (2013); Petraru, Schubert, Schmid, Trithaveesak & Buchal (2003); Lee *et al.* (2011)), and all of them are based on measurements of variations of the material refractive index induced by an applied external field. However, they all have some limitations or restrictions. For example, spectroscopic ellipsometry is a common technique for characterizing the optical properties of thin-films, but one which suffers from rather low sensitivity (Tompkins & Irene (2005); Kang *et al.* (2008)). The Teng-Man reflectometry (Teng & Man (1990)) is a method similar to ellipsometry, but with a significantly better resolution. Although this technique is widely extended for thin-film characterization (Park (2008); Enami *et al.* (2007); Wang *et al.* (1995)), it is still susceptible to misinterpreting the signals measured. The transmission measurement method (Reitze *et al.* (1993); Hoerman *et al.* (1999)) is based on the same principle of detecting changes in polarization, but using transmission geometry with a perpendicular angle of incidence. Unfortunately, this method only determines the effective Pockels value, rather than single tensor elements. The prism coupling method for its part (Hunsperger (1995); Rabiei & Gunter (2004)) provides sensitive measurements by using guided mode waves and applying an electric field between the prism and thin-film (Liu *et al.* (2009)) , but samples must be thick enough to support multiple modes. Alternative methods integrate devices such as Mach-Zehnder interferometers (Palmer *et al.* (2013); Petraru *et al.* (2003)) or resonant structure-like ring resonators (Lee *et al.* (2011) to determine the EO properties of a material included in this structure. While these methods can reveal small Pockels effects (Lee *et al.* (2011)), their design and processing represent an extra workload.

In the last decade, near-field THz imaging methods have emerged as a powerful method for mapping the electric field distribution of metamaterial structures (Seo *et al.* (2007); Bitzer *et al.* (2009)) in a contactless approach, and for resolving the intrinsic resonances of such structures in time and space (Adam (2011); Blanchard *et al.* (2013)). One such method, which is composed of a split ring resonator (SRR), a well-known metamaterial unit cell, is able to excite the electric and magnetic components of the electromagnetic field simultaneously (Padilla, Taylor, Highstrete, Lee & Averitt (2006); Kumar, Strikwerda, Fan, Zhang, Averitt, Planken & Adam (2012)). Technically, the subwavelength resonant responses of SRR can act as tiny electrodes that concurrently probe information in the x-, y-, and z-directions. Therefore, by temporally and spatially resolving the electromagnetic field distribution of an SRR patterned on an unknown thin-film material, one could retrieve the full EO tensors of this material. However, most THz near-field methods work using the raster scanning approach (Seo *et al.* (2007); Bitzer *et al.* (2009); Adam (2011)), and thus require long acquisition times to retrieve relatively large two-dimensional information; such methods would suffer from low sensitivity if thin-film materials were used as EO sensors. More recently, by combining intense THz pulses (Hirori *et al.* (2011)) with a near-field method, extremely thin EO sensors have successfully been used to enable the high-resolution two-dimensional mapping of metamaterial samples (Blanchard & Tanaka (2016)), as well as nonlinear THz near-field imaging (Blanchard *et al.* (2018)).

In this work, we first numerically studied all field distributions of SRRs, including electric and magnetic fields in three dimensions (x, y, z) as a function of the exciting and probing beam polarizations using finite difference time domain (FDTD) simulation. Then, we utilized intense THz near-field microscopy (Blanchard *et al.* (2013); Blanchard & Tanaka (2016); Blanchard *et al.* (2011)) to characterize a 1- μm-thick X-cut Lithium Niobate (LN) crystal as a sensor. Indeed, we used an SRR structure sample similar to the simulated one, and patterned it on an X-cut LN crystal. In agreement with our simulations, we experimentally found the expected response of the readable EO tensors of the LN crystal. Finally, in order to calibrate our method, we used the well-known EO parameters of the LN crystal to analytically show its sensitivity as a function of the applied electric field and optical probe polarizations. This demonstration confirms that our methodology is valuable for characterizing thin-film EO materials.

2.3 Methodology

The EO sampling method, which relies on the linear Pockels effect (Wu & Zhang (1995)), is frequently used for coherently detecting THz radiation. Once a THz electric field is applied to an EO sensor crystal, a modification of its refractive indices appears, depending on the field polarization and its strength. Therefore, changes in the sensor's refractive index will modulate the polarization ellipticity of an optical probe beam passing through the sensor. The induced ellipticity modulation of the optical probe beam can be demodulated using a polarizer, in turn providing information linearly proportional to the applied electric field (Saleh & Teich (1991)).

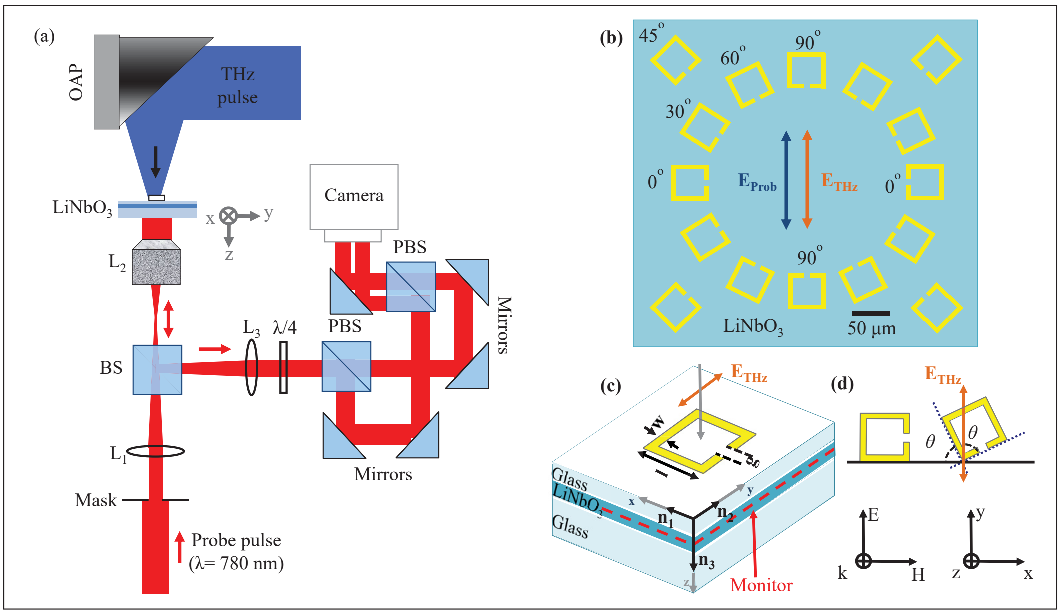

Figure 2.1 Schematic of (a) the experimental setup, where OAP: Off-Axis Parabolic Mirror, PBS: Polarized Beam Splitter and BS: Beam Splitter. (b) Schematic diagram of the SRR pattern arrangement on the surface a of 1-μm-thick LN crystal for the experimental study. (c) Simulation structure of a single SRR unit on LN crystal with a split gap of g = 4 μm, width w = 10 μm and length l = 50 μm and 500-nm-thick gold material. (d) The THz electric field polarization is changed by rotating the SRR structure by the angle θ

Undoubtedly, the most studied EO crystal is lithium niobate, with its high EO coefficient and well-known tensors (Weis & Gaylord (1985); Shuto & Amano (1995)). However, due to the phase mismatching condition between the optical waves (e.g., at 800 nm) and the THz waves (Winnewisser, Jepsen, Schall, Schyja & Helm (1997a)), this crystal is not commonly used for detecting THz waves. Only recently, the two-dimensional (2D) EO near-field method using a thin LN crystal was shown to enable high-resolution THz images (Blanchard & Tanaka (2016)), while being barely sensitive to the phase-matching condition (Blanchard *et al.* (2011)). In this system, to access the near-field region, the sample is placed on top of the EO crystal. The top and bottom surfaces of the EO crystal must have a high-reflection and an anti-reflection coating for the probe light at 780 nm. As shown in Fig. 2.1 (a), the probe light at 780 nm forms an image of the mask on the top surface of the EO crystal after passing through an achromatic lens (L1) in combination with an objective lens (L2). The reflected images are returned to the objective lens and retrieved by a charge-coupled device (CCD) camera with a non-polarized beam splitter cube. To transfer the image to the camera, a second achromatic lens is used (L3). Finally, the measurement of THz-induced birefringence in the EO crystal is detected by a polarization analysis scheme. Since the thickness of the films to be characterized are usually smaller than the wavelength of light, the interaction range with the electromagnetic wave propagating through them is limited. A primary means of compensating for the small EO response is through the use of intense THz pulses (i.e., 500 kV/cm at the focus position) (Hirori *et al.* (2011)).

A significant advantage of performing two-dimensional THz microscopy is that it allows the retrieval of the absolute electromagnetic field distribution on a large field of view (e.g., 500 μm × 500 μm) without changing the experimental condition. To capitalize on this ability, we designed a gold SRR sample arrangement that exhibits distinctive responses as a function of THz field polarizations, which can be simultaneously probed within the same viewing area (see Fig. 2.1 (b)). In order to avoid SRR fabrication difficulty for different material characterizations, the SRRs can also be fabricated on a silicon wafer and then placed on top of the sample EO material to perform a 2D THz microscopy. To fully characterize the expected field distributions of our structure, we carried out 3D simulations using FDTD software from Lumerical. A THz Gaussian beam with a 0.35 ps pulse width and a central frequency of 1 THz was used to excite the SRRs, with its field polarized in the y-direction. All simulation movies cover 17 ps of temporal evolution with 16.8 fs in step resolution. A 500-μm-thick glass substrate, a 1-μm-thick lithium niobate crystal and a 3-μm-thick SiO_2 material for high reflectivity coating were included in the simulated materials, same as the experimental conditions. For our characterization method, we restrict our analysis to the lowest resonant frequency of the SRR, i.e., the LC resonance. The LC resonance is approximately 0.5 THz for the considered dimension of the SRR, also depending on the substrate refractive index. Note that to explore the EO response in a different frequency range, one can change the SRR dimension. In simulations, retrieving all electromagnetic field distributions, E_x, E_y, E_z, H_x, H_y and H_z, in the vicinity of each SRRs, can be done through solving the Maxwell equations. To access the near-field information, a 2D monitor plane is set 5 μm under the SRR position (as shown in Fig. 2.1 (d)), which is in good agreement with the THz microscope used in this study (Blanchard *et al.* (2011)). Experimentally, by using the same structure as the simulated one, but patterned on an unknown EO sensor, the 2D electromagnetic response will only be sensed by the existing EO tensors of the investigated thin-film material (i.e., r_{ijk} EO tensors). Therefore, there is a straightforward relation between the observable experimental response and the related signature from our simulated SRR sample arrangement.

For our demonstration, we analytically studied the uniaxial X-cut LN crystal (also called b-cut), with its ordinary (n_o) and extraordinary (n_e) refractive indices oriented as follows: $n_o = n_1 = n_3$ and $n_e = n_2$, as illustrated in Fig. 2.1 (c). In Fig. 2.1 (d), an applied THz beam (E_{THz}) travels in the z-direction, with its electric and magnetic components pointing toward the ordinary and extraordinary refractive indices, respectively. However, since metamaterial is used to investigate an EO response of thin-film materials, each combination of field polarizations will be available at the same time. In order to simplify our analysis, we defined the principal axes of the THz electric field polarization framework (E_{THz}) in agreement with the principal refractive indices of the crystal, i.e., $E_{THz} = (E_x, E_y, E_z)$. The elements of the impermeability tensor of the crystal are described by Eq. 2.1:

$$\eta_{ij}(\mathbf{E}) = \eta_{ij(0)} + \textstyle\sum_k r_{ijk} E_k \quad , r_{ijk} = \begin{bmatrix} 0 & -r_{22} & r_{13} \\ 0 & r_{22} & r_{13} \\ 0 & 0 & r_{33} \\ 0 & r_{42} & 0 \\ r_{42} & 0 & 0 \\ -r_{22} & 0 & 0 \end{bmatrix}, \qquad ijk = 1,\ 2,\ 3 \quad , \tag{2.1}$$

where $\mathbf{E} = (E_1,\ E_2,\ E_3)$ which is related to $E_{THz} = (E_x,\ E_y,\ E_z)$, where $E_1 = E_z$, $E_2 = E_x$, and $E_3 = E_y$ according to (Winnewisser *et al.* (1997a)) and $r_{ijk,}$ the well-known linear Pockels coefficients of the LN crystal. To find the modified index ellipsoid of the LN crystal, the following equation should be calculated:.

$$\sum_{ij} \eta_{ij}(E)\, x_i x_j = 1 \tag{2.2}$$

Consequently, the EO response can be extracted from the modified index ellipsoid equation, (Saleh & Teich (1991)) as shown in Table 2.1. For an EO sampling measurement, the probe beam $E_{Prob} = (E_x, E_y, E_z)$ undergoes a phase retardation from the modification of the index ellipsoid. It should be mentioned that the intensity of the probe beam is not strong enough to induce the Pockels effect inside the crystal. Thus, E_{Prob} defines the polarization of the probe beam relative to the THz field. The phase retardation is proportional to the difference between the modified ordinary and extraordinary refractive indices, which is a function of the electric field components (E_{THz}) and Pockels coefficients (r_{ijk}). Therefore, the phase retardation, Γ, of the probe beam after propagation in the crystal is given by,(Saleh & Teich (1991)):

$$\Gamma = k_o\left(n_o(\mathbf{E}) - n_e(\mathbf{E})\right)L, \tag{2.3}$$

where k_o is the wavenumber of the probe beam and L is the thin-film thickness. Thus, from this phase retardation function, we can determine the EO response as a function of the THz field polarization, probe polarization and Pockels coefficients of the material. Table 2.1 shows how the sensitivity of the LN crystal depends on the polarization of the applied THz electric field and its EO coefficient by choosing different polarization configurations for the optical probe beam. The first step to characterize a thin material is to know all polarization conditions of the applied electric field and probe beam. Each condition allows determining the specific Pockels coefficients. Table 2.1 presents several conditions. For example: In Table 2.1 (b), the applied THz electric field polarization is in the direction of ordinary refractive index and probe beam polarization is 45^o from ordinary and extraordinary indices of the crystal axis. With this condition, the sensitivity of the LN crystal is 20 pm/V. This shows that the polarization of the THz electric field in this direction only changes the ordinary refractive index of the LN crystal. Therefore, the probe beam experiences the effect of Pockels coefficient r_{22} by considering proper polarization.

Table 2.1 Differential phase retardation as a function of the THz pulse and probe beam polarization directions

Investigation conditions	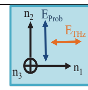	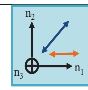	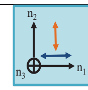	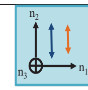
	(a)	(b)	(c)	(d)
THz field ($\mathbf{E_{THz}}$)	$(E_x,\ 0,\ 0)$	$(E_x,\ 0,\ 0)$	$(0,\ E_y,\ 0)$	$(0,\ E_y,\ 0)$
Modified index ellipsoid when, $\mathbf{n_o = n_1 = n_3}$, $\mathbf{n_e = n_2}$	$n_o(E) \approx$ $n_o - \frac{1}{2}n_o^3 r_{22}E$ $n_e(E) \approx n_e$	$n_o(E) \approx$ $n_o - \frac{1}{2}n_o^3 r_{22}E$ $n_e(E) \approx n_e$	$n_o(E) \approx$ $n_o - \frac{1}{2}n_o^3 r_{13}E$ $n_e(E) \approx n_e - \frac{1}{2}n_e^3 r_{33}E$	$n_o(E) \approx$ $n_o - \frac{1}{2}n_o^3 r_{13}E$ $n_e(E) \approx n_e - \frac{1}{2}n_e^3 r_{33}E$
Optical probe beam polarization	$(0,\ E_y,\ 0)$	$(\frac{1}{\sqrt{2}}E_x,\ \frac{1}{\sqrt{2}}E_y,\ 0)$	$(E_x,\ 0,\ 0)$	$(0,\ E_y,\ 0)$
Phase retardation, Γ, (pm/V)	None	$\frac{-1}{2}n_o^3 r_{22} \propto 20$	$\frac{-1}{2}n_o^3 r_{13} \propto 39$	$\frac{1}{2}n_e^3 r_{33} \propto 163$
Investigation conditions	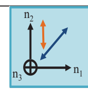	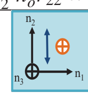	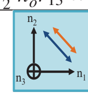	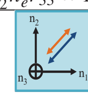
	(e)	(f)	(g)	(h)
THz field ($\mathbf{E_{THz}}$)	$(0,\ E_y,\ 0)$	$(0,\ 0,\ E_z)$	$(\frac{-1}{\sqrt{2}}E_x,\ \frac{1}{\sqrt{2}}E_y,\ 0)$	$(\frac{1}{\sqrt{2}}E_x,\ \frac{1}{\sqrt{2}}E_y,\ 0)$
Modified index ellipsoid when, $\mathbf{n_o = n_1 = n_3}$, $\mathbf{n_e = n_2}$	$n_o(E) \approx$ $n_o - \frac{1}{2}n_e^3 r_{13}E$ $n_e(E) \approx$ $\mathbf{n_e - \frac{1}{2}n_e^3 r_{33} E}$	None	$n_o(E) \approx$ $n_o - \frac{1}{2\sqrt{2}}n_e^3(-r_{22} + r_{13})E$ $n_e(E) \approx$ $n_e - \frac{1}{2\sqrt{2}}n_e^3 r_{33}E$	$n_o(E) \approx$ $n_o - \frac{1}{2\sqrt{2}}n_e^3(r_{22} + r_{13})E$ $n_e(E) \approx$ $n_e - \frac{1}{2\sqrt{2}}n_e^3 r_{33}E$
Optical probe beam polarization	$(\frac{1}{\sqrt{2}}E_x, \frac{1}{\sqrt{2}}E_y, 0)$	$(0,\ E_y,\ 0)$	$(\frac{-1}{\sqrt{2}}E_x, \frac{1}{\sqrt{2}}E_y, 0)$	$(\frac{1}{\sqrt{2}}E_x, \frac{1}{\sqrt{2}}E_y, 0)$
Phase retardation, Γ, (pm/V)	$\frac{-1}{2}\left(n_o^3 r_{13} - n_e^3 r_{33}\right)$ $\propto 125$	None	$\frac{1}{2\sqrt{2}}\left(n_o^3(-r_{22} + r_{13}) - n_e^3 r_{33}\right)$ $\propto 103$	$\frac{1}{2\sqrt{2}}\left(n_o^3(r_{22} + r_{13}) - n_e^3 r_{33}\right)$ $\propto 74$

For X-cut LN crystal, n_o=n_1=n_3=2.29 and n_e=n_2=2.20 at 0.840. Where, r_{22}=3.4 pm/V, r_{13}=6.5 pm/V, r_{33}=30.8 pm/V, at 0.633nm (Blanchard *et al.* (2013))

In condition Table 2.1 (a), the probe beam polarization is not proper to undergo any phase retardation. Therefore, we cannot detect any sensitivity from the LN crystal with the same applied THz electric field polarization.

2.4 Results and discussion

According to Faraday's Law, the electric field vector E and magnetic field vector H of the time-varying electromagnetic wave are linked. Once an incident E_{THz} is applied with its polarization parallel to the SRR arm containing the gap, an asymmetric field distribution induces a current on the metal surface. Within this conductive loop, a magnetic flux appears in the z-direction. This current also leads to an accumulation of charge carriers near the gap area and creates a field enhancement. The enhancement factor depends on the accumulated charge carrier amount in the gap zone, which is finite and a function of the gap size (Bagiante, Enderli, Fabiańska, Sigg & Feurer (2015)). In the near-field range of the SRR gap position, several orders of magnitude in field enhancement are reachable. Such a strong field enhancement is a key point allowing sensitive thin-film material characterization through THz microscopic imaging. The spatial distribution of the different frequencies within the bandwidth of the THz pulse of each electromagnetic field in the frequency domain can be determined from the electromagnetic field response in the time domain by using a Fourier transformation. For example, $E_z(x,\ y,\ \omega)$ can be determined from $E_z(x,\ y,\ t)$. In this section, as a second step of our characterization method, we present all the responses of the designed SRR as shown from Fig. 2.2 to Fig. 2.5.

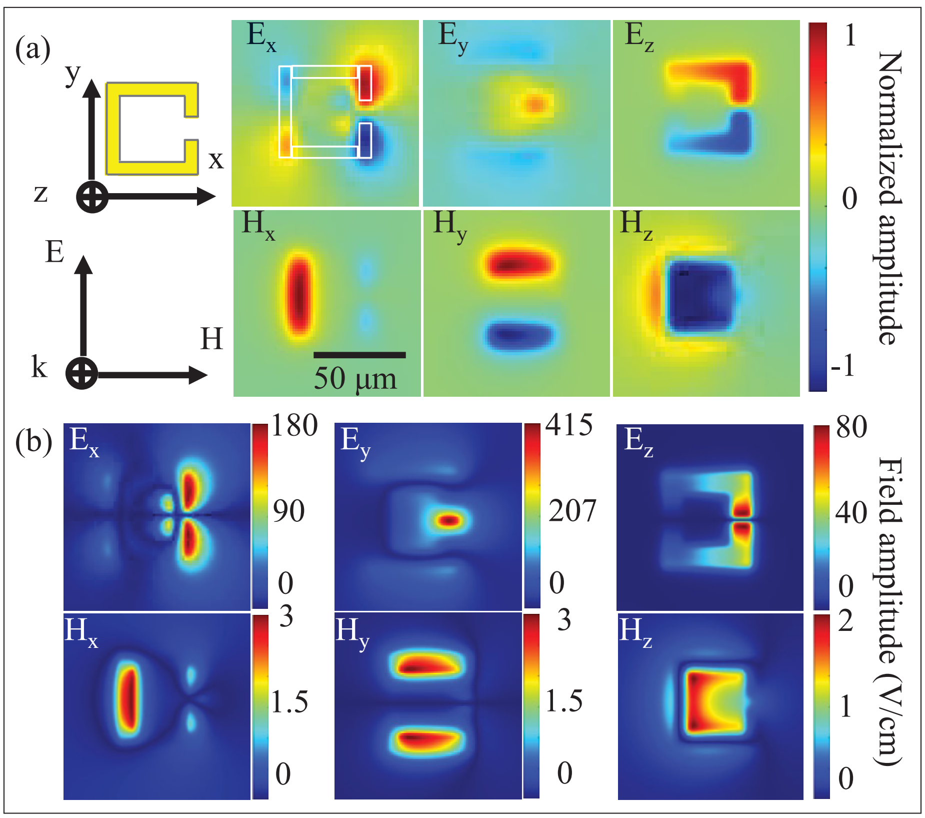

Figure 2.2 Simulated amplitude-frequency maps of the electric and magnetic field components of an SRR at 0.46 THz with the incident THz field polarized in the y-direction. (a) and (b) respectively, show the real and absolute amplitude-frequency maps for (E_x, E_y, E_z) and (H_x, H_y, H_z)

In Fig. 2.2, we explore the Fourier-transformed images of the spatially distributed electric $(E_x,\ E_y,\ E_z)$ and magnetic $(H_x,\ H_y,\ H_z)$ amplitude field maps at 0.46 THz for an SRR excited by a THz field polarized in the y-axis. Fig. 2.2 (a) shows the real part of the normalized electromagnetic field, in which each field is normalized with its maximum response (i.e., excluding contributions from the imaginary part). Fig. 2.2 (b) illustrates the absolute value of each electric and magnetic field components at the LC resonance. Each map shows their maximum local field amplitudes. The incident-simulated field is 10 V/cm and large enhancements are observed for each field direction. Indeed, the local field amplitudes are enhanced relative to incident THz electromagnetic field amplitude. All these fields are simultaneously applied on the thin material. Technically, by sensing an unknown EO thin-film material, a THz microscopy investigation of an SRR should reveal one of the near-field maps presented in Fig. 2.2. As the incident THz field is polarized in the y-direction, the charges accumulate at the gap edge position. This leads to an antisymmetric electric field distribution on the SRR for the E_x and E_z components, while the E_y component remains symmetric. Therefore, the E_y electric field concentrates in the middle of the SRR gap with constant phase, and E_x and E_z appear with a π-phase shift across the gap. These symmetric and antisymmetric electric field distributions can be attributed to the symmetry of the SRR, in addition to the symmetry of the incident electric field. The E_z electric field component shows the charge density on the surface of the SRR. The E_y electric field presents the electric field enhancement in the gap with a high intensity, while the intensity of the E_z component is close to one order of magnitude lower as compared to the E_y and E_x components, as shown in Fig. 2.2 (b).

To improve our understanding of the near-field distribution of the SRR, Fig. 2.3 reports the polarization dependence response of the SRR, resulting in confirming the crystal axis orientation. To have a comprehensive idea of the coupling efficiency as a function of polarization, all electric field amplitudes are normalized, with the maximum amplitude electric field found for SRR with $\theta = 0°$. Figs. 2.3 (a) and (b) respectively represent the angular dependency of the real and absolute values of the near-field electric component in the x-direction (E_x), i.e., perpendicular to the incident THz field. These two-dimensional normalized maps can be translated as the electric charge density just outside the SRR surface in the x-direction at 0.46 THz. Figs. 2.3 (c) and (d) respectively show the real and absolute amplitudes of the electric field (E_y) enhancement appearing in the gap of the SRR, with the highest intensity for $\theta = 0°$.

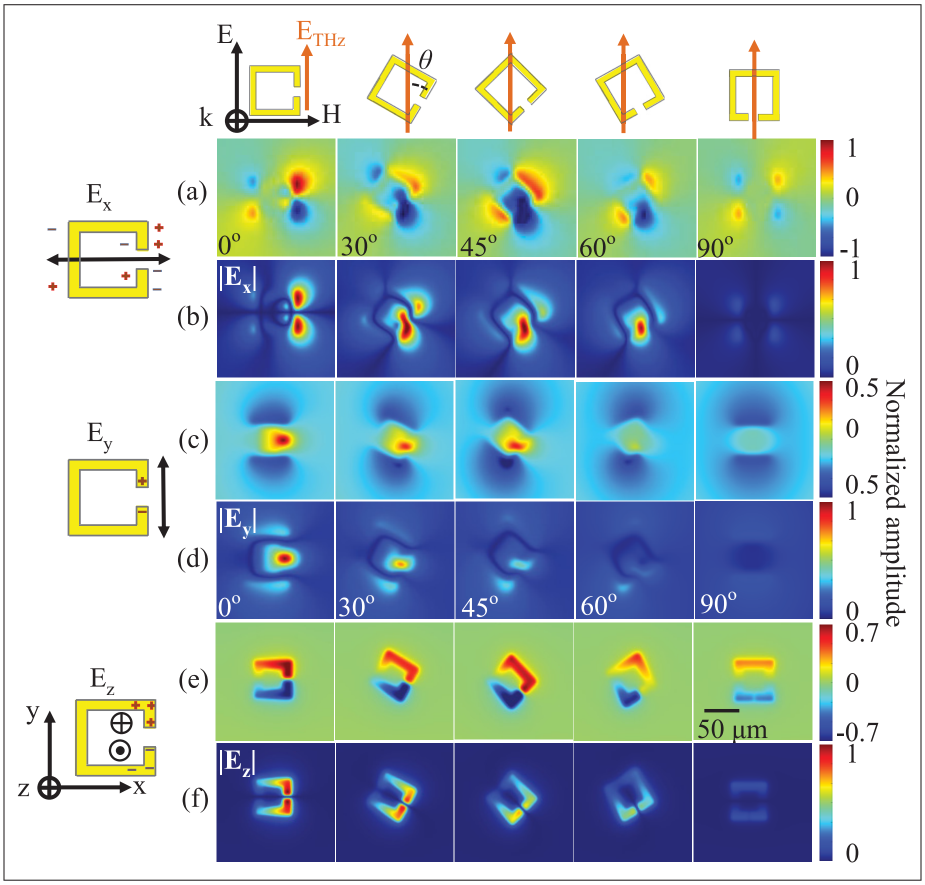

Figure 2.3 Normalized amplitude electric field maps from the SRR response at 0.46 THz and as a function of THz field polarization. (a), (c) and (e) are the real amplitudes of E_x, E_y and E_z components as functions of the incident THz field, respectively. (b), (d) and (f) are the absolute amplitudes of E_x, E_y and E_z components as functions of the incident THz field, respectively

The field enhancement is gradually reduced until vanishing at $\theta = 90°$. In this case, no asymmetric field distribution exists and the current becomes null. Figs. 2.3 (e) and (f) show the corresponding two-dimensional maps of the real and absolute amplitudes of the E_z components. The field in the z-direction shows the amount of charge density on the surface of the SRR, and is proportional to the charge distribution around the SRR. As the near-field electric component in the z-direction (E_z) is perpendicular to the SRR metal surface, it shows how light emerges from the SRR surface. In addition, the spatial distribution of the surface charge density occurs in the vicinity of the gap of the SRR (Bagiante *et al.* (2015); Adam *et al.* (2008)) and undergoes a π-phase shift across the gap. To visualize this effect in the time domain, Fig. 2.4 (a) shows the simulated time-dependent out-of-plane electric field $E_z(t)$ at two points close to the gap of the SRR (i.e., p1 and p2). The different snapshots of the $E_z(x, y, t)$ field distribution at different times is shown in Fig. 2.4 (b). The time stamps in the x-axis of Fig.2.4 (b) are selected based on the time corresponding to peak amplitudes in Fig.2.4 (a), as illustrated by t_1 to t_8. It can clearly be observed that the field is changing signs right at the edge of the gap due to the π-phase shift.

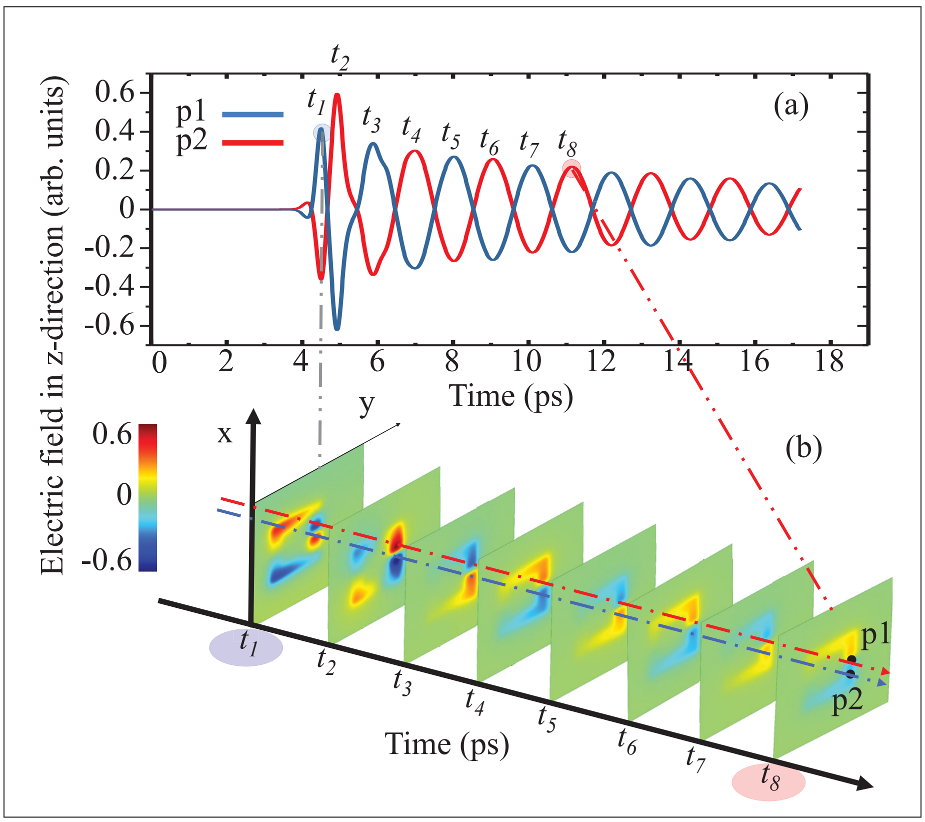

Figure 2.4 Simulated time-dependent out-of-plane electric field for the SRR with a 4 μm wide gap. The time-dependent electric field measured at two points of p1 and p2 close to the gap of SRR structure is shown in (a). The intensity graphs show the time-dependent electric field distribution $E_z(x,\ y,\ t)$ at a selected time (b)

As the time-varying optical electromagnetic wave is described by Faraday's Law, the near-field distribution in the vicinity of the SRR structure also has a magnetic excitation in the x-, y- and z-directions. It means that coupling the incident electric field to the SRR structure and producing a current in the loop causes a magnetic field to appear. It is well known that the amplitude of the magnetic field is strongest at the first resonant frequency of the SRR. From Faraday's Law, we have:

$$H = -\frac{i}{\omega\,\mu_0}\frac{\partial B}{\partial t} = \frac{i}{\omega\,\mu_0}\nabla \times E, \tag{2.4}$$

where $B = \mu_0 H$ and the time derivative of a time-harmonic wave can be represented by $i\omega$, where ω is the frequency of the wave. For example, the near-field magnetic component in the x-direction, as shown in Fig. 2.5 (a), simplifies the numerical curl operation from Eq. 2.4 to:

$$H_x = \frac{i}{\omega\,\mu_0}\left(\frac{\partial E_z}{\partial y} - \frac{\partial E_y}{\partial z}\right) \tag{2.5}$$

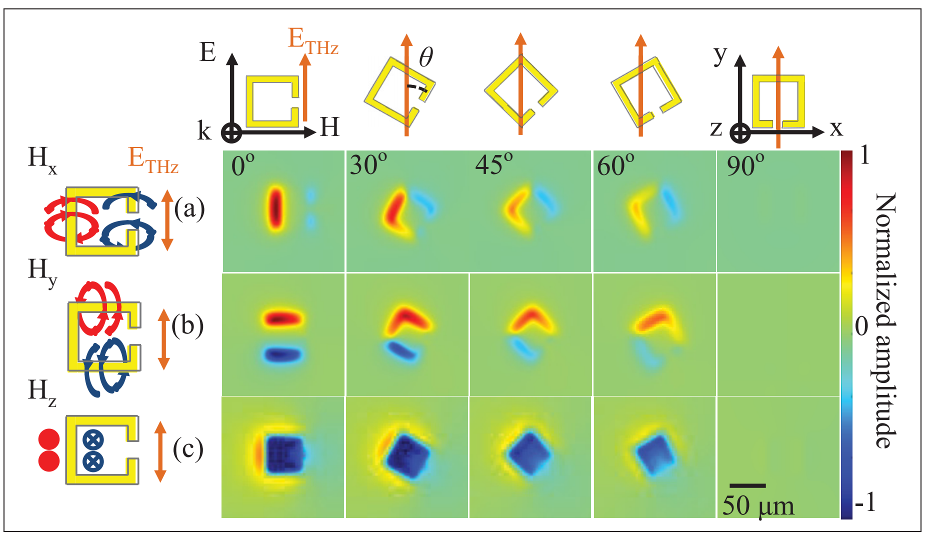

Figure 2.5 Normalized amplitude of the magnetic field mapped at the lowest resonant frequency, i.e., 0.46 THz. (a), (b) and (c) are the real amplitudes of H_x, H_y and H_z components as functions of the incident THz field, respectively

The current orientation in the conductive material is proportional to the applied electric field orientation and based on Ohm's law, a magnetic field is perpendicular to the current direction

(Olmon, Rang, Krenz, Lail, Saraf, Boreman & Raschke (2010)). Therefore, H_x provides the contribution of the electric field component in the y- and z-directions, as shown in Fig. 2.5 (a). The charge separation generated from the electric field over the x-direction creates a current that gives rise to a magnetic dipole in the y-direction (H_y), in response to the driving incident THz electric field. With our simulated monitor placed 5 μm under the SRR (inside the thin-film material), only the currents perpendicular to the SRR arm can be observed, as shown in Fig. 2.5 (b). Fig. 2.5 (c) shows the two-dimensional spatial distribution of the near-field Hz of the SRR at the lowest resonance frequency, with different polarizations of E_{THz}. As H_z is perpendicular to the surface of the SRR, it provides information on the spatial distribution of the magnetic field going inside and outside the SRR. We observe that the magnetic field is strongest near the bridge region that connects the two voids, where the current has the maximum value.

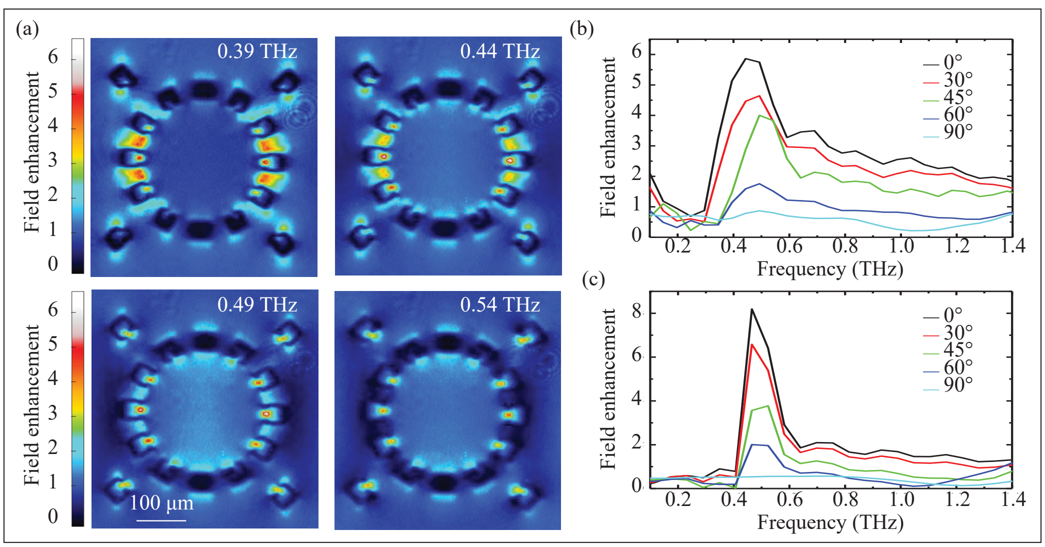

Figure 2.6 Illustration of (a) normalized absolute amplitude of experimental electric field obtained on the structure illustrated in Fig. 2.1 (a) as a function of angle mapping of the SRR at the LC resonance frequency, i.e., 0.39, 0.44, 49, and 54 THz. (b) and (c) are respectively the experimental and simulated results of the absolute values of the electric field enhancement, E_y, in the gap of SRR

In the last step, in order to confirm and calibrate our proposed method, we experimentally characterize a 1-μm-thick LN crystal by performing a 2D near-field THz imaging, whose experimental details are described in (Blanchard *et al.* (2013); Blanchard & Tanaka (2016); Blanchard *et al.* (2011)). The SRRs arrangement on the LN sample is shown in Fig. 2.1 (b) for experimental characterization. For the sensing demonstration, the condition (d) from Table 2.1 is considered, where the THz and probe polarization are set parallel to each other and aligned with the extraordinary index axis of the crystal. This condition exhibits the strongest EO response Γ of 163 pm/V, as predicted by Table 2.1 (d). In this condition, the probe beam experiences the phase retardation due to Pockels coefficient r_{33}. In Fig. 2.6 (a), we show the absolute value of the 2D electric field maps for 0.39, 0.44, 0.49 and 0.54 THz, normalized to the reference signal (i.e., without the SRR structure) in the LN crystal. This normalization procedure directly produces a 2D field enhancement mapping of the resonant response. The reference and signal THz movies cover 10 ps of temporal evolution with 40 fs in step resolution. In order to smooth their spectral response, 10 ps of padding data were added to both movies. Still, the spectral resolution of our experimental measurements is limited to 100 GHz line width.

Through a simple observation, it can be seen that the polarization dependency clearly corresponds to the E_y response from the SRR structure (see the simulated response in Fig. 2.3 (d)). The maximum field enhancement at the gap position is observed at 0.49 THz, in good agreement with our simulations. Conversely, no field enhancement exists for the 90° SRR structure, as expected. A gradually decreasing field enhancement behavior is observed for the other SRR structures (i.e., at 30°, 45°, and 60°). To confirm that this visual observation is representative of the E_y response, we extracted the absolute field enhancement value measured at the gap position of each SRR (Fig. 2.6 (b)) and compared them with the corresponding simulated values of E_y (Fig. 2.6 (c)). The comparison shows that the simulated absolute field enhancement E_y at the gap position of the SRR is in good agreement with the experimental response from the LN thin-film. Still, some differences exist between the experimental and simulation results, and they may arise due to the low spectral resolution of our system. This would be critical in the case of high Q-factor resonators, where misleading measurements of the resonance responses could occur.

Table 2.2 Differential phase retardation for a probe beam polarized in Y-direction as a function of THz pulse polarizations for (a) 0°, (b) 30°, (c) 45°, and (d) 60° angles

Investigation conditions	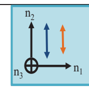	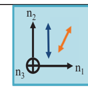	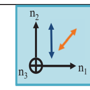	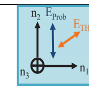
	(a)	(b)	(c)	(d)
THz field (E_{THz})	$(0,\ E_y,\ 0)$	$(\frac{1}{2}E_x,\ \frac{\sqrt{3}}{2}E_y,\ 0)$	$(\frac{1}{\sqrt{2}}E_x,\ \frac{1}{\sqrt{2}}E_y,\ 0)$	$(\frac{\sqrt{3}}{2}E_x,\ \frac{1}{2}E_y,\ 0)$
Modified index ellipsoid when, **$n_o = n_1 = n_3$,** **$n_e = n_2$**	$n_o(E) \approx$ $n_o - \frac{1}{2}n_o^3 r_{13} E$ $n_e(E) \approx n_e - \frac{1}{2}n_e^3 r_{33} E$	$n_o(E) \approx$ $n_o - \frac{1}{4}n_o^3(r_{22}+r_{13})E$ $n_e(E) \approx n_e - \frac{\sqrt{3}}{4}n_e^3 r_{33} E$	$n_o(E) \approx$ $n_o - \frac{1}{2\sqrt{2}}n_o^3(r_{22}+r_{13})E$ $n_e(E) \approx n_e - \frac{1}{2\sqrt{2}}n_e^3 r_{33} E$	$n_o(E) \approx$ $n_o - \frac{\sqrt{3}}{4}n_o^3(r_{22}+r_{13})E$ $n_e(E) \approx n_e - \frac{1}{4}n_e^3 r_{33} E$
Optical probe beam polarization	$(0,\ E_y,\ 0)$	$(0,\ E_y,\ 0)$	$(0,\ E_y,\ 0)$	$(0,\ E_y,\ 0)$
Phase retardation, Γ, (pm/V)	$\frac{1}{2}n_e^3 r_{33} \propto 163$	$\frac{\sqrt{3}}{4}n_e^3 r_{33} \propto 142$	$\frac{1}{2\sqrt{2}}n_e^3 r_{33} \propto 116$	$\frac{1}{4}n_e^3 r_{33} \propto 82$

To better understand our EO characterization method and its limitation, we have compared the experimental measurements with the predicted response from our structure. For that purpose, at least two factors must be taken into account; the EO response in the appropriated crystal direction and the coupling efficiency of each SRR. In other words, the THz beam coupled to the SRR gap is a function of the SRR angle and the EO response of the LN crystal, which also depends on the field direction. The EO response of LN crystal as a function of the SRR angle for 0°, 30°, 45° and 60° are reported in Table 2.2. Similarly as in experiment, the probe beam is kept parallel to the extraordinary crystal axis. The analytical study shows the LN response dependency on the polarization of THz beam gradually reducing from 163 to 82 pm/V, as expected for the SRR oriented from 0° to 60°, respectively. On the other hand, the efficiency of the incident THz beam E_y coupled with the SRR can be estimated by this simple relation (Staelin (2011)), $E_{coupled} \approx E_y cos(\theta)$, where θ is the SRR orientation angle with respect to the THz beam. Additionally, the projection of the field enhancement response at the gap position E_{gap}, which is read by a probe beam aligned in the E_y direction, must follow a $cos(\theta)$ relationship. Thus, this combined relation can approximate the simulation response:

$$E_{gap} \approx E_y\, (cos\,(\theta))^2 \tag{2.6}$$

In the second column of Table 2.3, the response of Eq. 2.6 as a function of the SRR angle is reported. By normalizing the simulated response of the SRR (i.e., from Fig. 2.6 (c)) to its maximum response for the SRR at 0°, a clear agreement with Eq. 2.6 is found in column

3. Since the simulation does not take into account the EO coefficient of the LN crystal, the expected experimental response has to be weighted using the coefficient obtained in Table 2.2. It is interesting to note that when the probe beam is aligned to the extraordinary axis, only r_{33} parameter appear in the response (as in Table 2.2), For that condition, the sensitivity dependency found in column 5 of Table 2.3 exactly follows the one reported in simulation (i.e. in column 3).

Table 2.3 Ratios between the different Pockels coefficients considering the different couplings of the THz beam on the SRR gap

SRR angle θ	**Response in E_y direction** $\sim$ **Ey(cos(θ)^2**	**Simulation measurements E_y (0.46 THz)**	**EO coefficient Γ(pm/V)**	**Expected weighted response**	**Experiment results E_y (0.44 THz)**	**Experiment results E_y (0.49 THz)**
0	1	1	163	1	1 ± 3.7%	1 ± 3.6%
30	0.75	0.78	142	0.75	0.72 ± 3.8%	0.77 ± 3.0%
45	0.50	0.49	116	0.50	0.41 ± 7.2%	0.64 ± 3.2%
60	0.25	0.25	82	0.25	0.16 ± 7.5%	0.18 ± 4.0%
90	0	none	none	none	none	none

Finally, to evaluate the repeatability of our measurements, we extract all field enhancement data at the gap position of every SRR structure. All the corresponding structures are averaged together. As shown in Fig. 2.1 (b), we have two SRRs structures for 0°, four at 30°, four at 45°, four at 60°, and two at 90°. Using these data, a standard deviation of the measurements for each SRR angle is extracted. The last two columns of Table 2.3 show the normalized absolute field values of each SRR with their corresponding standard deviations. Due to a higher signal-to-noise ratio (SNR), the strongest field responses show better standard deviations than the weaker field enhancement values (e.g., SRR at 60°). It means that, the range of field responses as a function of angle dependency agrees well with the expected measurements. The most problematic SRR behavior is seen at 45°. We suspect that the Q-factor of this resonator is slightly higher than other SRRs in this sample arrangement. This might be due to the absence of a mutual coupling between adjacent SRR structures. It can be seen in Fig. 6(a) that SRR 0°, 30° and 60° are mutually coupled at 0.39 THz (i.e., by the strong fields between them). This situation does not exist with the SRR at 45° and may sharpen its resonance (see also the experimental time-domain movie of signal - reference in supplementary info S1). In fact, this reason and the low spectral resolution may explain the small discrepancy between our measurements and the expected response reported in Table 2.3. Nevertheless, we believe that this demonstration remains an important tool for EO characterization, particularly when it comes to rapidly evaluating the field direction responses of novel thin EO materials. We can use the data presented here as a reference tool to characterize novel EO thin materials. As an essential step, if the tensor structure is not known, the X-ray method could be performed (Weis & Gaylord (1985)). Based on this tensor structure, the next step would consist in exploring the spatially resolved EO responses for various probe beam polarization conditions. It is worth mentioning that for some EO coefficients, it would be mandatory to evaluate additional crystal cuts (e.g., a z-cut LN crystal is needed to retrieve the r_{42} coefficient). Therefore, the same evaluation as in Table 2.1 could be used to extract the obtained spatial signature from our special SRR design. In principle, a correlation between LN material response and an unknown material response could lead to an absolute EO calibration method. As an example for the current experimental condition, the modulation values read by our microscope system (i.e. from the balanced imaging scheme) could be used to estimate the THz field at the gap position of each SRR. This operation is commonly done for field evaluation of THz sources (Blanchard *et al.* (2007)):

$$Modulation \approx \frac{2\pi}{\lambda} n_e^3 r_{33} E_{THz} L \tag{2.7}$$

with L the thin-film thickness, r_{33} a known EO coefficient of LN crystal and λ the probing beam wavelength. For an unknown thin-film EO material, the rest of the solution becomes a reverse problem. Hence, knowing the expected THz field values for each SRR, one could measure the modulation and fit its response with the sought EO values.

2.5 Conclusion

We introduced a new method to characterize the optical properties of EO thin-film materials using the THz near-field imaging technique. In agreement with our simulations, we experimentally found the expected responses of the readable EO tensors of an X-cut LN crystal. As the EO parameter of the LN crystal was known, we analytically showed its sensitivity as a function of the applied electric field and optical probe polarizations. This demonstration confirmed the responses of the LN crystal. Indeed, the analytical results showed how to find all elements of the EO coefficient tensor from X-cut LN crystal as a function of THz pulse and probe beam polarization. Therefore, using the setup presented here, we should be able to characterize an unknown material with the same SRR structure that is patterned on it. In other words, we should be able to retrieve the EO components of the unknown material according to our previous LN characterization by this method. Ultimately, since the SRR structure also exhibits a magnetic response, this method could be extended to characterize novel magneto-optic materials.

2.6 Acknowledgment

F.B. gratefully acknowledges financial support from NSERC grant number RGPIN-2016-05020, the FRQNT and the ÉTS Chair in THz optoelectronics.

CHAPTER 3

ACTIVE TERAHERTZ TIME DIFFERENTIATOR USING PIEZOELECTRIC MICROMACHINED ULTRASONIC TRANSDUCER ARRAY

Fatemeh Amirkhan[1] , Alexandre Robichaud[1] , Xavier Ropagnol[1,2] , Mathieu Gratuze[1] , Tsuneyuki Ozaki[2] , Frederic Nabki[1] , François Blanchard[1]*

[1] Department of Electrical Engineering, École de technologie supérieure, 1100 Notre-Dame West, Montreal, Quebec, Canada H3C1K3
[2] Institut national de la recherche scientifique, Varennes, Quebec, Canada J3X 1P7

Paper published in Journal of the Optics Letter (OL), July 1, 2020.

Résumé

La croissance rapide des technologies de l'information est étroitement liée à notre capacité à moduler et démoduler un signal, que ce soit dans le domaine des fréquences ou dans celui du temps. Des démonstrations récentes de modulation térahertz (THz) font appel à des surfaces métamatérielles semi-conductrices actives ou utilisent un micromiroir à réseau pour le réglage du décalage de fréquence. Cependant, un différentiateur actif et à large bande dans la bande de fréquence THz reste à démontrer. Nous proposons ici une méthode simple pour différencier une impulsion THz en induisant de minuscules changements de phase sur le trajet du faisceau THz à l'aide d'un réseau de transducteurs ultrasoniques micro-usinés piézoélectriques. Nous démontrons précisément que le signal THz modulé détecté après le dispositif piézoélectrique est proportionnel à la dérivée de premier ordre de l'impulsion THz. La technique proposée pourra prendre en charge une large gamme d'applications THz, telles que les schémas de détection de crête pour les systèmes de télécommunication.

3.1 Abstract

The rapid growth of information technology is closely linked to our ability to modulate and demodulate a signal, whether in the frequency or in the time domain. Recent demonstrations of terahertz (THz) modulation involve active semiconductor metamaterial surfaces or the use of a grating-based micromirror for frequency offset tuning. However, a wideband and active differentiator in the THz frequency band is yet to be demonstrated. Here, we propose a simple method to differentiate a THz pulse by inducing tiny phase changes on the THz beam path using a piezoelectric micromachined ultrasonic transducer array. We precisely demonstrate that the modulated THz signal detected after the piezoelectric device is proportional to the first-order derivative of the THz pulse. The proposed technique will be able to support a wide range of THz applications, such as peak detection schemes for telecommunication systems.

3.2 Introduction

Modulators are the key to success in advancing information technology in terms of speed and efficiency (Yu, Wu, Wang, Guo & Tong (2017); Cai, Qin, Cui, Li & McCann (2018b); Ma *et al.* (2019)). Undeniably, in the context of the ever-increasing demand for telecommunications bandwidth (Gubbi, Buyya, Marusic & Palaniswami (2013); Al-Fuqaha, Guizani, Mohammadi, Aledhari & Ayyash (2015)), research activities focused on designing and implementing new and efficient modulators are not about to slow down. For optical communications, the last decade has witnessed the achievement of critical modulation functions to overcome the severe speed limitations imposed by an electronics-based system (Salem *et al.* (2013)). In particular, optical differentiator schemes that perform the time derivative of the field envelope of an optical signal are mandatory in processing ultrahigh-bit-rate optical communication signals (Slavík *et al.* (2006); Azaña (2010)). In the near-infrared range (NIR), this operation is generally done using various schemes, such as fiber grating, temporal lensing, and electro-optic effects (Salem *et al.* (2013); Slavík *et al.* (2006); Azaña (2010)). At the same time, the spatial differentiation function is a common operation in digital image processing for edge detection (Gonzalez & Woods (2002)). For example, this operation can be achieved optically using plasmonic response at the metal-dielectric interface (Zhu, Zhou, Lou, Ye, Qiu, Ruan & Fan (2017)), as well as by guided resonances in photonic crystal slabs (Guo, Xiao, Minkov, Shi & Fan (2018)). Although many of these approaches are well established in the manipulation of the optical beam, they still remain to be demonstrated in the THz frequency band (i.e., from 0.1 THz to 10 THz). The arrival of THz waves in the telecommunications world is eagerly awaited (Nagatsuma, Ducournau & Renaud (2016); Ma, Shrestha, Adelberg, Yeh, Hossain, Knightly, Jornet & Mittleman (2018)). Consequently, the demand for a differentiation device to identify the high-frequency component of a signal, such as peak detection, will be a necessary tool to respond to future real-time, high-speed information processing. Significant efforts have been investigated in achieving the analog modulation of THz waves (Ma *et al.* (2019); Kappa, Sokoluk, Klingel, Shemelya, Oesterschulze & Rahm (2019); Wang, Zhang, Guo, Chen, Liang, Hao, Hou, Kou, Zhao, Zhou et al. (2019b); Cai, Huang, Hu, Liu, Fu, Zhao, He & Lu (2018a); Zhang, Chen, Liu, Zhang, Zhao, Dai, Bai, Wan, Cheng & Castaldi (2018a); Vasić, Zografopoulos, Isić, Beccherelli & Gajić (2017); Filin *et al.* (2001); Jiang *et al.* (2000a); Fang, Lou & Ruan (2017)). For example, micromirror array grating-based (Kappa *et al.* (2019)) and THz metasurfaces (Wang *et al.* (2019b)), which are based on various functional materials, such as photoexcited semiconductors, liquid crystal and graphene, have provided several modulation types: frequency tuning (Kappa *et al.* (2019)), amplitude modulator (Cai *et al.* (2018a)), phase modulator (Zhang, Zhao, Liang, Zhang, Wang, Zhou, Kou, Lan, Zeng & Han (2018b)), and polarization control (Vasić *et al.* (2017)). Although a few attempts have been made to introduce temporal (Filin *et al.* (2001); Jiang *et al.* (2000a)) and spatial (Fang *et al.* (2017)) differentiators, to the best of our knowledge, none of them work dynamically in the time and/or space domain, i.e., with an external control signal, which is required to efficiently couple information from an electronic signal to THz radiation. In this letter, we propose a differentiator using an 8×8 piezoelectric micromachined ultrasonic transducers (PMUT) array excited at its resonant frequency to realize a first-order temporal differentiation in the THz region. The PMUT array is generally used for ultrasonic transducers (Robichaud *et al.* (2018b)). Here, each unit cell acts as a single micromirror to modulate the full THz bandwidth in the time domain. The piezo resonance is excited by an external single-frequency electric field, which induces an up and down translation of each unit cell, allowing tiny temporal (i.e., at the femtosecond timescale) variations in the THz beam path. Using a lock-in detection referenced on the piezo resonance frequency allows undertaking a differential measurement. Here, we first describe the characteristics and functionality of the PMUT. Then, we demonstrate that the lock-in detection of THz pulses at the PMUT's resonant frequency is proportional to the first-order derivative of the reflected THz pulse. Third, we evaluate the effect of PMUT amplitude motion on the derivative signal behavior. Based on these observations, we recommend the limit at which microelectromechanical devices can act as differentiators for THz waves.

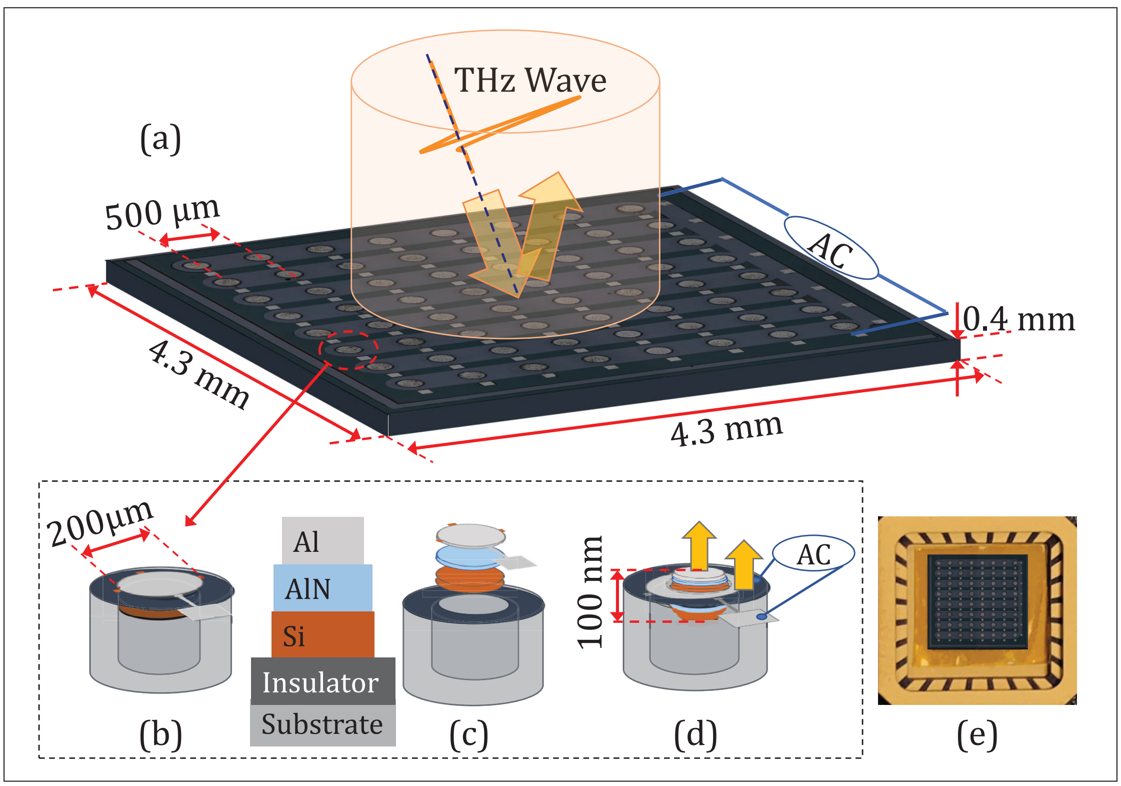

Figure 3.1 Picture of the fabricated PMUT array on an SOI wafer with the illustration of (b) unit cell, (c) materials, (d) functionality when a driving voltage is applied, and (e) the picture of the array mounted on a gold leadless chip carrier (LCC) package Adapted from Robichaud *et al.* (2018b)

3.3 PMUT Array Structure

Figure. 3.1(a) shows the PMUT array. The fabrication process is similar to the one described in reference (Robichaud *et al.* (2018b)). The PMUT array covers an area of $4.3 \times 4.3\ \mu m^2$ on a 0.4 mm thick silicon-on-insulator (SOI) wafer substrate. The array is built with 8×8 PMUTs with a 500 μm lattice pitch in both directions. A unit cell of the PMUT array (Figure.3.1 (b)) consists of a silicon membrane structure that is suspended above a trench etched into the substrate. The membrane has a 200 μm diameter, with a 500 nm thick piezoelectric layer (aluminum nitride) sandwiched between the membrane and a top electrode layer to drive the structure electrically. The top electrode is composed of a 1 μm thick aluminum layer and the silicon membrane is 10 μm thick, as shown in Figure.3.1 (c). The structure is suspended above a cylindrical cavity to allow up and down displacement, as illustrated in Figure. 3.1 (d). Due to the geometry and materials of each element, all PMUT unit cells have almost identical resonant frequencies, with their first and second resonant modes located at 1.38 MHz and 5 MHz, respectively. By applying an external sinusoidal electric field at 1.38 MHz, only the first resonant mode of the piezo material is excited, and yields an oscillation in the piezo structure. As illustrated in Figure. 3.1 (d), the maximum achieved displacement normal to the substrate plane is around ± 500 nm, for a total round trip of 100 nm. It should be mentioned that this magnitude of displacement is not high enough to induce a significant curvature on the aluminum surface during the resonant motion at 1.38 MHz, and thus a flat surface.

3.4 Methodology

To test the capacity of the PMUT array to modulate THz signals, we used a standard time-domain THz spectrometer with photoconductive antennas (PCA) (Jepsen *et al.* (2011)). Figures 3.2 (a) and (b) show the experimental configuration without and with modulation applied to the PMUT array, respectively. An ultrafast Ti:Sapphire oscillator laser at an 80 MHz repetition rate with a central wavelength at 805 nm and a pulse duration of 30 fs was used to pump two LT-GaAs PCAs (from Teravil Ltd.) for the emission and detection of THz waves. The average pumping power is set to 25 mW and 20 mW for the emitter and detector, respectively.

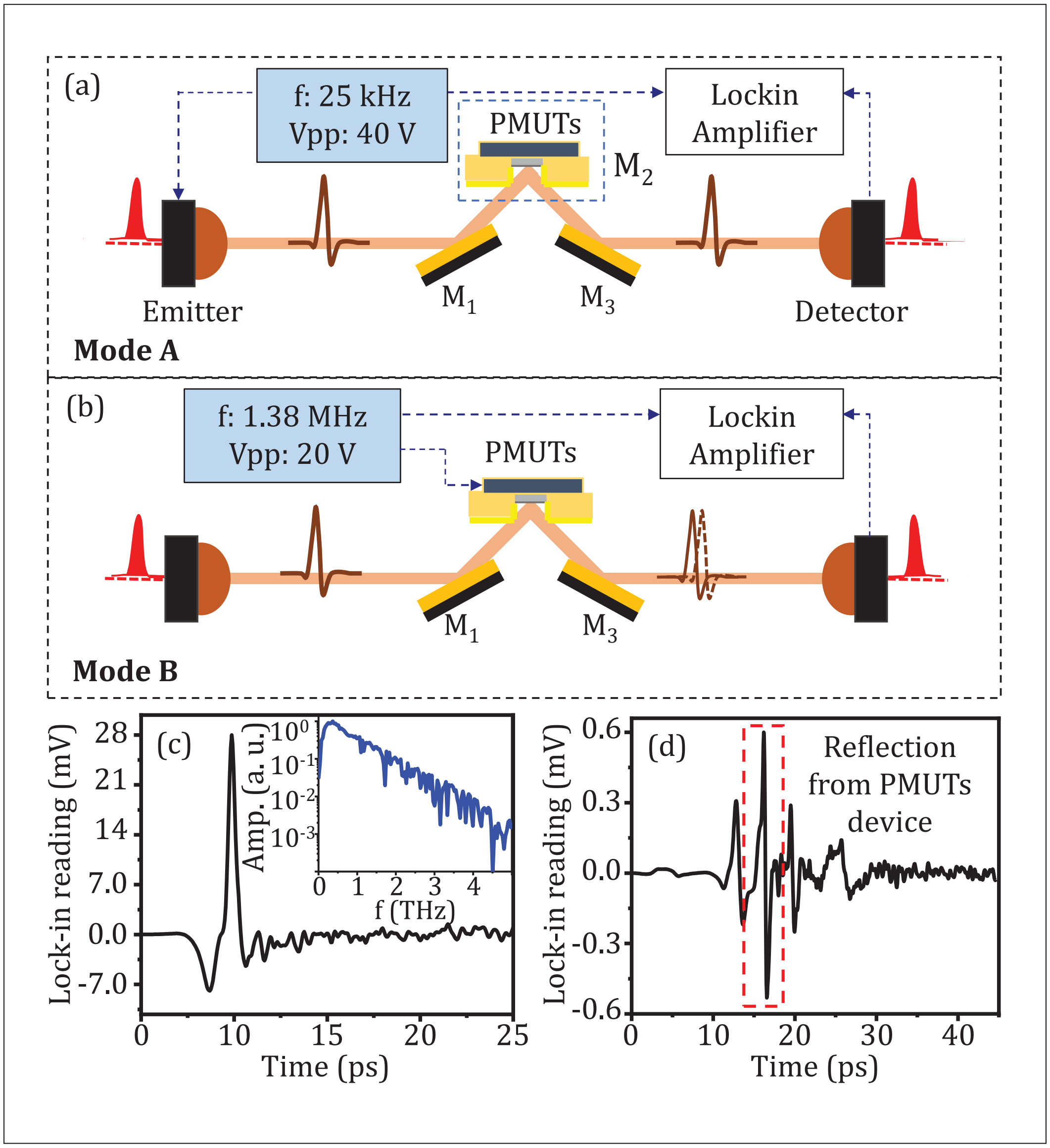

Figure 3.2 Illustration of (a) and (b): experimental device classified into two modes (Mode A and Mode B) using an electronic chopper on the transmitter and a signal generator on the PMUTs, respectively. (c) and (d) show the measured THz wave in Mode A for mirrors only, and the PMUT array replacing M_2, respectively

The hemispherical Si lens on the back of the emitter and detector provides a collimated THz beam approximately 12 mm in diameter. Therefore, to simplify this demonstration, no focusing optics were used; rather, only 2-inch diameter copper mirrors with bare gold coatings on top, denoted M in Figure 3.2 (a) and (b), were used. To work in reflection geometry, the PMUT array is placed in position M_2. Figures 3.2 (c) and (d) show the THz traces obtained with the experimental configuration Mode A, as illustrated in Figure 3.2 (a). For these measurements, the lock-in detection is referenced to the emitter modulation frequency, which was set to 25 kHz. Figure 3.2 (c) shows the THz pulse after the reflection from only highly reflective copper mirrors. In this case, the Fast Fourier Transform (FFT) spectra reveal a bandwidth of 0 to 4 THz and a reading of the lock-in amplifier voltage in the millivolt range. As observed in Figure 3.2 (d), the THz pulse reflected from the PMUT array exhibits a complex shape when compared to the reflection from the flat surface of M_2. This phenomenon is explained by the spatial property of the THz beam impinging on the sample, which is collimated, and thus has a beam size larger than the PMUT array. In this and other such cases, the strongest pulse in Figure 3.2 (d), highlighted by the red dotted line, corresponds to that from the PMUT array, whereas the smaller pulses that appear temporally before and after the main signal originates from multiple reflections coming from the LCC package.

To study the differentiator function of the PMUT array on the THz wave, in active mode, we changed the reference signal sent to the lock-in amplifier by the fundamental resonance frequency of the piezoelectric material. This operation is illustrated in Figure 3.2 (b), and is hereinafter referred to as Mode B. Before investigating the effect of the PMUT motion on the THz beam, we characterized the PMUT frequency response by measuring the transmitted radio frequency (RF) energy (power) using a network analyzer (E5061B Keysight VNA). To identify the resonant frequency, the power transferred (i.e., measured via the S21 scattering parameter) between both electrodes was measured (Robichaud *et al.* (2018b)). In figure 3.3 (a), we show the characteristic response of all PMUT arrays as a function of frequency. From that figure, the PMUTs sharply resonate at 1.386 MHz, and can therefore only be excited optimally at a single frequency of 1.38 MHz. Since each PMUT operates in the MHz frequency range, a high-frequency lock-in amplifier (model SRR844 from Stanford Research System) was required to perform the lock-in detection with the reference signal at 1.38 MHz in order to investigate the effect of PMUT motions on THz radiation.

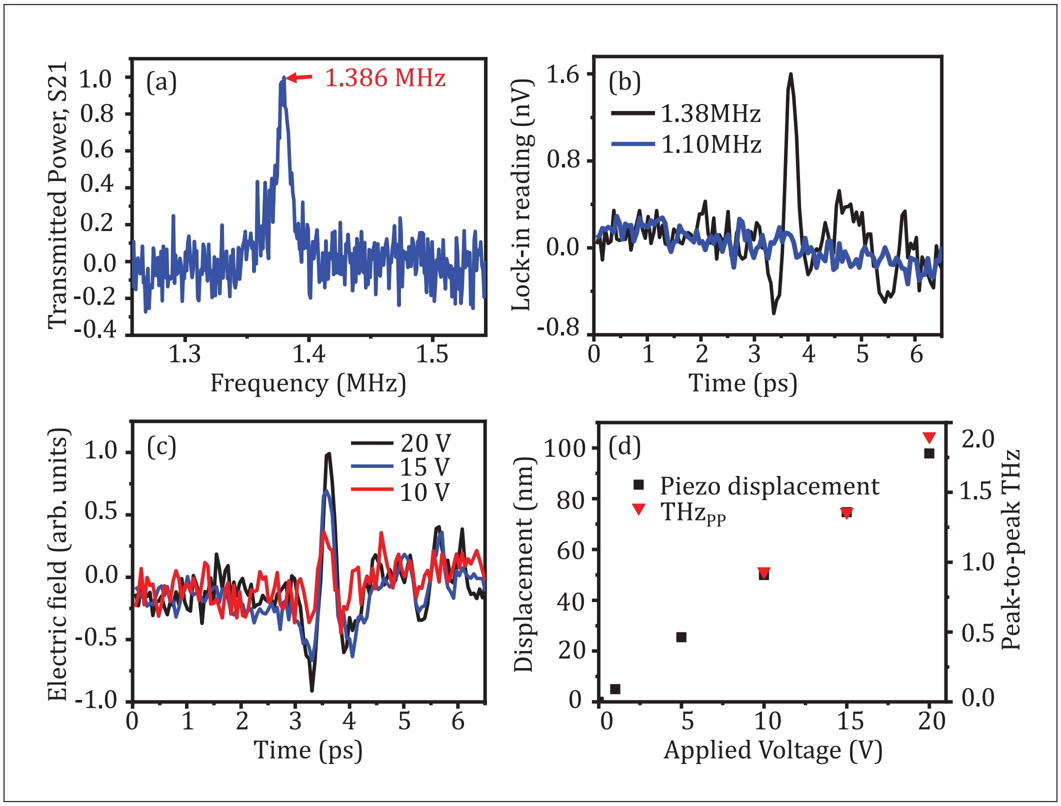

Figure 3.3 (a) Resonant frequency of all PMUTs obtained by a network analyzer (1.38 MHz), (b) Measured THz response at two PMUT resonant frequencies, 1.38 MHz and 1.10 MHz, using Mode B setup, (c) Dependency of the measured THz signal as a function of PMUT driving voltage at 1.38 MHz, and (d) Motion characterization of a PMUT unit cell with a vibrometer as a function of driving amplitude voltage with the corresponding peak-to-peak detected THz pulse

3.5 Result and Discussion

Figure 3.3 (b) shows the measured THz response for 1.38 MHz and 1.10 MHz exciting frequencies of the PMUT array. As expected from the network analyzer, no signal is observed for excitation at 1.10 MHz, i.e., when the device is not significantly oscillating. On the other hand, at a modulation frequency of 1.38 MHz, a nanovolt-scale THz signal in phase with the modulation of the PMUT array is clearly observed. We have to stress that for this experimental demonstration, the total active area of the PMUTs represents only 3.4% of the total irradiated THz beam size.

In addition, since each unit cell of the PMUT array is smaller than the wavelength (i.e., 200 μm in diameter), we expect strong diffraction of the THz wave to occur.

To confirm the effect of the PMUT motion on the detected THz waves, in figure 3.3 (c), we show the dependency of the measured THz signal as a function of the PMUT driving voltage at 1.38 MHz. Note that the applied voltage on the PMUT provides proportional changes in the amplitude of the detected differential THz signal. To relate the effect of the absolute motion of the PMUT array to the measured THz signal, figure 3.3 (d) shows the displacement of the PMUT, measured by a vibrometer and the THz peak-to-peak (pp) electric field, recovered in figure 3.3 (c), as a function of the control voltage. Both curves show a linear dependency on their respective scales. This dependency confirms the active control of the THz response in phase with the PMUT oscillating field strength and frequency. It is clear that for movements of 60 nm and less, i.e. for a control voltage of 10 V and less, the signal falls in the noise level.

In the last step, we investigate the signature of the modulated THz wave from the PMUT array. As the lock-in amplifier is referenced to the resonant frequency of the PMUT array (Mode B described in Figure 3.2 (b)), The detected THz signal is simply the subtraction of the electric field by itself shifted by the time path length difference induced by the upper and lower positions of the aluminum membrane of the PMUT array (see Figure 3.1 (d)). As shown in Figure 3.3 (d), for the maximum PMUT displacement of 100 nm, the corresponding roundtrip phase change in the THz beam path is only 0.66 fs. This change is two orders of magnitude less than the resolution of the stepping scan mode of the mechanical delay line, i.e., corresponding to a time interval of 53 fs for this experiment. In such a condition, the PMUT motion induces a differential signal response significantly greater than the detected bandwidth of the measured THz pulses. Instead, the difference signal reveals the variations of the THz electric field ΔE in Volt/cm/s. Mathematically, this can be expressed by the limit of m(t) as t approaches t_0 is m, the slope of the electric field at a given time t, where:

$$m = \lim_{t \to 0} m(t) = \lim_{t \to 0} \frac{f(t) - f(t_0)}{t - t_0} \approx \frac{\Delta E}{\Delta t} \tag{3.1}$$

This well-known behavior is at the core of calculus and modern mathematics, the so-called derivative function, and also expressed as dt when Δt tends towards zero. Figure 3.4 (a) shows the signal detection concept using a lock-in amplifier synchronized to the motion of the PMUT array. As the displacement of PMUTs increases due to the piezoelectric effect, the THz beam path difference Δt increases, and thus, the THz electric field difference ΔE also increases proportionally, i.e. as long as the slope does not change within the motion range of the PMUT. This situation is illustrated in Figure 3.4 (a) where the larger motion offers greater sensitivity ($\Delta E_2 > \Delta E_1$), but with the drawback of a low-pass filtering effect of the measured signal, as illustrated by the difference between the readings of slopes $m_1 > m_2$.

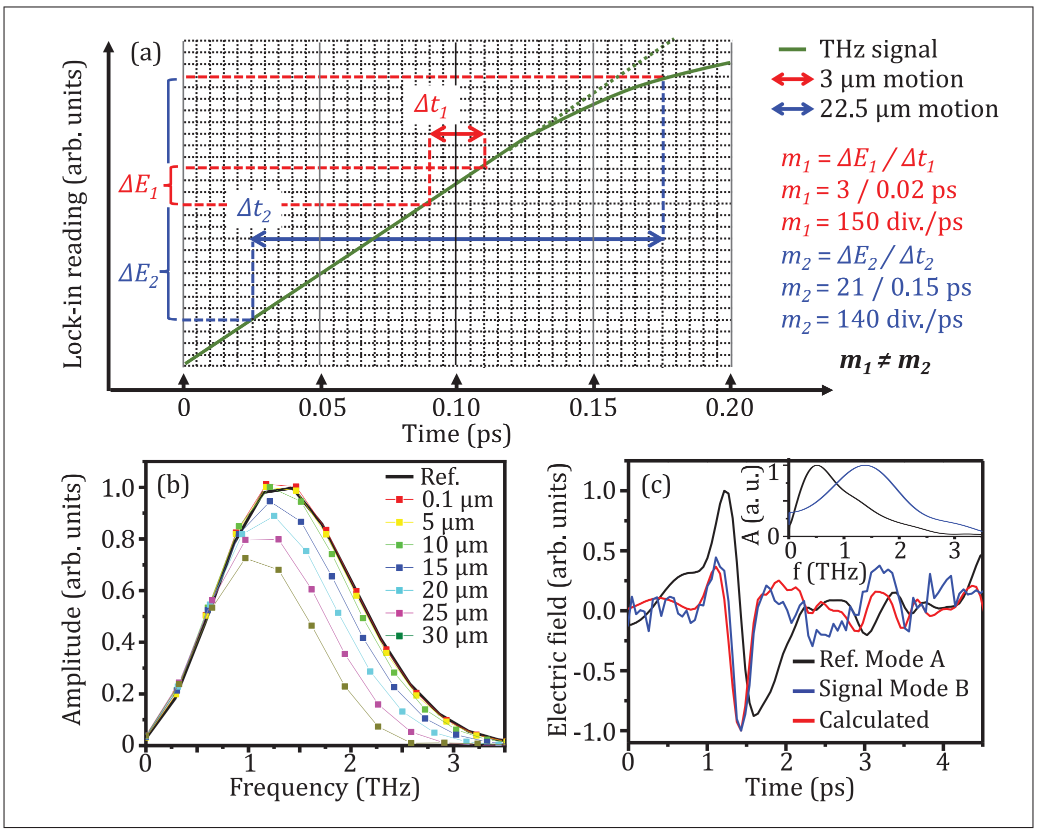

Figure 3.4 (a) Signal detection concept using a lock-in amplifier synchronized to the motion of the PMUT array. (b) Amplitude spectra dependency of the recovered signal as a function of PMUT array motions. (c) Measured Mode A (black) and Mode B signals (blue) with the calculated derivative signal (red) from the Mode A measurement

To quantify the impact of the increased PMUT motion on the derived function, we created a simulated reference signal with the same THz bandwidth as the experimental signal, i.e. 0.1 to 4.0 THz, but with a higher time resolution, i.e. 6.6×10^{-3} fs. The evaluation of the first-order derivative as a function of the displacement of the PMUT, Δt is obtained by inducing small phase differences (ranging from 0.6 fs to 200 fs, corresponding to 0.1 μm to 30 μm in PMUT motion) on this high temporal resolution signal. To ensure that this evaluation was representative of the experimental condition, we recovered the slope information only at a discrete time interval, e.g. for every 0.53 fs where Δt varies around these discrete time intervals. We then integrated the derived signals according to Δt and retrieved the amplitude spectrum of the recovered signals according to the movements of the PMUT array.

In Figure 3.4 (b), we show the amplitude spectra dependency of the recovered signal as a function of PMUT array motions. Interestingly, for motions of 5 μm and less, the spectral content remains almost unchanged in the 0 to 4 THz range and has a response similar to the reference spectra. For motions greater than 5 μm, spectra are progressively affected by the low-pass filtering effect, as illustrated in Figure 3.4 (a). In principle, to avoid losing the high-frequency component of the THz information, phase shifts that are at least two times smaller than the sampling timing should be considered. This would ensure satisfying the Nyquist theorem, which is highly respected in our demonstration.

Finally in Figure 3.4 (c), we plot the THz wave reflected by the PMUT array for both modulation types with respect to their absolute time scale: Mode A for emitter modulation (black curve), corresponding to all reflected THz waves on the device when the device is passive, and Mode B for PMUT array modulation (blue curve) when the device is active. The red curve in the same graph represents the calculated first-order derivative of the reflected THz pulse electric field obtained from Mode A (corresponding to $\frac{dE}{dt}$ of the black curve). Strikingly, an excellent match is found between the Mode B signal and the first-order derivative of the Mode A signal (see blue versus red curves). The amplitude spectra of mode A and B signals are presented in the inset. A shift at a higher frequency is found for the Mode B spectrum, consistent with the derivative function.

3.6 Conclusion

Summing up, we have demonstrated a simple method to actively modulate THz waves in reflection mode using a PMUT array as a differentiator. This modulator enables the reconstruction of the time derivative of the THz pulse back-reflected from its surface, i.e., supplying an output proportional to the derivative of the input. Such differentiators are highly anticipated for the future of data transmission in THz telecommunications. Derivation could also be of interest for spectroscopy because it allows spectral information to be shifted from low to high frequencies and to quickly identify the rate of change of the THz signal, which could be particularly interesting for non-linear processes identification in the THz band (Salén, Basini, Bonetti, Hebling, Krasilnikov, Nikitin, Shamuilov, Tibai, Zhaunerchyk & Goryashko (2019)). Our result confirms the merit of microelectromechanical devices for manipulation and control of THz waves and suggests the use of PMUTs with larger motions to improve sensitivity and to work at a lower frequency (Gratuze, Alameh & Nabki (2019)), which are already in preparation.

3.7 Acknowledgment

F.B. gratefully acknowledges financial support from NSERC (grant 2016-05020), FRQNT and the ÉTS-Chaire in THz optoelectronics. F.N. acknowledges financial support from NSERC (grant number 2016-04871).

3.8 Supplementary Information

This document provides supplementary information to the article entitled “Active terahertz time differentiator using piezoelectric micromachined ultrasonic transducer array”. We start by describing the fabrication flow of piezoelectric micromachined ultrasonic transducers (PMUT) with their electrical and mechanical characterization by a vector network analyzer and vibrometer-based methods, respectively. Then we evaluate the amount of THz modulated power that reaches the THz-TDS system’s detector. Finally, we establish the relationship between PMUT array motions and the phase

3.8.1 Fabrication flow of PMUT

Figure 3.5 shows a visualization of the piezoelectric micromachined ultrasonic transducer (PMUT) array using scanning electron microscopy (SEM). As can be seen in Figure 3.5 (a), the arrangement of the PMUT is linearly spaced, with a distance of 500 μm separating them. The PMUT device is a free-standing 200 μm diameter silicon membrane anchored using four 20 μm-wide and 30 μm-long arms (or anchors). The silicon membrane acts as the bottom electrode, and is covered by a layer of Aluminum Nitride (AlN) acting as the piezoelectric material. The AlN layer, for its part, is covered by an aluminum layer acting as the top electrode (Robichaud *et al.* (2018b); Robichaud, Cicek, Deslandes & Nabki (2018a)).

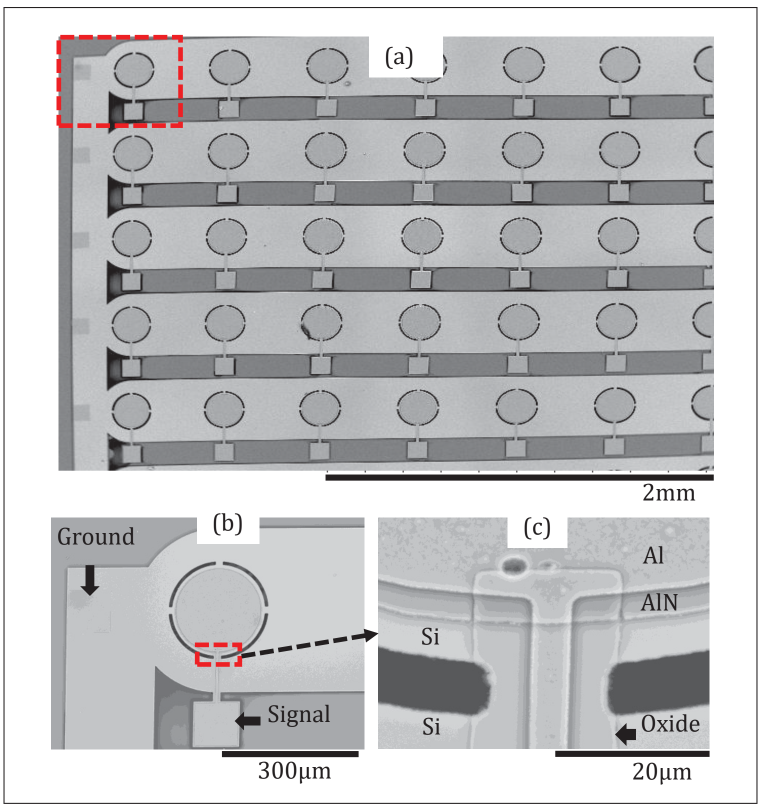

Figure 3.5 SEM micrographs of the fabricated PMUT: (a) view of the PMUT array, (b) close-up view of one PMUT, (c) detailed view of the layers

Figure 3.5 (b) presents a view of a single PMUT, with an indication of two electrodes for signal and ground. In this figure, we can clearly see the anchoring of a single PMUT. In Figure 3.5 (c) we show a detailed view of the anchor, where the signal is taken, and which clearly identifies all layers used in the manufacture of the PMUT.

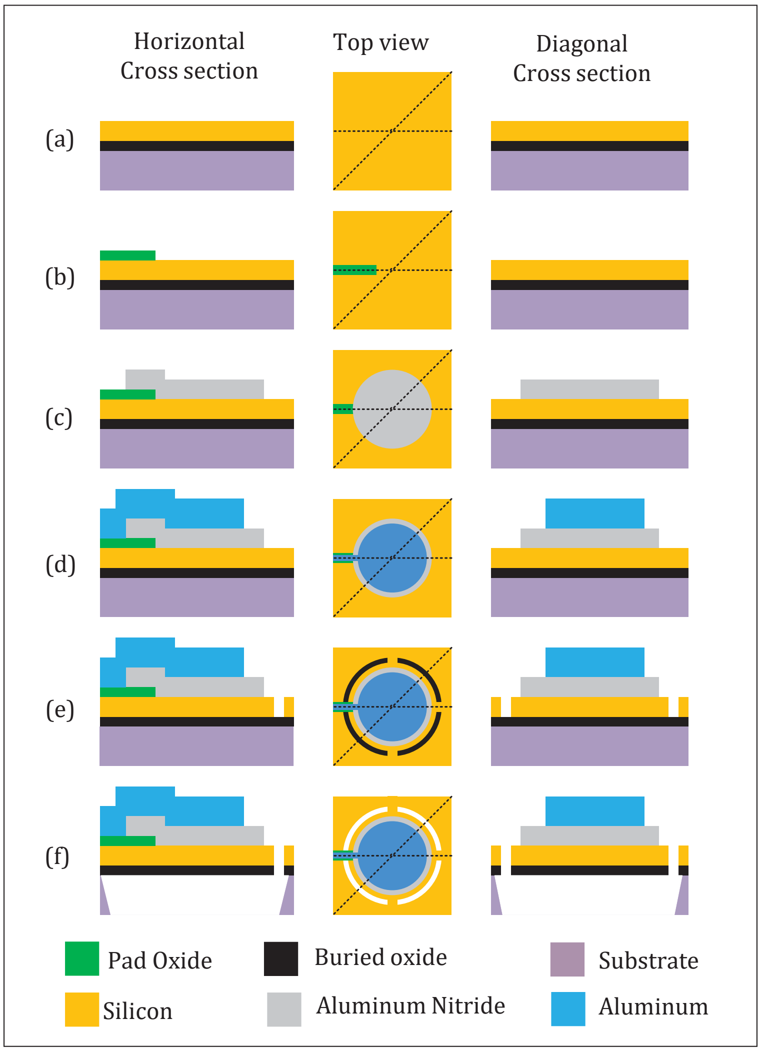

Figure 3.6 Piezo MUMPS process flow for the fabrication of a PMUT and post-processing: (a) SOI wafer, (b) growth of thermal oxide, (c) deposition of aluminum nitride, (d) deposition of aluminum, (e) etching of silicon (f) membrane release

The PMUT array was fabricated using the commercial Piezo, Multi-User MEMS Processes (MUMPS) process by MEMSCAP (Cowen, Hames, Glukh & Hardy (2014)), and the fabrication steps are illustrated in Figure 3.6. The process starts with using a Silicon On Insulator (SOI) wafer composed of a 400 μm thick silicon layer, a 400 nm thick insulator layer and a 10 μm thick silicon layer (Figure 3.6 a). Electrical conduction is achieved by doping the substrate, followed by the thermal growing of a 200 nm thick pad oxide layer (Figure 3.6 b) by photolithography. This step allows electrical insulation between the two electrodes. Afterward, a 500 nm AlN layer is deposited as a piezoelectric material by sputtering (Figure 3.6. c). The top electrode is created by the deposition and patterning of a 1 μm thick and 180 μm diameter aluminum layer (Figure 3.6. d). Later, the silicon device layer is etched by Deep Reactive-Ion Etching (DRIE), resulting in a 200 μm diameter circular silicon membrane (Figure 3.6. e). The diameter of the silicon structure is made deliberately larger than the aluminum nitride to ensure no overhang of the piezoelectric material. Finally, the membrane is released by etching a trench from the back of the handle wafer (or substrate) by DRIE (Figure 3.6. f).

3.8.2 Electrical response of PMUT from Network analyzer

A network analyzer is a device with input and output ports that measures the transmitted or reflected power of a signal that passes through the Device Under the Test (DUT). The measurement of reflected power via scattering parameters S11 and S22 or transmitted power using scattering parameters S21 and S12 can be performed. The measurement is based on transmitted or reflected energy from the DUT. The measure of the S parameters allows the identification of the resonant frequency of the DUT. For example, by transferring alternative power through the DUT, S21 and S12 will experience higher power when DUT is resonating rather than when DUT is not resonating. In our case, the average resonant frequency of the PMUT is measured using a Vector Network Analyzer from Keysight, model E5061B, with the 64 PMUT devices connected in parallel in the PMUT array. The resonant frequency of PMUT array is measured via S21 by passing the power between both electrodes of the PMUT array.

3.8.3 Modulated THz power at the detector

Here, we are interested in evaluating the maximum detected modulated THz power at the detection position. To that end, we first estimate the THz intensity (I_{THz}) from the emitter reaching the PMUT array, with the THz power (P_{THz}) transferred per unit area (A) (i.e., $I_{THz} = P_{THz}$/A). The emitted THz beam is collimated by a 12 mm diameter spherical lens and assuming a Gaussian THz irradiation. The half-power beam width (HPBW) is $1/e^2$ of the THz beam's peak irradiance, which corresponds to a radius of 4.31 mm. Therefore, for the maximum generated THz power of 6 μW (Ltd) and a THz beam area of 58.3 mm^2 (π×4.312), the intensity at the PMUT array position is approximately 100 nW/mm^2.

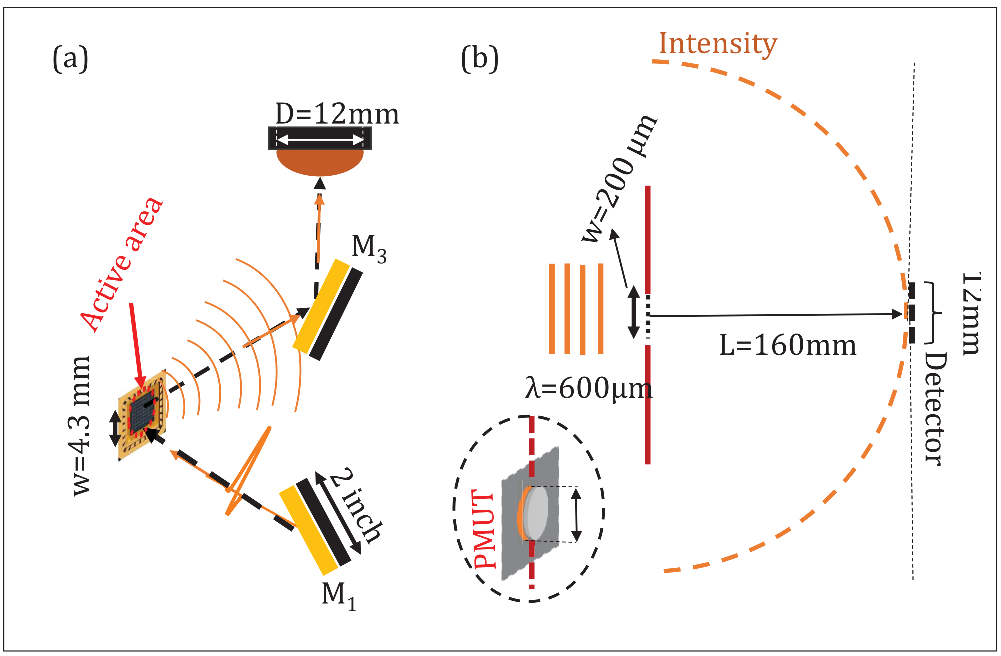

Figure 3.7 Illustration of (a) an experimental setup scheme when THz beam travels from M_1 to PMUT array and then reaches the detector, (b) diffraction effect from a single PMUT

To estimate the THz modulated power after reflection on the PMUT array, we added up the active area covered by the 64 PMUT array, as illustrated in Fig. 3.7 (a). Each PMUT was 200 μm in diameter, and we found a corresponding active area of 2 mm^2 for 64 PMUT (64×π×0.12). This area over the THz beam area represents only 3.4% of the THz beam irradiance. By multiplying the THz intensity at the PMUT position by the active area, we found a modulated THz power of 200 nW.

In addition, since each PMUT (unit cell) has an active area of 200 μm in diameter, and assuming a central frequency of around 0.5 THz, as shown in Figure 3.2 (c), the corresponding wavelength of 600 μm indicates a large diffraction effect. As predicted by the first-order diffraction represented by equation 3.2, it is clear that θ cannot be solved for this situation, indicating the diffraction behavior of a point source:

$$W sin(\theta) = m\lambda \tag{3.2}$$

where w is the size of one PMUT, λ is the wavelength of the THz wave (600 μm), and θ is the angle at which the first minimum for m = 1 is found. Given a distance of 160 mm from the PMUT array to the detector, a half-spherical surface is around 160×103 mm^2 (2π×160 mm^2), as illustrated in Figure 3.3 (b). Therefore, the corresponding intensity at the detector position is 1.25 pW/mm^2. Finally, to retrieve the THz power detected, we multiplied the THz intensity by the collecting lens area of the detector (i.e., 6 mm radius Si hemispherical lens). This results in a maximum power of 141 pW (1.25 pW/mm^2 ×113 mm^2) at the detection position, which represents a ratio of the detected modulated THz power of only 0.0023% of the total transmitted THz power.

3.8.4 Mechanical response of PMUT from Vibrometer method

Contrary to the vector network analyzer which measures an electrical response, the vibrometer method optically measures the mechanical response of the PMUT. The vibrometer is used to carry out non-contact vibration measurements of a point using the Doppler effect. In this fashion, the amplitude and frequency of a mechanical motion can be characterized. The laser of the vibrometer is then targeted at the center of a PMUT membrane (as shown in Fig. 3.8). Time-domain measurements were undertaken using a function generator and a Polytec OFV-5000 vibrometer.

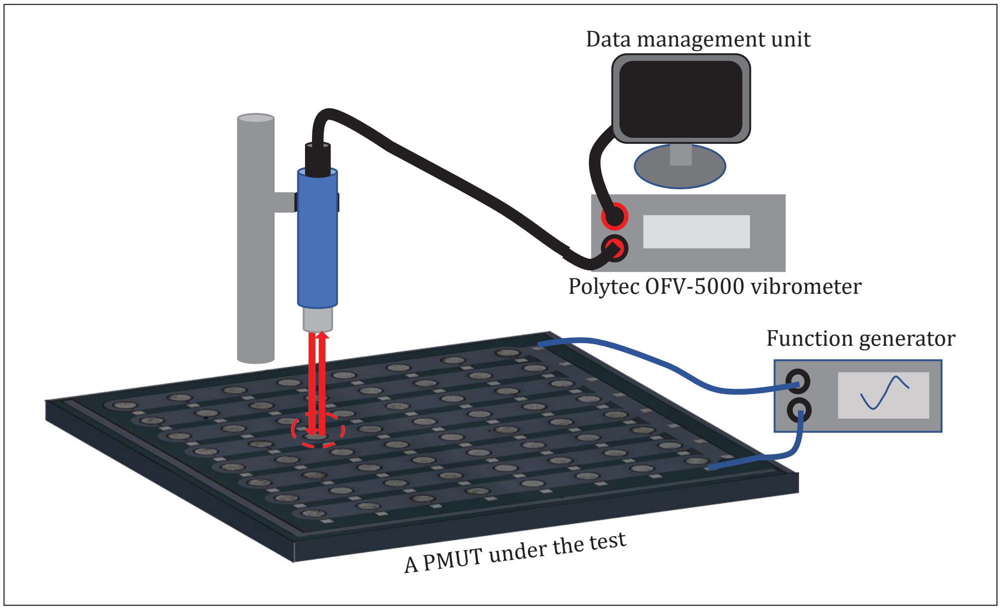

Figure 3.8 Schematic of the test bench using the vibrometer to characterize a PMUT

The function generator type 33 250A from Agilent is used to provide an electrical excitation to the PMUT (a 1.38 MHz sinusoidal signal with 20 V peak-to-peak amplitude). Then, the PMUT transforms this electrical excitation into a mechanical excitation, i.e., a displacement. The PMUT vibrates optimally at this specific frequency, which is the mechanical resonance frequency. The amplitude of displacement is linearly proportional to the applied voltage.

3.8.5 Phase shift on derivative signal induced by PMUT motions

To evaluate the impact of PMUT motions on the derivative function, we created a simulated reference signal with a 6.6×10-3 fs time resolution and calculated its first-order derivative response as a function of PMUT displacement. To ensure this evaluation was representative of the experimental condition, we retrieved the slope signal only at discrete time frames, e.g., same as in the experiment for every 53 fs. This is illustrated in Fig. 3.9, where δt varies around these discrete time frames.

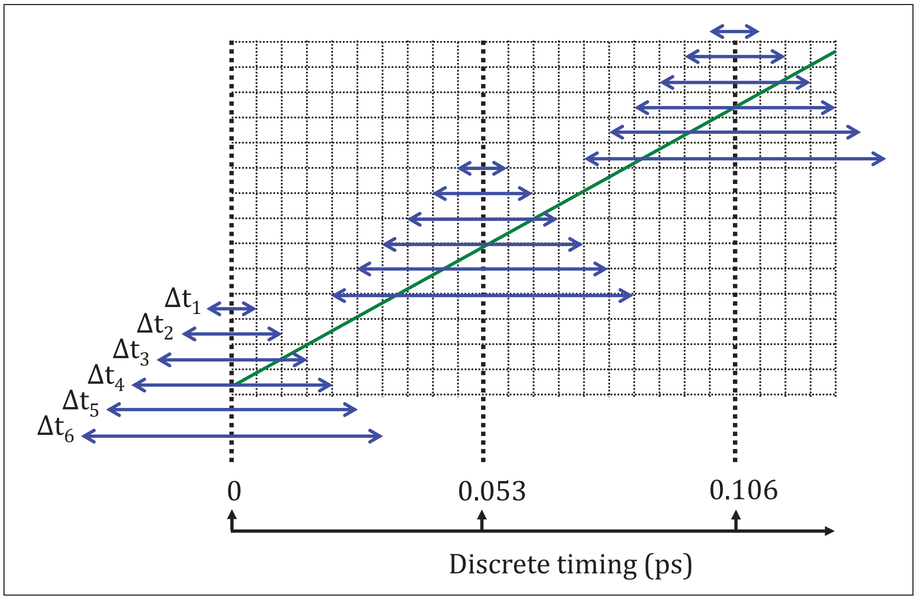

Figure 3.9 Illustration of the differentiation principle. The motion of the PMUT array induces a THz beam path change proportional to δt. The slope measurement is differentiated according to temporal size δt (e.g., where $\delta t_1 < \delta t_2$), and is only retrieved for discrete positions every 53 fs

The result of this evaluation is presented in Fig. 3.10 (a) for some selected displacements: 50 nm, 20 μm, 30 μm, 35 μm and 45 μm. The same calculations are performed for the discrete position every 0.33 fs in Fig. 3.10 (b). In these two figures, the reference signals and their first-order derivative calculations are evaluated as a function of time delay δt ranging from 0.33 fs to 133.3 fs, also corresponding to 50 nm to 45 μm in PMUT motion, respectively. Note that sub few microns motions would be the highest practical range.

In Fig. 3.10 (a) and (b), as δt increases, a clear shift of the peak position of the derivative signal towards negative time is observed. Phase shift-related information is summarized in Fig. 3.4(b) of the main document. To have an idea of the impact of the phase shift on the experimental data, we have, in Figure 3.10 (c), integrated the calculated derivative signals of Figure 3.10 (b) and compared them with the reference signal. Note that the reference signal was created with the same THz bandwidth as the experimental one, i.e., from 0.1 to 4.0 THz. It is clear that the THz signal recovered from the derivative one is highly dependent on PMUT motions.

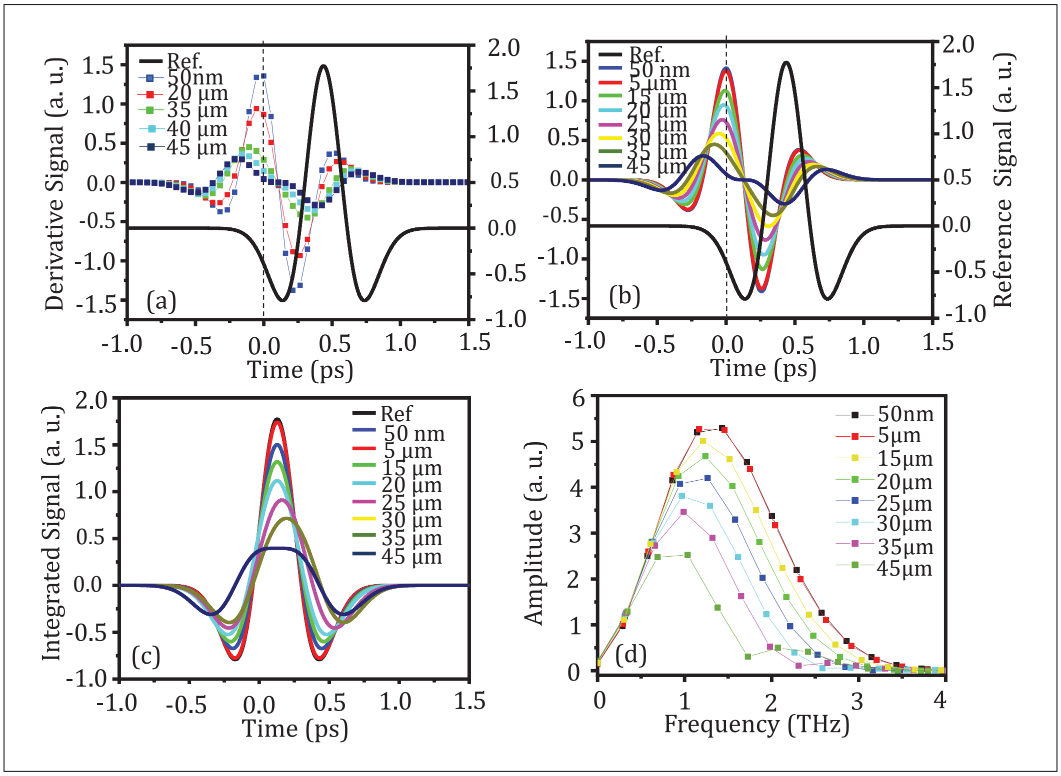

Figure 3.10 Illustration of (a) and (b) time variations of the calculated first derivative of a simulated signal based on different displacements at discrete times 53.3fs and 0.33 fs, respectively, (c) integration of selected first derivative of signals, (d) amplitude spectra dependency of the recovered signal as a function of PMUT array motions

Finally, to estimate the amplitude spectrum dependency of the recovered signal as a function of PMUT array motions, we show the amplitude spectra obtained by Fast Fourier Transform (FFT) of the integrated signals calculated in Figure 3.10. From that figure, we can confirm that the PMUT motion of 100 nm used in our experiment does not induce any change in the spectral domain, which confirms the ability of the broadband to induce phase change on a THz signal with this novel modulator.

CHAPTER 4

TERAHERTZ TIME-DOMAIN DERIVATIVE SPECTROMETER USING A LARGE-APERTURE PIEZOELECTRIC MICROMACHINED DEVICE

Fatemeh Amirkhan[1] , Mathieu Gratuze[1] , Xavier Ropagnol[1,2] , Tsuneyuki Ozaki[2] , Frederic Nabki[1] , François Blanchard[1]*

[1] Department of Electrical Engineering, École de technologie supérieure,
1100 Notre-Dame West, Montreal, Quebec, Canada H3C1K3
[2] Institut national de la recherche scientifique,
Varennes, Quebec, Canada J3X 1P7

Paper published in Journal of the Optical Society of America Optics Express, July 5, 2021.

Résumé

L'ingénierie des systèmes optomécaniques a explosé au cours des dernières décennies, avec de nombreuses géométries et applications découlant du couplage de la lumière avec le mouvement mécanique. La modulation du rayonnement électromagnétique dans la gamme de fréquences térahertz (THz) par des systèmes optomécaniques ne fait pas exception à cet effort de recherche. Cependant, certaines capacités de modulation fondamentales pour les communications THz et/ou les applications de traitement de données à grande vitesse restent à établir. Nous démontrons ici un spectromètre dérivé THz dans le domaine temporel basé sur un dispositif piézoélectrique micro-usiné (PM). L'insertion du dispositif PM dans le trajet du faisceau THz fournit une modulation de référence pour l'unité de détection à verrouillage, qui à son tour donne accès à l'information dérivée d'ordre n du signal THz entrant. De manière frappante, l'intégration du signal dérivé enregistré conduit à un signal de référence récupéré avec un rapport signal/bruit équivalent ou même meilleur, ouvrant la porte à un nouveau type de mesures THz hautement sensibles dans le domaine temporel.

4.1 Abstract

The engineering of optomechanical systems has exploded over the last decades, with many geometries and applications arising from the coupling of light with mechanical motion. The modulation of electromagnetic radiation in the terahertz (THz) frequency range through optomechanical systems is no exception to this research effort. However, some fundamental modulation capabilities for THz communications and/or high-speed data processing applications are yet to be established. Here, we demonstrate a THz time-domain derivative spectrometer based on a piezoelectric micromachined (PM) device. Insertion of the PM device into the THz beam path provides reference modulation for the lock-in detection unit, which in turn provides access to the nth-order derivative information of the incoming THz signal. Strikingly, the integration of the recorded derived signal leads to a recovered reference signal with an equivalent or even better signal-to-noise ratio, opening the door to a new type of highly sensitive THz measurements in the time-domain.

4.2 Introduction

In recent decades, the development of several techniques for the generation and detection of electromagnetic waves in the terahertz (THz) frequency range (Tonouchi (2007); Song & Nagatsuma (2015)) has led to a wide range of applications in the fields of security (Kawase, Ogawa, Watanabe & Inoue (2003); Liu, Chen, Bastiaans & Zhang (2006)), nondestructive testing (Zhong (2019); Zhuldybina, Ropagnol, Bois, Zednik & Blanchard (2020)), spectroscopy (Van Exter *et al.* (1989); Ferguson & Zhang (2002); Hafez, Chai, Ibrahim, Mondal, Férachou, Ropagnol & Ozaki (2016)), telecommunications (Nagatsuma *et al.* (2016); Elayan, Amin, Shihada, Shubair & Alouini (2019)), imaging (Mittleman (2018); Guerboukha, Nallappan & Skorobogatiy (2018)) and microscopy (Amirkhan, Sakata, Takiguchi, Arikawa, Ozaki, Tanaka & Blanchard (2019); Blanchard *et al.* (2013); Cocker, Jelic, Gupta, Molesky, Burgess, De Los Reyes, Titova, Tsui, Freeman & Hegmann (2013)). In order to improve the performance of THz systems in these various applications, the design of innovative and efficient modulators in this frequency range is the subject of intense research activity (Rahm, Li & Padilla (2013); Wang *et al.* (2019b); Ma *et al.*

(2019)), particularly for sensing applications (Rahm *et al.* (2013); Wang *et al.* (2019b)) and data transmission systems (Ma *et al.* (2019)). As in the world of optics for ultrafast signal processing (Salem *et al.* (2013), it would be necessary to design and implement fundamental mathematical operators, such as differentiator (Slavík, Park, Kulishov, Morandotti & Azaña (2006)), integrator (Park, Ahn, Dai, Yao & Azaña (2008)) and Hilbert transformer (Asghari & Azaña (2009)). A differentiator is one of these fundamental operators that perform the mathematical action of differentiating an input signal. In the same way, an nth-order derivative type differentiator provides an nth-order derivative type output signal derived from an arbitrary input signal, which can be a function of time, frequency or wavelength (Ngo *et al.* (2004)). Differentiators have been realized for the ultrafast processing of light in the temporal, spatial and spectral domains, which have generally been realized using special fiber-optic routing and wave-mixing devices (Zhang *et al.* (2021c)). When dealing with slowly varying optical signals, a simple method to obtain the derivative of the input signal is the use of a resistor-capacitor (RC) filter in combination with a modulation device in the optical path, such as a tachometer (Klein & Dratz (1968)). This latter case is a well-established method that has been used for decades is known as derivative spectroscopy (Klein & Dratz (1968); Dubrovkin (1983); Holcomb & Little (1992); Wiley *et al.* (2009); Karpińska (2004)).

While the ultrafast optical differentiator (Salem *et al.* (2013); Slavík *et al.* (2006); Park *et al.* (2008); Asghari & Azaña (2009); Ngo *et al.* (2004); Zhang *et al.* (2021c)) and derivative spectroscopy (Klein & Dratz (1968); Dubrovkin (1983); Holcomb & Little (1992); Wiley *et al.* (2009); Karpińska (2004)) approaches to deal with the complex envelope of the intensity profile of an input signal, THz measurement systems provide direct access to the amplitude and phase of the electric field, thanks to coherent methods of generation and detection by sampling (Blanchard *et al.* (2007); Wu & Zhang (1996a)). This additional feature can have several advantages for signal processing in the THz range. One such advantage is the use of low-frequency electronic tools, such as a lock-in amplifier, to recover ultra-fast THz phenomena (Neu & Schmuttenmaer (2018)). Since a lock-in amplifier is already a sophisticated RC filter, the addition of a suitable modulator only could in principle transform the traditional THz time-domain spectroscopy

(THz-TDS) system (Zhuldybina *et al.* (2020); Neu & Schmuttenmaer (2018)) into a THz time-domain derived spectrometer (THz-TDDS). Using electronics, an accurate reading of the derived THz signal could quickly measure the slope and/or the position of the peak in the time-varying signal (Skolnik (1962)). Derived information could also be applied to allow the precise identification of fixed points, such as local maxima and minima. The latter case could be of great interest for THz phase-contrast imaging, improving the accuracy of layer detection (Redo-Sanchez *et al.* (2016)) or refractive index changes (Blanchard *et al.* (2014b)). However, to date, only a few attempts have been made to demonstrate passive THz time differentiators, using a grating (Filin *et al.* (2001)) and a silicon ring resonator (Xie *et al.* (2020)). More recently, we reported an active THz time differentiator with an 8×8 piezoelectric micromachined ultrasonic transducer (PMUT) array (Amirkhan, Robichaud, Ropagnol, Gratuze, Ozaki, Nabki & Blanchard (2020)). Nevertheless, the latter demonstration was limited due to the small pixel size (i.e., sub mm^2) and the small motion of the PMUT unit cell relative to the THz propagation path. Additionally, the need to use a voltage driver with a MHz-scale oscillator to sustain the resonant frequency of the PMUT array made its use less convenient for the lock-in amplifier.

Accordingly, we demonstrate here an nth-order THz time-domain derivative spectrometer using a piezoelectric micromachined device (PM) with a surface area that is larger than 1 mm^2 and operating in the kHz frequency range. Originally designed for energy harvesting (Gratuze *et al.* (2019)), once inserted in the THz beam path as a modulator, this new device has an impressive performance to accurately measure not only the first derivative of the incoming signal, but our results show a good response up to the fourth-order derivative. This paper is organized as follows; we first present the proposed structure for PM devices and its functionality. We also explain the operating principle of the lock-in amplifier to access the multiple-order derivative of the incoming THz signal. We then describe the experimental setup and the results obtained. Finally, we show the good agreement of our experimental results with the simulations and demonstrate the ability to recover the original signal with high accuracy by integrating the information from the differentiated signal.

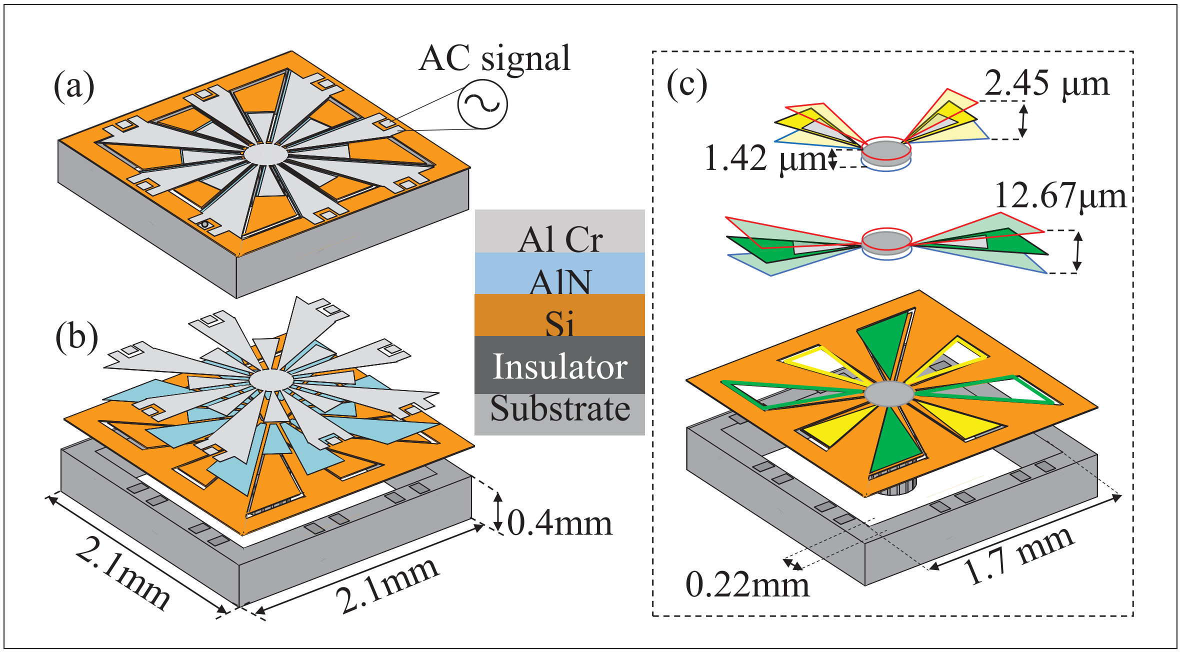

Figure 4.1 Illustration of (a) the PM device, (b) with its layers of aluminum chromium (Al Cr), aluminum nitride (AlN), silicon (Si), and on a silicon-on-insulator substrate. (c) A graphical representation of the complex motion of the three separate areas of the PM surface; the center, yellow wings, and green wings, with lengths of 12.67 μm, 2.45 μm, and 1.42 μm, respectively

4.3 PM device material and its characteristics

Fig. 4.1 (a) shows the PM device with its electrodes for controlling and activating displacements. The PM device has been fabricated using the commercial PiezoMUMPS process from MEMSCAP, detailed in (Cowen *et al.* (2014)). The design, fabrication and characterization of such PM are detailed in Gratuze et al. (Gratuze *et al.* (2019)). The surface area covers 2.1×2.1 mm^2 on a 0.4 mm thick silicon-on-insulator (SOI) substrate. This metallic multilayer device (see Fig. 4.1 (b)) consists of a stack of from top to bottom: 1 μm thick aluminum (Al), 0.02 μm thick chromium (Cr), and a 0.5 μm thick piezoelectric material (aluminum nitride) deposited on the 10 μm thick top silicon (Si) layer of the SOI substrate. As shown in Fig. 4.1 (a), the metallic multilayer acts as an upper electrode layer and the Si layer acts as the lower electrode to piezoelectrically control the displacement of the structure. To avoid short circuits where needed, an additional insulating layer of silicon dioxide with 0.2 μm is deposited between the Si layer and the metallic multilayer stack.

To allow large vertical movements around its resting position, the structure is suspended above an empty cavity with an area of 1.7×1.7 mm^2, as illustrated in Fig. 4.1 (c). Inside this cavity, the maximum round-trip displacements perpendicular to the plane of the substrate for the green wing, the yellow wing and the central (grey) part of the device are 12.67 μm, 2.45 μm and 1.42 μm, respectively. Indeed, these values are based on the simulation and measurement of the mode shape of the PM device as presented in (Gratuze *et al.* (2019)). The PM device is a resonator, and therefore it is possible to excite it with a sinusoidal signal, in which case each moving part of the PM will oscillate at the same frequency. Thereafter, this frequency will be referred to as the modulation frequency (f_{mod}). To achieve the maximum displacement at f_{mod}, an external sinusoidal voltage amplitude 20 V peak-to-peak at 10.82 kHz is applied across the electrodes.

4.4 Principle of operation

To understand the difference between a typical THz wave measurement and the use of our device, it is important to recall the basic concept of lock-in detection. As illustrated in the supplementary info (Fig.S1), a lock-in amplifier is a kind of alternating current (AC) voltmeter that mixes an input signal with a periodic reference signal (Kloos (2018)). For THz-TDS measurements, the electro-optical sampling method is commonly used and requires a lock-in amplifier (Neu & Schmuttenmaer (2018)). This method involves either a mechanical chopper or control of the bias voltage of a photoconductive antenna (PCA), the latter acting as an ON-OFF switch of the input signal. Unlike the electronic modulation of a PCA or the mechanical chopping of the THz signal, our device does not modulate the input signal ON and OFF. In fact, the PM device induces a small change in the path length of the THz beam (Amirkhan *et al.* (2020)). This modulation causes the physical system we are interested in (i.e., the THz signal) to respond with a frequency f_{mod}, whereas the detector and lock−in amplifier convert its response into a voltage. For a lock-in amplifier, a stimulus x(t) of amplitude A and oscillating with an angular frequency Ω_{mod}, which is $2\pi f_{mod}$, around an average value $\bar{x}$ can be expressed by:

$$x(t) = \bar{x} + A sin(\Omega_{mod} t). \tag{4.1}$$

Upon application of the stimulus, the detector reads a time-varying signal V(t):

$$V(t) = V(x(t)). \tag{4.2}$$

Under the assumption that the modulation A is sufficiently small, we can approximate V(x(t)) by a Taylor-series expansion about $\bar{x}$. Passing through the lock-in amplifier provides an output that is proportional not only to the modulation A, but also to the derivative of the system's response to the stimulus, evaluated at $x = \bar{x}$ (Kloos (2018)):

$$V_{out} \approx \frac{A}{\sqrt{2}} \frac{dV}{dx} |_{\bar{x}} \ . \tag{4.3}$$

According to equation (4.3), changing the ON-OFF modulation for a change in THz path length converts a THz-TDS system into a THz derivative spectrometer. Furthermore, as with derivative spectroscopy (Holcomb & Little (1992)), reading the Nth-order harmonic signal from the lock-in should, in principle, provide access to the Nth-order derived function of the modulated signal (Kloos (2018)). To describe the functionality of a THz derivative spectrometer obtained by combining a PM device with a lock-in amplifier, we show in Fig.4.2 the relationship between the motion of a part of the PM device (see the green wings at the top of the figure) as a function of the lock-in detection phase. In Fig.4.2 (a), assuming an excitation frequency at f_{mod} with 20 V peak-to-peak, a phase change of 2π corresponds to a complete excursion of about 12.66 μm on the wing edge. In such a condition, the PM motion still induces a sufficiently small differential response $\Delta E/\Delta t$, i.e., greater than the detected bandwidth of the measured THz pulses (Amirkhan *et al.* (2020)), to recover a derivative measurement. In Fig.4.2 (b), (c) and (d), we show the value of the phases with respect to the excitation frequency f_{mod} corresponding to the second, third and fourth harmonic functions of the lock-in amplifier, respectively.

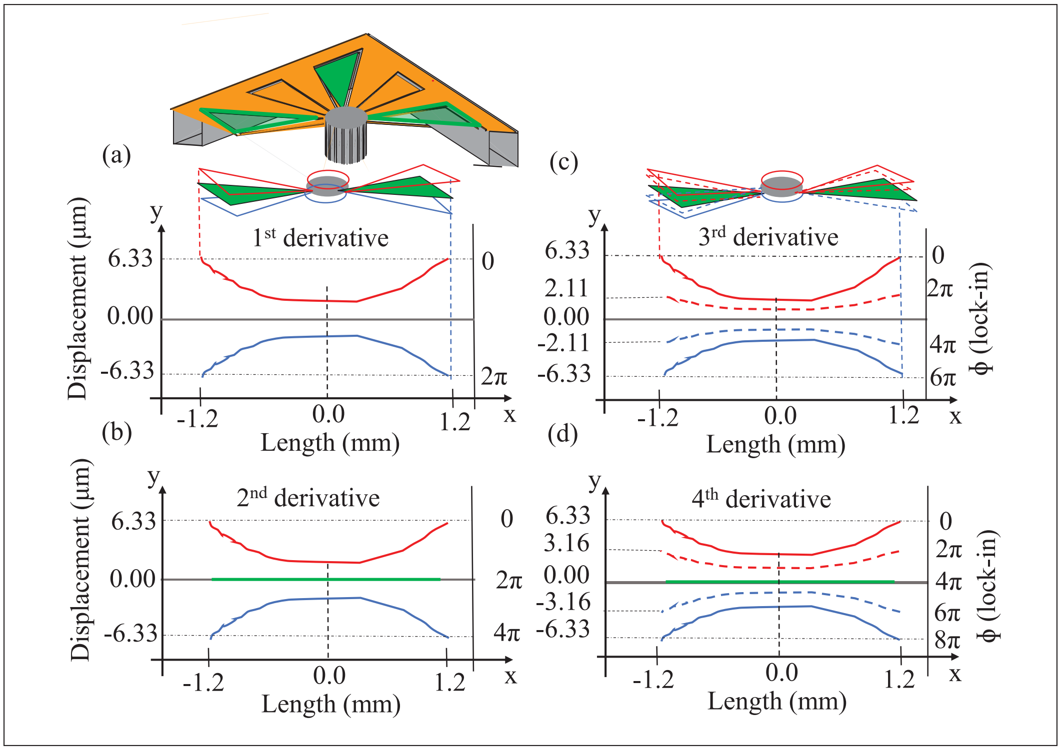

Figure 4.2 Illustration of the displacement of a PM device in the y-direction relative to its x position, all in relation to the phase interpretation of the lock-in amplifier for the measurement of (a) 1^{st}-order, (b) 2^{nd}-order, (c) 3^{rd}-order, and (d) 4^{th}-order derivatives

In these cases, the harmonic function of the lock-in amplifier allows the slope of the slope to be determined, and so on as the harmonic value is increased (for more information, see supplementary S1).

4.5 Experimental setup and results

Terahertz spectroscopy (Jepsen *et al.* (2011)) is well-known for the characterization of THz devices, such as modulators (Wilk, Vieweg, Kopschinski & Koch (2009)), filters (Lo & Murphy (2009)) and artificial metamaterials (Padilla *et al.* (2006)), to name a few applications. Similar to these experiments, we employed a THz-TDS system based on the transmission and detection of THz waves by two PCAs from TeraVil Ltd. The PCAs were pumped using a Ti:Sapphire laser oscillator providing 810 nm, 40 fs laser pulses at a repetition rate of 80 MHz and an average power of 20 mW on each antenna. The hemispherical silicon lens at the back of the transmitting antenna collimates the THz output beam with a diameter of about 10 mm. As shown in Fig.4.3(a), the collimated THz beam is guided by a gold-coated flat mirror, followed by a concave mirror 3 inches in diameter and 3 inches in focal length. The PM device is located exactly at the focus of the concave mirror, and the reflected beam returns symmetrically to the opposite side of the concave mirror, where the THz beam is recollimated. Finally, another gold-coated flat mirror guides the THz beam to the high resistivity hemispherical silicon lens of the PCA detector. The latter focuses the THz beam on the micrometer gap of the antenna.

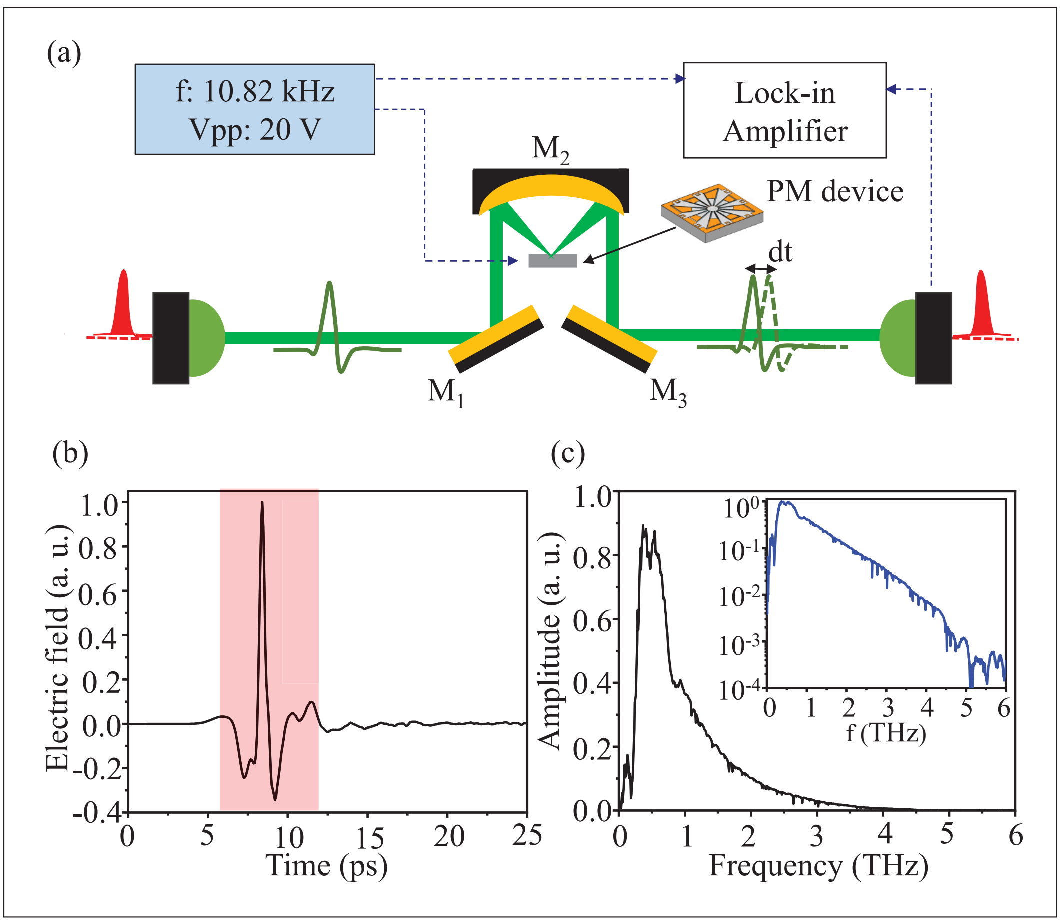

Figure 4.3 Demonstration of (a) the experimental setup in reflection geometry using a gold-coated concave mirror (in position of M_2) of 3-inch focal distance and a signal generator to drive the PM device to modulate the THz signals. (b) and (c) are the measured THz pulse and its spectrum, respectively, when the modulation is applied to the antenna. The inset in (c) shows the measured reference spectra

In order to study the behavior of our PM device, we first measured the THz signal without any external electric field applied to the device, as shown in Fig.4.3 (b). In this case, the PM device is considered at rest, behaves like a metallic mirror, and only the THz transmitting antenna is biased with a voltage of 40 V modulated at a repetition frequency of 30 kHz. This ON-OFF modulation on the emitted field of the transmitting antenna is the typical lock-in detection operation used for the standard THz-TDS configuration (Jepsen *et al.* (2011)), hereinafter referred to as the THz reference measurement. Fig.4.3 (b) and (c) show the THz pulse reflected from the PM device (i.e., in the state of rest) and its fast Fourier transform (FFT) spectra, which reveal a bandwidth of 0 to 5 THz with the central frequency located at 0.7 THz.

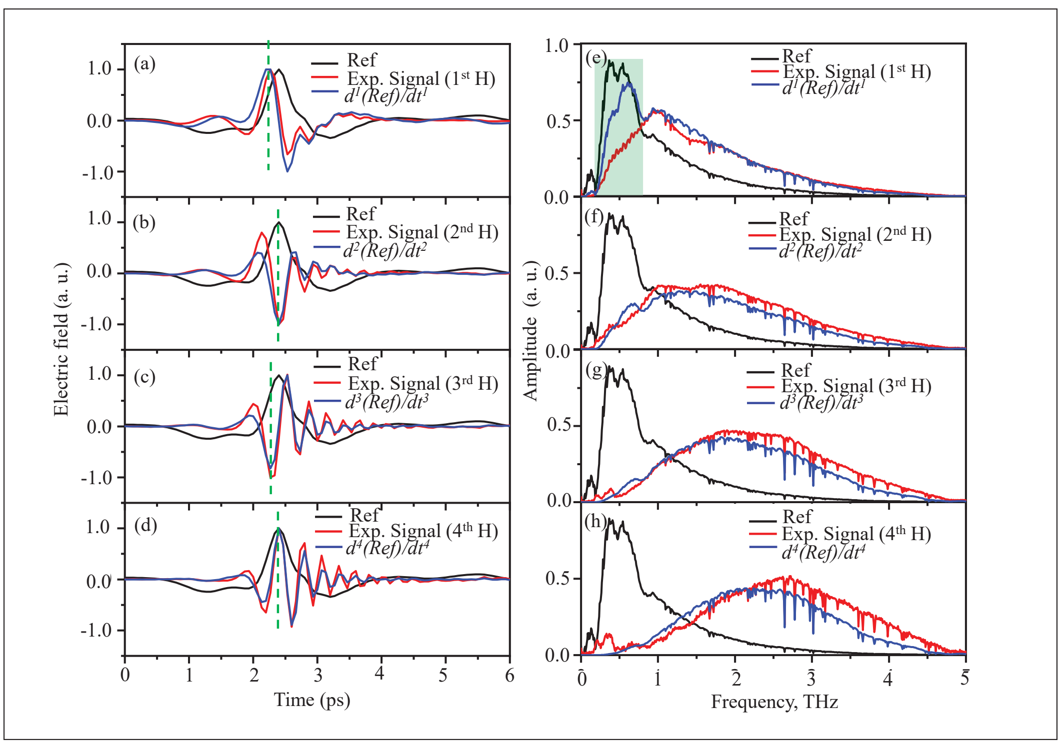

Figure 4.4 The reference signal (black) when the PM device is not operating, the temporal measured THz waves (red) using PM device as a differentiator with lock-in amplifier set to (a)1^{st}, (b) 2^{nd}, (c) 3^{rd} and (d) 4^{th} harmonic measurement and the calculated derivative signal of the reference (blue) which are normalized separately. In (e), (f), (g) and (h) are the corresponding retrieved THz spectra from (a), (b), (c) and (d), respectively

To study the modulation effect of the PM device on the THz signal, the lock-in detection is referenced to the 10.82 kHz excitation frequency obtained using an AC signal generator and the time steps used for all measurements are set to 66 fs. Fig. 4.4 shows the time traces (in red) obtained with the lock-in amplifier and the PM device activated for (a) the first harmonic, (b) second harmonic, (c) third harmonic and (d) fourth harmonic. The black trace represents the reference signal, i.e. the one obtained with the emitter modulated ON and OFF. The traces in blue represent (a) the first derivative, (b) second derivative, (c) third derivative and (d) fourth derivative of the reference signal obtained using the mathematical derivation function. Fig. 4.4 also shows that the signal modulated by the PM device (in red) is slightly different from the one calculated (in blue). This difference is mainly observed for the first (a) and second derivative (b), while a great similarity exists between the experimental and calculated data for the third (c) and fourth derivatives (d). Nevertheless, as shown in Fig.4.4, the slope of the reference signal is recovered by the odd-order derivatives (1^{st} and 3^{rd}), while the peak of the reference signal is found by the even-order derivatives (2^{nd} and 4^{th}), as expected for the derived function.

4.6 Analysis and discussion

As THz measurements are performed on the electric field as a function of time, the FFT allows us to move into the frequency domain to analyze the information in amplitude and phase. Figure 4.4 also shows the normalized amplitude spectra in a linear scale of the reference signal (black curves), and in red the signals derived from (e) first, (f) second, (g) third and (h) fourth order recovered by the PM device. The blue curves represent (e) the first-order, (f) second-order, (g) third-order and (h) fourth-order derived signals calculated from the reference signal. As for the information in the time-domain, there is some difference in the low-frequency part between the calculated and experimental spectra, but mainly for the first-order derivative, see Fig. 4.4 (e). In this figure, as highlighted with green color, it can be seen that frequencies around 0.7 THz are modulated differently from their higher frequency counterpart (i.e., frequencies shorter than 1 THz or wavelengths longer than 300 μm). The increase in the order of the derivatives produces a closer agreement between the experimental information and the calculated derived information, see Fig. 4.4 (f), (g) and (h). These discrepancies between the low and high frequencies of the first derivative signal are partly due to the complex motion of the PM and the wave diffraction principle (Cowley (1995)). Therefore, the spatial distribution is dictated by the diffraction-limited condition at focus and is not uniform with frequency. In other words, only longer wavelengths are reflected from the entire substrate ($2.1x2.1\,mm^2$), in contrast to shorter wavelengths, which are mainly reflected at their center. In this case, it is reasonable to assume that the low-frequency part of the spectrum is more affected by the complex geometry of the device, while the higher frequencies are mainly located in a uniform area, the central part. Moreover, as mentioned previously, the reference signal is taken for a complete reflection on the whole substrate and the whole device simultaneously. However, the modulated signal only comes from the reflection of the moving complex geometry of the device, as shown in Fig.4.12 in the supplementary information. Only this "complex" signal should be used for comparison purposes, as a reference. Unfortunately, this reference information is inaccessible to obtain experimentally with this device. Fortunately, we have to stress that since the derivative function acts as a high-pass filter (Cooper & Cowan (2004)), the transition to higher-order derivative information becomes less sensitive to the complex geometry of the device, or to the discrepancy observed at low frequencies. The shift of the peak position of the spectra towards higher frequencies, up to 2.5 THz for the 4^{th} derivative order, confirms this high-pass filtering effect and is in a very good agreement between the calculated and measured high-order derivatives, see Fig. 4.4 (f), (g) and (h).

To confirm the quality of the derivative measurements, Fig. 4.5 (a) shows the calculated transfer function of the PM device obtained from the integral of the measured first derivative signal over the measured reference signal. The majority of the spectral range, i.e. from 0.8 to 4 THz, shows a flat response while complex variations appear for frequencies below this range. As mentioned earlier, the difference in beam size at the focus position as a function of frequency (Blanchard *et al.* (2013)) accounts for this non-uniform frequency response and can now be viewed as a new spectral response function for this system.

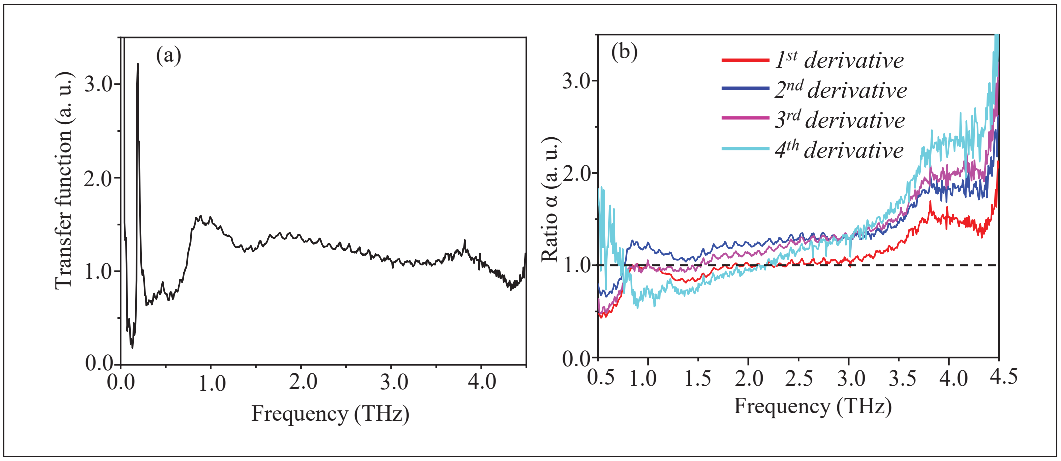

Figure 4.5 Illustration of (a) the transfer function of the PM device and (b) presents the ratio of normalized amplitude between the experimental data and the calculated signal to evaluate the PM device as a THz differentiator for four order derivative measured signals that are first, second, third and four derivatives

In Fig. 4.5 (b), we also show the normalized amplitude between the experimental data and the expected signal, i. e., those calculated from the reference signal. Normalization is expressed by the ratio between the experimental signal and the calculated derivative signal depends on the frequency, called $\alpha(\omega)$, as follows:

$$\alpha(\omega) = \frac{N^{th}\, order\, derivative\, of\, Exp}{\frac{d^N(Ref)}{dt^N}} \tag{4.4}$$

where N is the derivative order, Ref. and Exp. are the reference and experimental modulated THz signal, respectively. In order to qualitatively evaluate the purity of the experimentally derived signals, a ratio α equal or close to 1 would mean perfect agreement. In Fig. 4.5 (b), the results of this calculation show that the ratio α for the frequency range between 0.7 THz to 3.5 THz is almost flat around 1, which clearly indicates a good performance of the PM device with a lock-in amplifier as a THz derivative spectrometer. Only for frequencies below 0.7 THz, the performance of the PM device did not allow accurate recovery of the "readable" original signal. A second indication of the good performance of our THz derivative spectrometer is the achievable signal-to-noise ratio (SNR). In general, derivative spectroscopy has the disadvantage of poor SNR (Singleton & Collier (1956)).

To evaluate if the THz derivative spectroscopy with this method suffers from the same problem, we were interested in comparing the SNR of the original reference signal with those obtained from the derivative measurements. An interesting way to carry out this comparison on a comparable scale is to recover the reference signal from the integration of the measured derivative signals. For example, the integral of the 1st order derivative measurement leads to the reference signal. Similarly, the double integral of the measured signal of the $2^n d$ order derivative also leads to the reference signal, and so on. However, we found that by increasing the number of integration on the signal, the DC component in the generated FFT signal was amplified. As a result, a succession of integral calculations on the higher-order derivative signals introduces a non-negligible offset in the recovered signal. On the other hand, the positive result of the integration is its low-pass filtering action, which nicely eliminates the high-frequency noise level.

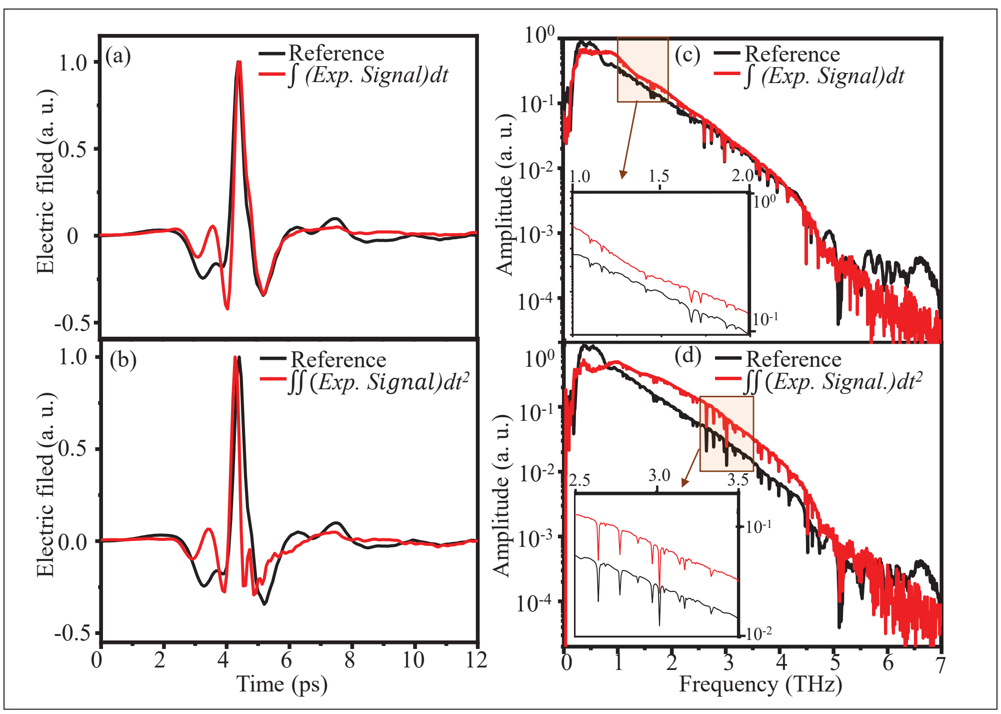

Figure 4.6 Showing (a) and (b) are the integral of the first and second derivative measured signals in the time domain (red) with the reference (black). (c) and (d) show the corresponding spectra of these two signals compared with the reference spectra

Figures 4.6 (a) and (b) show the 1^{st} and 2^{nd} order integration of the detected modulated THz signal in the time domain and (c) and (d) their respective frequency spectra. By way of comparison, the black curves of each figure are the reference signal in the time and frequency domains. For a fair comparison, it is important to note that all scans were done with the same scale and integration time. As expected, the signals of the first-order integral in the time and frequency domain are similar to the measured reference signal, except for the low-frequency part. In Fig. 4.6 (c), we can also see that the SNR between the reference signal and the integrated signal are surprisingly comparable, without any sign of SNR degradation. Even more strikingly, compared to its reference, the double-integrated signal in Fig 4.6 (d) has an order of magnitude better dynamic range in the frequency range of 1 to 3 THz, i.e., in the operational range of the device. To ensure that this setup does not introduce errors for future spectroscopic applications, we show in the insets of Fig.4.6 (c) and (d) a zoomed-in view of the water absorption lines. From these results, it is clear that no negative effect exists on the spectral shape of the water lines, only an increase in signal with respect to the reference spectrum. Therefore, the device can be used for practical THz derivative spectroscopy experiments in the time domain.

4.7 Simulation results

In order to simulate the effect of the PM device on the THz field, we used Lumerical's FDTD (Finite-Difference-Time-Domain) software. As the simulations produce discrete information, the differentiation function must be expressed as an analytical expression in the form of a set of discrete points (see Table S1 for more information) (Gilat (2013)). As detailed in the complementary information S2, we have simulated two configurations of the PM device: first for a uniform displacement such as a plane mirror (see Fig.S2 (a)) and second for a complex angular displacement (see Fig.S2 (b)), closer to the experimental reality of the PM device with a time step of 1 fs. The formula of the central difference approximation of the derivatives was used (Gilat (2013)), see in supplementary information Fig.S3 the discretization of the points according to the position of the simulated structure. This derivative function allows to estimate the derivation from points on both sides of the central point at which the derivative is calculated.

For example: Two-point and three-point central difference formula for the first and second derivative is derived using (Gilat (2013)),

$$f'(d_i) = \frac{f(d_{i+1}) - f(d_{i-1})}{2h} \tag{4.5}$$

$$f''(d_i) = \frac{f(d_{i-1}) - 2f(d_i) + f(d_{i+1})}{h^2} \tag{4.6}$$

where h is the difference between the points in time, d_i is the central point of origin, while d_{i+1} and d_{i-1} are lateral points as displacements of the device, for example ±6.33 μm for a round trip of 12.66 μm. The simulation results for the differentiation of orders 1, 2, 3 and 4 are presented in Fig. S4 and Fig. 4.7, with (a) the reflection on a flat surface and (b) on a complex surface.

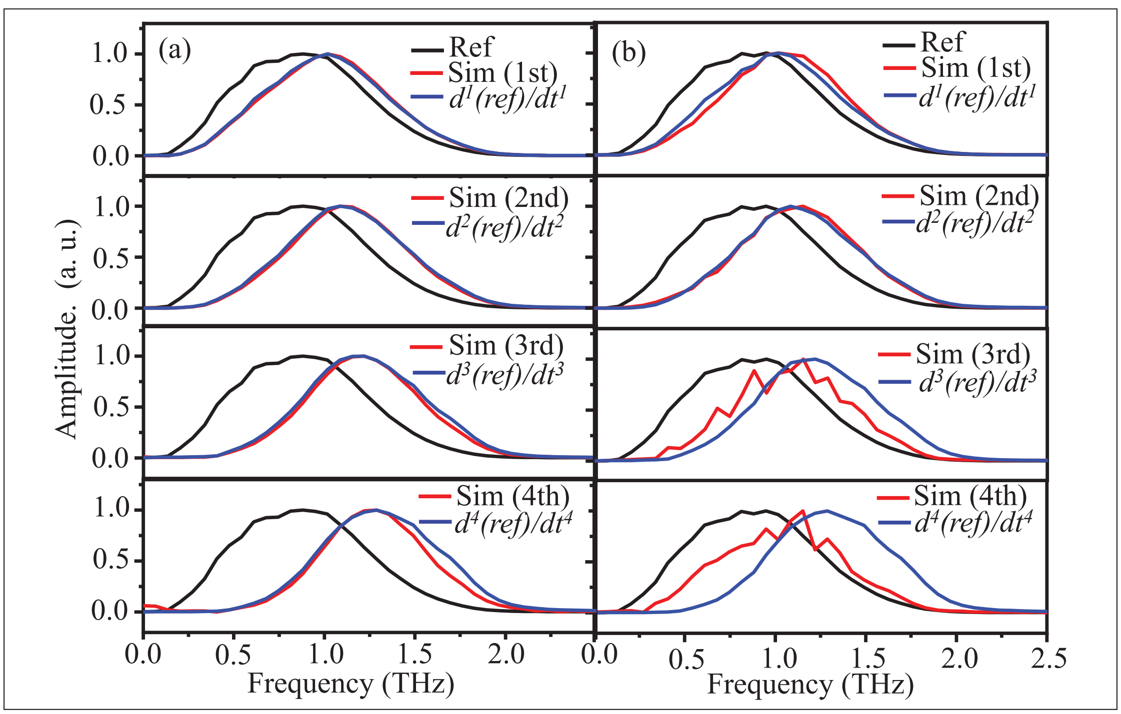

Figure 4.7 Comparison of the frequency spectras reference, differentiated by FDTD and calculated one, (a) obtained from the time domain traces for a uniform displacement while (b) are obtained with an angular displacement. (see supplementary info).

A perfect agreement is found using simulation from a flat mirror. In contrast, the simulations for the complex geometry produce a significant reading error. We attribute this discrepancy to the fact that the simulations are performed with discrete points and the background signal from the stationary parts of the device is orders of magnitude larger than the simulated changes, which could not be resolved.

In the simulations, we also compared the spectrum of the THz signal reflected from all elements of the PM device with the spectrum of the signal reflected only from the moving parts of the device (see Fig. S5). It is interesting to note, as shown in Fig. 4.5 (e), that a clear difference in the range of 0.1 THz to 0.7 THz appeared between the reference signal reflected from the complete device and that of the moving part only. In light of this finding, it is reasonable to assume that the main difference between the measured derivative signals and those calculated from the reference is due to the complex structure of our device.

4.8 Conclusion

Using a large aperture PM device, we have investigated a simple strategy to convert the traditional THz-TDS system into a derivative THz spectrometer. Our results confirm that the THz signal modulated by the PM device provides access to the nth-order derivation of THz pulses. We have experimentally demonstrated up to the $4^t h$ derivative and found good agreement with the expected derivative information of the reference signal. Moreover, after the integration of the nth-order derivative signal, the recovered information shows an increase of the SNR compared to its reference signal. This demonstration could be very useful for fine THz spectroscopy where the phase changes on a signal is the critical parameter to improve. In the near future, this differentiator can be implemented as a two-dimensional uniform motion matrix that would allow the development of new methods for computational imaging and advanced manipulation of THz pulses.

4.9 Acknowledgment

F.B. gratefully acknowledges financial support from NSERC (grant number 2016-05020), FRQNT and Canada Research Chair in THz technology. F.N. acknowledges financial support from NSERC (grant number 2016-04871). The authors would like to thank CMC Microsystems for providing the tools enabling design and fabrication of the PM device.

4.10 Supplementary information

4.10.1 Lock-in amplifier:

Lock-in amplifiers are essential to measure a weak signal within a noisy background. A lock-in amplifier is a system which selectively amplifies this signal at a given reference frequency. Fig.4.8 shows the input signal, V_{in}, which is multiplied by a reference wave, V_{ref}, at reference frequency which modulates the input signal. Then, after applying a low-pass filter (LPF), the final result is a DC signal, which is the signal of interest to measure (Kloos (2018)).

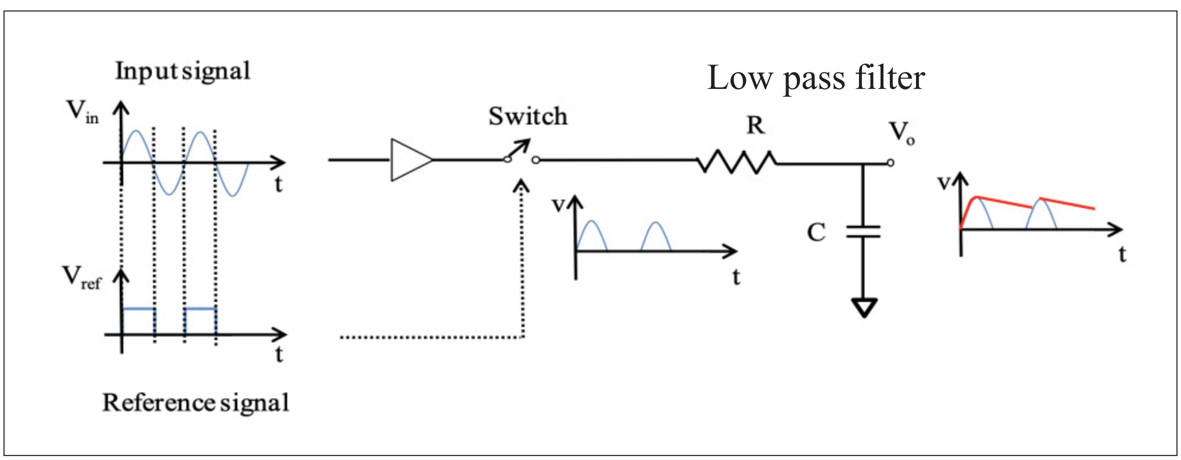

Figure 4.8 The simplified chain of elements constituting a lock-in amplifier

In our experiments, we used an SR865A lock-in amplifier from Stanford research. The input signal is a sinusoidal signal with a frequency of f_{mod}, at 10.82 kHz. In general, the low LPF period is always fixed to $1/f_{mode}$, regardless of the harmonic order to be detected (i.e. N as a harmonic number on the lock-in amplifier) in the operation of the lock-in amplifier (Kloos (2018)).The output signal will be averaged over N periods of the detected frequency. Then the lock-in is able to detect signals at harmonics order of the frequency of the reference signal. Simply, the lock-in multiplies the input signal with a digital sine wave with a frequency of N$\times f_{mod}$. Therefore, only input signals at this, Nth harmonics order, will be detected. Consequently, the other signal is not detected. In order to describe the performance of the PM device in combination with lock detection, the relationship between the moving parts of the PM device and lock detection must be explained. In this context, it is important to understand two things: (i) how the lock-in amplifier reads "device position" and (ii) how the harmonic function operates according to this first description. In our case, the lock-in reference signal is a fixed sine wave that drives the PM device, called the modulation frequency f_{mod}, or modulation angular frequency Ω_{mod}. The angular frequency Ω_{mod} of the reference signal is changed based on the selection of the number of harmonics in the lock-in, N. Therefore, for the first harmonic measurement, f_{mod} is $2\pi f_{mod}$. The angular frequencies for the second, third, and fourth harmonic measurements are $4\pi f_{mod}$, $6\pi f_{mod}$, and $8\pi f_{mod}$, respectively. This means that to measure the first derivative of the THz beam, the lock-in detects the differential THz signal of two positions of the moving part of the PM device during a period of one cycle from 0 to 2π. By increasing the harmonic order N, the lock-in amplifier detects the signal at N times the referenced signal. Therefore, it will have N times more stop position of the PM device to read the THz field amplitude and thus N times a subdivision of the differential optical path leading to the measurement of the N-order derivative function of the THz waveform. These subdivisions are carried over periods of 4π, 6π and 8π, corresponding to the 2^{nd}, 3^{rd} and 4^{th} harmonics, respectively.

As an example, the relationship between the motion and the lock-in detection phase as function of the Nth order derivative of one part of the PM device is shown in Fig.2 of the main article for the green wings (see at the top of these figures). As mentioned in the article, in Fig.2(a), (b), (c) and (d) the value of displacement with its corresponding phase value are shown for each Nth order derivative function. For measurement of the second derivative signal, as the harmonic N increases to 2, the angular frequency, Ω_{mod}, of the reference signal for Lock-in detection will be $2\ \pi(2f_{mod})$, resulting in detection over two distinct displacement regions, i.e., +6.33 μm to 0 and 0 to -6.33 μm also corresponding to the 0 to 2π and 2π to 4π phases. These subdivisions in displacements of the device and the corresponding phases according to the order of the harmonics N increase accordingly, see (c) and (d) in this figure for the 3^{rd} and 4^{th} harmonics, respectively. In light of this explanation, it is important to note that in the experimental measurement, the derived information obtained from the incoming THz signal results from the combination of the complex movements of each part of the PM device, i.e., green and yellow wings as well as grey central part displacements.

4.10.2 Simulation study of PM device:

In order to simulate the effect of the PM device motions on the THz field, we used the Finite-Difference-Time-Domain (FDTD) software from Lumerical. As the simulations produce discrete information, we used the differentiation function to calculate numerically the N^{th} order derivative that is expressed as an analytical expression in the form of a sets of discrete points (Gilat (2013)). We first simulated the response of the PM device for discreet displacement points in the FDTD simulation and then we calculated the Nth order derivative of corresponding data from simulation using the numerical differentiation function.

Table 4.1 The finite central difference formulas for numerically calculating the first-, second-, third-, and fourth-order derivatives, where h is the time interval difference between points, d_i is the center point of origin, and d_{i+x} is the displacement for each device motion

Derivative order	Definition	Eq.	set of points
1st	$f'(d_i) = \frac{f(d_{i+1})-f(d_{i-1})}{2h}$	(S1)	two
2nd	$f''(d_i) = \frac{f(d_{i-1})-2f(d_i)+f(d_{i+1})}{h^2}$	(S2)	three
3rd	$f'''(d_i) = \frac{f(d_{i-3})-8f(d_{i-2})+13f(d_{i-1})-13f(d_{i+1})+8f(d_{i+2}-f(d_{i+3})}{8h^3}$	(S3)	six
4th	$f''''(d_i) = \frac{f(d_{i-2})-4f(d_{i-1})-6f(d_i)-4f(d_{i+1})+f(d_{i+2})}{h^4}$	(S4)	five

Table 4.1 shows the formula of the central difference approximation of the derivatives (Gilat (2013)) that we used to calculate the first-, second, third, and fourth-order derivatives from

simulation data using various set of discrete data d_i. The discrete points are considered for all displacements from every moving part of the device (green, gray and yellow parts) as shown in Fig 2 (c) in the main article. These functions allow to calculating and estimating the derivation from points on both sides (e.g. d_{i+1} and d_{i-1}) of the central point. It is important to mention that the values of both sides from the central point should be equal as well as they should have the same distance from each other.

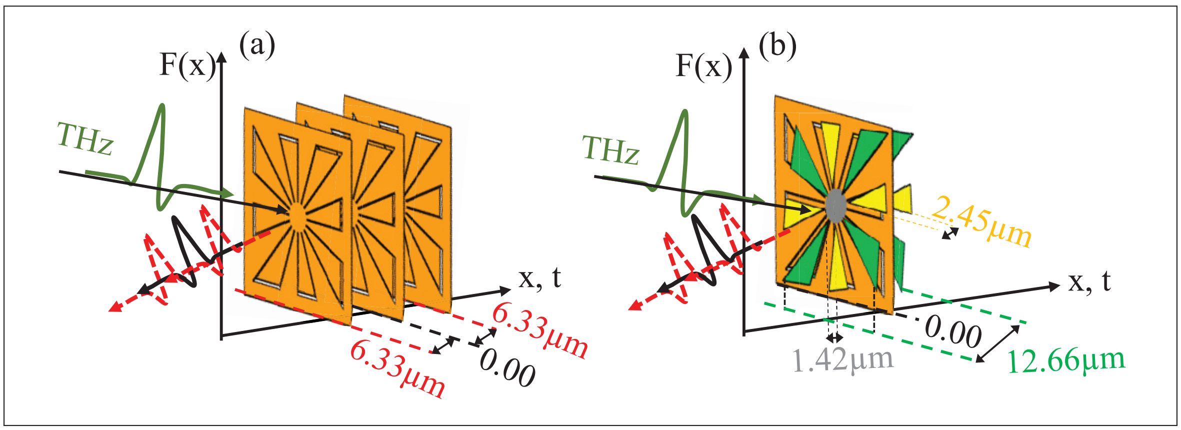

Figure 4.9 Illustration of a silicon layer of the PM device design in the FDTD simulation with (a) a planar surface with uniform displacements and (b) an angular surface with complex displacements for three parts of this layer

In Fig.4.9, we have simulated two configurations of the device: (a) for a uniform displacement of the entire structure and (b) with a complex angular motion of the different moving parts of the device. In the simulation, the incoming THz beam is assumed to be Gaussian with a central frequency of 0.83 THz and a bandwidth of 2.5 THz. Finally, the incident beam impinges normal to the surface of the PM device and then the reflected THz signal is recorded by a monitor. In (a), the entire device undergoes a round-trip motion of $\pm 6.33\ \mu m$. In (b), the green and yellow wings and the central part of the PM device undergo a motion of 12.66 μm, 2.45 μm, and 1.42 μm, respectively.

To better understand how to use the numerical differentiation function for the flat surface, Fig.4.10 shows a set of (a) two, (b) three, (c) six, and (d) five discrete simulation conditions.

The positions chosen correspond to the data needed to compute the finite central difference formulas for recovering the first-, second-, third-, and fourth-order derivative of the THz signal, respectively. For example, Fig.4.10 (e) illustrates how to position the device at a set of three locations in the simulation to obtain the second-order derivative of the THz signal from the motion by using Eq.(S2) in table 4.1.

The temporal derivative traces obtained by simulations are shown in Fig.4.11 with (a) the reflection on a flat surface with uniform displacements and (b) on an angular surface with complex displacements. The subfigures show the 4 signals derived from the simulation data using the numerical differentiation function (in red) and from the simulated THz reference signal using the derivation function (in blue). An excellent match is obtained between the simulation results and the calculation from the reference signal when the PM device acts as a flat surface with uniform displacements. In (b), when the PM device operates with complex angular motions, we observed a very good agreement for the 1^{st} and 2^{nd} order derivatives with the calculations.

However, the simulations of the 3^{rd} and 4^{th} order derivatives produce a significant difference to the response of the calculations of these same derivatives. We translate this difference into the fact that the numerical method uses simulation data with discrete points and the signal reflected from the non-moving parts of the device has a magnitude that far exceeds the signal reflected from the moving parts of the device.

4.10.3 Difference between measurement and calculation of derivatives:

To explain the discrepancy between the experimental and calculated derived THz signal, as shown in Fig. 4(e) in the main article, we compared the THz signal reflected from all elements of the PM device and that reflected from the moving parts of the PM device, i.e. by FDTD simulation. Fig.4.12(a) shows the spectra of the reflected THz signals from these two cases. It is clear that the amplitude of the signal reflected by all the elements (blue curves) is greater than that of the signal reflected by only three parts (red curve) of the device, which is explained by

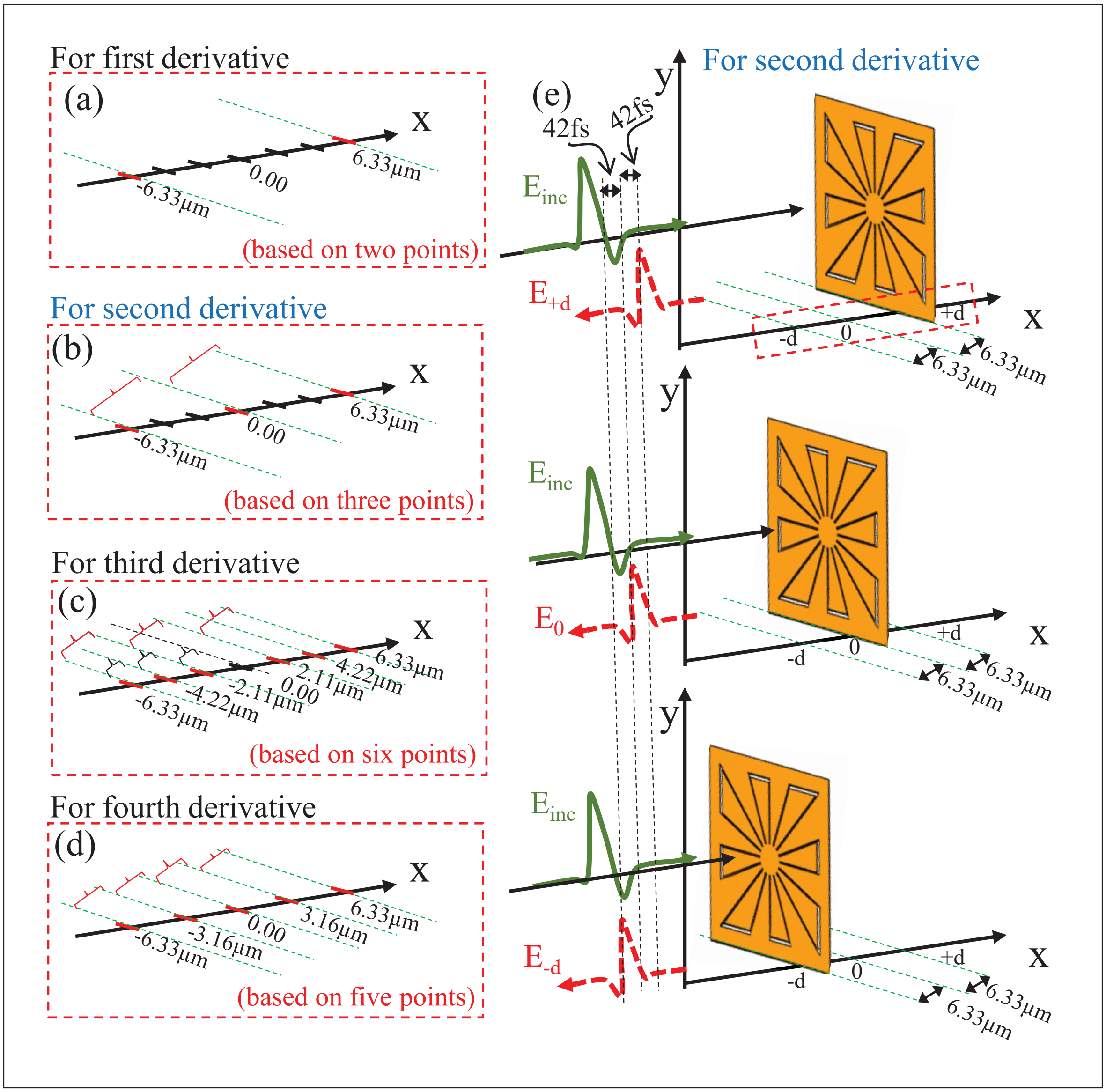

Figure 4.10 Illustration of the numerical method with a set of discrete points for a flat surface with a uniform motion of the silicon layer of the PM device to calculate the first (a), second (b), third (c), and fourth (d) derivatives of the THz signal. (e) Example of using the method in the simulation with a set of two points to calculate the second derivative of the THz signal at the zero point

the smaller surface covered by the moving parts of the device.

More interestingly, in Fig.4.12(b), the normalization between the two spectra reveals a significant shift for frequencies below 0.7 THz, as was also observed experimentally in Fig. 4(e) in the main

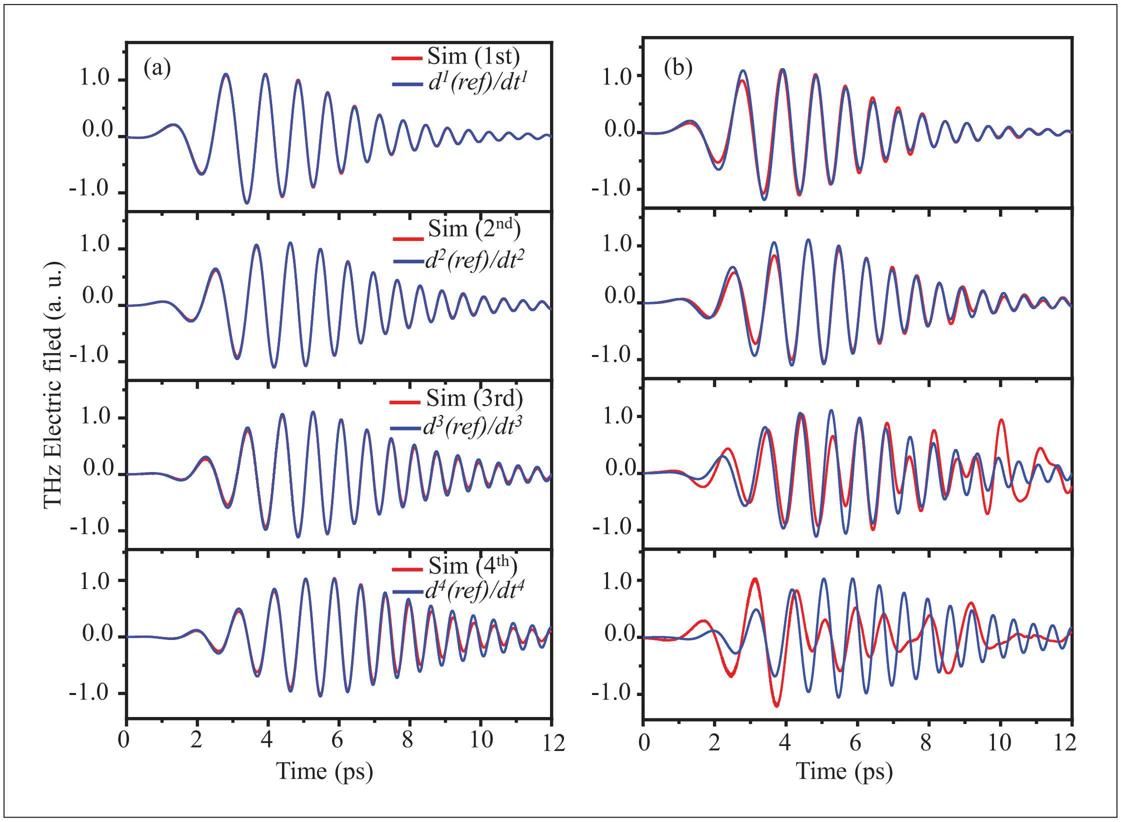

Figure 4.11 Showing the simulation results of two PM device configurations (a) obtained from a flat surface and (b) with a complex angular surface. The time traces of the FDTD-simulated differentiation were calculated from the reference signal for the first-, second-, third-, and fourth-order derivatives

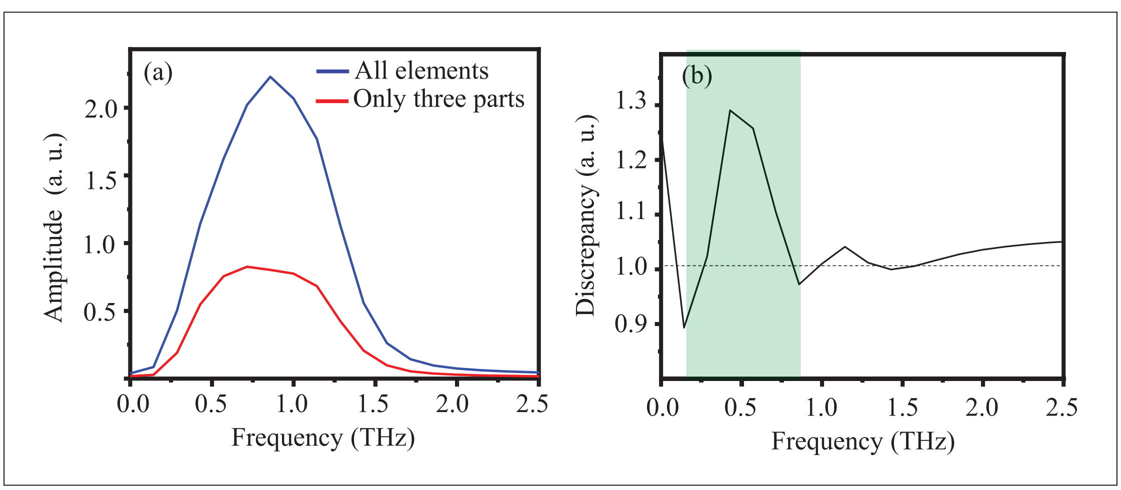

Figure 4.12 Illustrations of (a) the spectra simulated from the reflection of the signal on all the elements of the device and that reflected by the three mobile parts of the silicon layer and (b) normalization between these two spectra

article. Therefore, we suggest that the main difference between the experimental and calculated results comes from the way we measured our reference spectrum. This result is important because it also suggests the importance of using a uniform moving structure to accurately realize the derived function over a wide range of frequencies.

CONCLUSION AND RECOMMENDATIONS

Conclusion

THz sensing technology is a rapidly growing field. Terahertz time domain spectroscopy (THz-TDS) is an excellent tool for THz sensing because it allows the characterization of matter in novel ways using characteristics of THz radiation. Although, significant technical advances have been made over the past three decades to enable more efficient THz sensing and imaging, much improvement is still needed in sources and detectors in order to transform THz spectroscopy and imaging from a tool in laboratory settings to a flexible instrument with practical real-world applications. Many researchers are currently working on developing better performing THz sources and detectors with advanced features, which often include the use of new materials, processes, and techniques, to improve THz sensing technology. Following this line of research, the ultimate goal of this research project is to focus on creating innovative ways to improve THz detection.

The first contribution of this PhD research is the development of a new method for characterizing the electro-optic (EO) properties of a thin-film material based on intense THz near-field microscopy, as developed by Blanchard *et al.* (2013), where the THz electric field of a split-ring resonator (SRR) can be mapped using EO detection by a Lithium Niobate (LN) thin-film placed under the SRR. More specifically, we propose probing the unknown EO properties of a thin-film by probing the near-field response of an arrangement of SRRs with different orientations with respect to the main axis of the EO thin-film material. Therefore, as a proof of principle, we apply this method to an LN thin-film. For this purpose, we design an SRR for the THz frequency and use finite-difference time-domain simulation (FDTD) to study its field distribution. In order to access the response of the SRR in all orientations of the thin-film, we also study and analyze all the field distributions of the SRR using different applied THz field polarizations. Then, to show the validity of our simulation results, we use the same designed SRR with different orientations for the experimental work and place it on top of a well-known LN thin-film crystal, which is the $X-cut$ crystal in the experimental setup shown in Chapter 2.

As near-field THz imaging methods have been used as a powerful method to map the electric field distribution of metamaterial structures in a non-contact approach, we used this method, which can be located in the detection of the THz-TDS system, to observe the SRR response. We find a very good agreement between our simulation and the experimental results. To characterize and find the sensitivity of the EO crystal in all orientations, we also analytically study the LN crystal and show how the sensitivity of this thin-film crystal can be obtained as a function of the applied THz electric fields and probe beam polarizations. Indeed, the analytical results demonstrate how to calculate all the elements of the EO coefficient tensor of an $X-cut$ LN crystal as a function of THz pulse and probe beam polarization. As a result, we should be able to describe an unknown material using the technique provided here, with the same SRR structure that is patterned on it. In other words, using this technique can lead to improvement in THz sensing technology, and we should be able to recover the EO components of an unknown material on the basis of our provided LN characterization, which allows us to find a thin-film material with better performance.

This unique developed method of proposed EO thin-film characterization using non-contact electrodes provides a suitable way to explore the characteristics of EO thin-films for other wavelength ranges as well, for example, from 512 nm to 850 nm. The theoretical and numerical simulation results presented in this work could assist enhance the understanding of future researchers in further exploring similar metamaterial design candidates for material characterization and finding EO properties. In addition, for sensing applications, these analytical and theoretical studies can help in selecting the orientation of a crystal as well as an appropriate polarization for the probe beam to obtain a better response for using this crystal in THz detection and generation. Finally, as the SRR structure has a magnetic response, this approach could be used to characterize new magneto-optical materials.

The second contribution of this thesis is the development of a simple approach for actively modulating THz waves in reflection mode. This method is based on utilizing a piezoelectric micromachined transducer (PMUT) array with a lock-in amplifier, resulting in a differentiator. We report this method, which performed a first-order time-domain differentiation of broadband THz pulses using a PMUT array. This array can be electrically driven to induce displacement translations on the array elements at around 100 nm. These particularly small spatial translations induce tiny variations in the optical path of an impinging THz beam, which in turn dynamically changes the arrival time of the THz pulse to the detector. This modulator allows the time derivative of the THz pulse reflected from its surface, providing an output proportional to the input's derivative. In real time, we tested this device in the THz-TDS system, and it yields time-derived THz wave. This device operates based on the piezoelectric effect, which is mainly employed as an ultrasonic transducer (Robichaud *et al.* (2018b)). We placed this device in the THz path of the THz-TDS system, where the THz pulse is modulated on a femtosecond (fs) scale. Because lock-in amplifiers in the THz-TDS system use a method known as phase-sensitive detection to identify the component of the signal at a specific reference frequency and phase, we can measure the differentiation of two THz pulses with a variation of fs time while lock-in referenced to the resonant frequency of this device. We have proven theoretically and experimentally the concept of active THz time derivative measurement using the PMUT array in this work. We show a very good agreement between the calculation and the measured signal where the modulated THz signal detected after the piezoelectric device is proportional to the first-order derivative of the THz pulse. We also show the limitation of this method, which results from the tiny size (i.e. 200μm) and limited movement range (100 nm) of the unit cell of this array relative to the propagation THz path. Because of this limitation, the technique was restricted to the first-order derivative. Furthermore, we had to employ a voltage driver with a

MHz oscillator to maintain the resonance frequency of the PMUT array, which made its use for the lock-in amplifier less straightforward. This study allows the concept of using this device as a THz modulator to expand the knowledge required to select this device for better performance by presenting its characteristics and performance as well as describing the device's limits as a THz time modulator.

Finally, as the third contribution of this research effort, we have improved the previously presented approach (second contribution) by employing a new device, i.e. a piezoelectric micromachined (PM) (Gratuze *et al.* (2019)) device with a higher motion range and larger size relative to the THz beam. As a consequence, we can suggest a simple approach for converting a standard THz-TDS system into a derivative THz spectrometer utilizing the PM device. We evaluated the PM device on a standard THz-TDS system to measure directly the time-domain derivative (i.e.: up to fourth-order derivatives) of the THz wave. We characterize how the THz derivative wave is measured using this device in comparison to a reference wave and its numerical derivatives. To do this, we theoretically calculated the derivative of the THz reference signal as measured when the device acts as a mirror. Then, by using differentiated functions, we prove the validity of the fourth-order derivative of THz signals. In addition, we employed FDTD to study numerically THz differentiation by placing the PM device as a mirror at discrete points relative to the displacements of the PM device. Even though this device worked very well to provide THz derivative signals, there was a slight disagreement between the experimental result and the calculated one from the reference signal in the low-frequency range below 0.7 THz. Therefore, we investigated the response from the device using the simulation to detect reasons for the disagreement at these low frequencies. We also illustrate the comparison by the ratio between the measured derivatives and those calculated from the reference signal. This comparison reveals how this device works as a function of THz frequency, relatively. This also shows the spectral range of the ratios ranging from 0.7 to 3.5 THz.

Furthermore, after the integration of the first- and second-order derived signals, the recovered information shows an increase in SNR compared to the reference signal. Therefore, these examples can potentially be very useful in sensitive THz spectroscopy, where phase variations in a signal are the most essential feature to improve. We calculated the PM device transfer function, which is derived by integrating the measured first derivative signal over the observed reference signal. This transfer function shows that this device has a flat response in the spectral range from 0.8 to 4 THz but no flat response for frequencies below this range. We attribute this to the variation in beam size as a function of frequency (Blanchard *et al.* (2013)) compensating for this non-uniform frequency response. Additionally, the response of this device may be regarded as a new spectral response function for the THz-TDS system.

Ultimately, although many unanswered questions remain in this thesis, this is not particularly surprising since we have focused on only a few aspects of a very broad topic. In the following section, we conclude by highlighting some unresolved questions that may be addressed in the future.

Recommendations for future work

We propose here some suggestions for improving of the methods developed in this thesis, followed by their possible application to extend the research covered by this thesis.

Characterization of EO thin-film materials and their future applications

The development of the EO thin-film characterization using THz near field microscopy reveals EO responses in the x-, y-, and z-directions of thin-film materials. In the case of the experimental demonstration and SRR design, there are some suggestions for future work to improve and expand the method developed here. We listed them below as follows:

1) We designed an SRR for 0.5 THz to characterize EO thin-film materials whereby their all-electric and magnetic near field distribution are studied using FDTD simulation. These simulation results can be considered reference responses from this particular SRR. Since the SRR structure also exhibits a magnetic response (see Figure. 2.1), as shown in Chapter 2, this method could be extended to characterize novel magneto-optic (MO) materials. This indicates that this SRR structure can be used to study the magnetic response of well-known thin-film MO materials in an experimental setting, potentially providing a new approach to characterizing unknown MO thin-films.

2) In addition to this, to investigate the EO response in a THz frequency range different from 0.5 THz, one can change the SRR dimension and its gap size to access other THz frequencies to characterize the EO thin-film. The equation for SRR design is provided in the literature review section in Chapter 1.

3) Fabricating an SRR on materials might be difficult for each material characterization using our method. We therefore recommend that, in future, an SRR be fabricated on a silicon wafer, which can be utilized for multiple material characterizations by putting it on top of each material sample using our approach.

4) To improve the experimental data, a modification is required for the SRR sample. We recommend the increase of distance between the 45-degree SRR and the other excised SRRs in the design of the SRR sample. Because, in our fabricated SRR sample (see Fig.2.1(b)), the distance between the 45-degree SRR and the other excised SRRs appears to be insufficient, this caused a different mutual coupling in the enhanced field (showing a larger Q factor) observation for this SRR angle, which differs somewhat from the numerical study (see 2.6 (b) and (b) in Chapter 2).

5) To extend this method beyond the 800 nm wavelength to characterize EO thin-films with other optical beams, it is possible to study and examine the characterization of EO thin-films with other optical beam wavelength ranges (e.g., 512 nm to 850 nm) while using the same SRR. This is because the THz electric field acts as an electric field applied to the EO material to characterize the thin-film. Doing this will allow the extension of this method to other applications related to sensing, integrated electro-optics and communication.

6) To examine the influence of polarization on the sensitivity of the EO material, it is essential to test experimentally a thin-film with varying THz and probe beam polarizations. Then, the resulting experimental data need to be compared to the modeling and analysis results to determine the accuracy of this study, which will provide a working knowledge of the influence of beams and THz polarization on the orientation of the EO thin-film.

Characterization of EO thin-films not only provides a highly sensitive EO crystal for THz sensitivity applications, but is also very useful for higher speed, lower cost integrated optical devices and communications. Indeed, the design of a new generation of high-speed photonic modulators would require new materials with high Pockels coefficients, which would allow for a faster response and a wider bandwidth. On the other hand, EO thin-films can be bonded to a variety of substrates (see references Weigel, Zhao, Fang, Al-Rubaye, Trotter, Hood, Mudrick, Dallo, Pomerene, Starbuck et al. (2018); Zhang, Wang, Kharel, Zhu & Lončar (2021b)) and their fabrication is more compact than bulk EO modulator platforms. Therefore, they can be used as EO modulators and tunable EO filters in telecommunications, as optical switches, and as waveguide modulators for high-speed integrated optical devices.

Derivation of THz wave by PMUT array and possible future applications

The study of a time-domain THz differentiator using a piezoelectric micromachined ultrasonic transducer array (PMUT) demonstrates the idea of measuring the phase-modulated THz signal after the PMUT array in a THz-TDS system. In fact, this device works as a phase (femtosecond time) modulator combined with a lock-in amplifier to provide a THz-time derivative signal that could be useful in THz applications, including information processing, spectroscopy, and imaging. Differentiators are highly anticipated for the future of data transmission in THz telecommunications. However, this work is still based on laboratory instruments that need to be developed for industrial work. For example, we used a lock-in amplifier to measure the differentiation of THz signals that are delayed in time by the PMUT array. For telecommunications applications, a lock-in amplifier must be developed as a simple device to differentiate these two signals at the resonant frequency of the PMUT array device. Other than this, differentiators are a type of high-pass filter. The derivation of a THz signal could be interesting for THz spectroscopy applications as well because a derivative THz signal provides access to spectral information at high frequencies. It allows us to quickly identify the rate of change of the THz signal, which could be particularly interesting for the identification of nonlinear processes in the THz band: (Salén *et al.* (2019)). However, due to the PMUT array device's motion and small unit cell size, the PMUT array has several limitations, allowing only the first-order derived signal of the THz signal to be measured.

Since the potential of microelectromechanical devices to manipulate and control THz waves has been demonstrated we have studied and proven the limitations of the method both experimentally and mathematically. Therefore, we recommend that appropriate microelectromechanical devices with larger unit cells and appropriate motion be selected and designed. Furthermore, we recommend using a device that will be able to work with a kHz oscillator that makes it easier to use with the lock-in amplifier. We also suggest a sampling rate of the data collection in which, to avoid losing the high-frequency component of the THz information, phase shifts that are at least two times smaller than the sampling timing should be considered. This would satisfy the Nyquist theorem. The proposed methodology using the PMUT array device is able to support a wide range of THz applications, from edge detection for imaging to peak detection techniques for telecommunications systems, in addition to developing the sensitivity of THz spectroscopy methods. Furthermore, as it is a matrix modulator in which each transducer is electronically controllable, the development of new spatio-temporal computational information retrieval in the THz frequency range is highly anticipated.

From our suggestion to use a microelectromechanical device with bigger dimensions and movements to increase sensitivity, which also functions at a lower frequency, we found a device (i.e. the PM device) (Gratuze *et al.* (2019)) that was ready to be used for our next step in this project to develop our suggested method.

THz time derivative spectrometer using the PM device and its future applications

We used the large aperture PM device with a simple strategy to convert the traditional THz-TDS system into a derivative THz spectrometer. Our findings show that the THz signal modulated by the PM device allows up to the 4th order of THz pulse derivation. Following these observations, the recovered information indicates an increase in SNR relative to the reference signal. This example may be particularly beneficial in precise THz spectroscopy, where the phase changes in a signal are a key parameter to optimize. Therefore, one of the recommendations for future work would be the design of this device with uniform motion to remove the disagreement in the low-frequency range of performance of the PM device that is under 0.7 THz, as shown in Figure 4.5 and highlighted within the spectral range in Figure 4.4 (b). These discrepancies between the low and high frequencies of the first derivative signal are due in part to the complex motion of the PM and the wave diffraction principle (Padilla *et al.* (2006)). Therefore, the spatial distribution is dictated by the diffraction-limited condition. In addition to this, we suggest that this differentiator can be implemented as a two-dimensional uniform motion matrix in the near future, that would allow for the development of this novel approach for THz imaging processing and advanced THz pulse modulation.

The THz derivative spectrometer might be one of the advanced new spectroscopy techniques based on the so-called derivative THz time-varying signal originally generated from a zero-order reference. Derivatization of the zero-order signal can result in the separation of overlapping signals as well as the removal of noise produced by the presence of other chemicals or materials in a sample. Because of these characteristics, it is possible to quantify one or several analyses without first separating or purifying the sample. Therefore, our suggested approach could become a highly valuable supplementary instrument that helps to resolve various analytical problems. The basic characteristic of the derivation of a THz signal is that it helps identify the slope of the THz signal and the position of the peaks and this could be helpful for sensitive spectroscopic applications, particularly with time-varying signals such as those of radar applications (Skolnik (1962)), spectroscopy and imaging. As a result, one of the most important advantages of utilizing the PM device is its ability to detect accurately fixed points such as local maxima and minima, in real time. In the work of Redo-Sanchez *et al.* (2016), using this device might have great potential to enhance layer detection accuracy. Another potential application of this device, in reference to Blanchard *et al.* (2014b), would be to show the change in refractive indices for THz phase-contrast imaging.

For example, for sensing purposes, Redo-Sanchez *et al.* (2016) were motivated to use the Probabilistic Pulse Extraction (PPEX) algorithm which calculates the probability of each point of an extremal value (i.e. obtained by maths logic) in the signal according to the amplitude, first derivative (for velocity), and statistical characteristics of the noise in the signal because the edge detection methods can suffer from sensitivity to noise. The reason they chose this method was that it uses a distinct filtering process to distinguish the signal from the noise. PPEX actually uses the amplitude and velocity histograms to create a probability distribution for both amplitude and velocity. It calculates the combined probability of a point being external on the basis of such a probability distribution. PPEX, however, does not indicate which candidates match which peaks. According to experimental and modeling data, candidates tend to cluster around a genuine pulse peak. To match the candidates to distinct peaks, Redo-Sanchez *et al.* (2016) utilized k-means clustering.

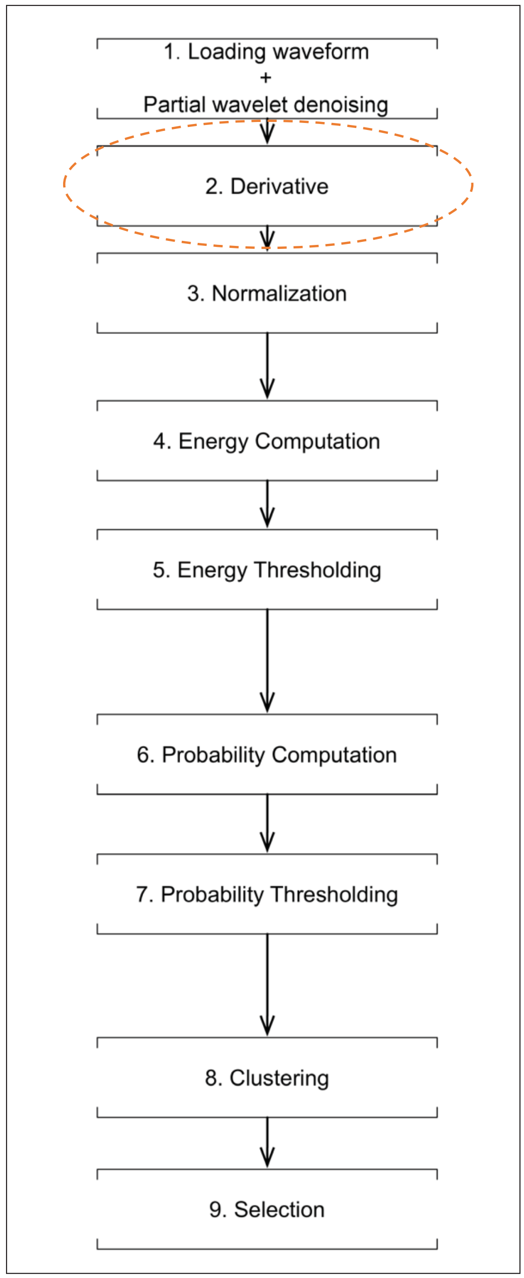

Figure 5.1 (a) Showing the PPEX algorithm flow
Taken from Redo-Sanchez *et al.* (2016)

In Redo-Sanchez *et al.* (2016) work, the derivation function is in the PPEX algorithm flow for image processing as described in the supplementary figure 2 (a) (see Figure 5.1) of this article. In particular, in the second process of calculating the slope of the signal by the histogram of the combination of the amplitude and velocity, they define a probability distribution for both amplitude and velocity. In the next process, they indicate that candidates tend to the group around a real peak of the pulse. However, this is a long process, in which a derivation of the signal is able to identify in real-time fixed points, such as local maxima and minima, with better accuracy to enhance the layer detection accuracy (Redo-Sanchez *et al.* (2016)). We believe that our developed method of using PM devices might have great potential for use in this sensing application without using the algorithm to identify the real peak of the signal. Redo-Sanchez *et al.* (2016) digitally differentiated a signal that directly emphasizes the high-frequency noise. The reason is that when dealing with discrete measurements digitally, differentiating a signal directly emphasizes the high-frequency noise. Since in their method, EO sampling and balanced detection are used for THz detection, we suggest that the use of our PM device, which can optimize detection of the derived signal in an analog way without adding noise. Thus, any unwanted signal is removed by lock-in detection while preserving the differentiated information. The integration of a discrete signal results in a reduction of the noise level, while highlighting the low-frequency information. This is exactly what we are looking for in THz measurements (i.e., an analog differentiation followed by a digital integration).

Another suggestion for future research could be to make a new 2D PM device for 2D derivative measurements using the compressive sensing algorithm. The gain in SNR offered by the integration of the derivative measurements would be very useful in this type of application where a low SNR is often associated with 2D measurements.

STATEMENT OF ORIGINAL CONTRIBUTION

The original contributions to the research described in this thesis are summarized below:

1. Development of a new technique to characterize a thin film electro-optical material using THz near-field microscopy with a non-contact electrode (SRR).
2. Development of a new method by testing a piezoelectric micromachined ultrasonic transducer (PMUT) array to prove the concept of THz wave differentiation and obtain a first-order THz derived signal.
3. Improvement of the THz differentiation method up to the 4th order derived THz signal by testing another device, which is a micromachined piezoelectric device (PM), with different properties such as large aperture and motion, and with the contribution of the lock-in amplifier.
4. A patent is pending for the method of modulating a terahertz signal to obtain a derivative THz wave utilizing the PMUT array.

These contributions were published in different categories, which are indicated in the next section.

LIST OF PUBLICATIONS

During the course of this doctorate, several academic achievements were made. These have been separated into three distinct categories: patent, refereed journal articles, and refereed internal and international conference papers. They are presented below.

Patent:

Amirkhan, F., Robichaud, A., Nabki, F., & Blanchard, F. filed on 23 March (2020). Terahertz Modulation System and Method of Modulating a Terahertz Signal. United States Provisional Patent, 62/993.

Refereed journal articles:

Amirkhan, F., Gratuze, M., Ropagnol, X., Ozaki, T., Nabki, F., & Blanchard, F. (2021). Terahertz time-domain derivative spectrometer using a large-aperture piezoelectric micromachined device. Optics Express, 29(14), 22096-22107.

Amirkhan, F., Robichaud, A., Ropagnol, X., Gratuze, M., Ozaki, T., Nabki, F., & Blanchard, F. (2020). Active terahertz time differentiator using piezoelectric micromachined ultrasonic transducer array. Optics Letters, 45(13), 3589-3592.

Sharma, M., Amirkhan, F., Mishra, S. K., Sengupta, D., Messaddeq, Y., Blanchard, F., & Ung, B. (2020). Transmission of orbital angular momentum and cylindrical vector beams in a large-bandwidth annular core photonic crystal fiber. Fibers, 8(4), 22.

Amirkhan, F., Sakata, R., Takiguchi, K., Arikawa, T., Ozaki, T., Tanaka, K., & Blanchard, F. (2019). Characterization of thin-film optical properties by THz near-field imaging method. JOSA B, 36(9), 2593-2601.

Dambul, K. D., Poh, S. Y., Tamchek, N., Tee, D. C., Amirkhan, F., Yeo, K. S., ... & Mahamd Adikan, F. R. (2019). Fabrication and characterization of Ge-doped flat fibres. Journal of Modern Optics, 66(11), 1219-1225.

Poh, S. Y., Mahdiraji, G. A., Sua, Y. M., Amirkhan, F., Tee, D. C., Yeo, K. S., & Adikan, F. R. M. (2017). Single-Mode Operation in Flat Fibers Slab Waveguide via Modal Leakage. IEEE Photonics Journal, 9(3), 1-9.

Refereed internal and international conference papers:

Amirkhan, F., Gratuze, M., Ropagnol, X., Ozaki, T., Nabki, F., & Blanchard, F. (2020, November). Terahertz differentiator using a piezoelectric micromachined device. In 2020 45th International Conference on Infrared, Millimeter, and Terahertz Waves (IRMMW-THz) (pp. 1-1). IEEE.

Amirkhan, F., Robichaud, A., Ropagnol, X., Gratuze, M., Ozaki, T., Nabki, F., & Blanchard, F. (2020, July). Simulation study of a piezoelectric micromachined ultrasonic transducer as terahertz differentiator. In Novel Optical Materials and Applications (pp. NoM4C-5). Optical Society of America.

Sharma, M., Amirkhan, F., Mishra, S. K., Sengupta, D., Messaddeq, Y., Blanchard, F., & Ung, B. (2020, July). Annular core photonic crystal fiber for transmission of endlessly mono-radial vortex beams. In Specialty Optical Fibers (pp. SoM3H-7). Optical Society of America.

Sharma, M., Amirkhan, F., Mishra, S. K., Sengupta, D., Messaddeq, Y., Blanchard, F., & Ung, B. (2020, May). Annular core photonic crystal fiber for propagation of optical vortices. In 2020 Conference on Lasers and Electro-Optics (CLEO) (pp. 1-2). IEEE.

Amirkhan, F., Sakata, R., Takiguchi, K., Arikawa, T., Ozaki, T., Tanaka, K., & Blanchard, F. (2019, September). Characterization of thin film materials using near field THz imaging. In 2019 44th International Conference on Infrared, Millimeter, and Terahertz Waves (IRMMW-THz) (pp. 1-2). IEEE.

Amirkhan, F., Nechache, R., Sakata, R., Takiguchi, K., Arikawa, T., Ozaki, T., ... & Blanchard, F. (2018, June). Characterization of thin-film optical properties by THz near-field imaging. In 2018 Photonics North (PN) (pp. 1-1). IEEE.

Amirkhan, F., Ozaki, T., Tanaka, K., & Blanchard, F. (2018). Material characterization through near field THz imaging, in the 2nd International conference on advanced materials and processes for environment, energy and health (iCAMP).

Blanchard, F., Nechache, R., Sakata, R., Amirkhan, F., Takiguchi, K., Arikawa, T., & Tanaka, K. (2018). Near-field terahertz imaging using Bi2FeCrO6 (BFCO) thin-film sensor, in Progress in Electromagnetics Research Symposium (PIERS).

LIST OF REFERENCES

TeraVil Ltd | Free space THz Detector. Consulted at https://www.teravil.lt/detector.php.

Adam, A., Brok, J., Seo, M., Ahn, K., Kim, D., Kang, J., Park, Q. H., Nagel, M. & Planken, P. (2008). Advanced terahertz electric near-field measurements at sub-wavelength diameter metallic apertures. *Optics Express*, 16(10), 7407–7417.

Adam, A. J. L. (2011). Review of near-field terahertz measurement methods and their applications. *J.Infrared Millim.Terahertz Waves*, 32(8-9), 976.

Adomavičius, R., Urbanowicz, A., Molis, G., Krotkus, A. & Šatkovskis, E. (2004). Terahertz emission from p-lnAs due to the instantaneous polarization. *Applied physics letters*, 85(13), 2463–2465.

Aillerie, M., Theofanous, N. & Fontana, M. (2000). Measurement of the electro-optic coefficients: description and comparison of the experimental techniques. *Applied Physics B*, 70(3), 317–334.

Al-Fuqaha, A., Guizani, M., Mohammadi, M., Aledhari, M. & Ayyash, M. (2015). Internet of Things: A Survey on Enabling Technologies, Protocols, and Applications. *IEEE Communications Surveys Tutorials*, 17(4), 2347–2376. doi: 10.1109/COMST.2015.2444095. Conference Name: IEEE Communications Surveys Tutorials.

Albert, S., Petkie, D. T., Bettens, R. P., Belov, S. P. & Lucia, F. C. D. (1998). Peer reviewed: FASSST: A new gas-phase analytical tool. *Analytical chemistry*, 70(21), 719A–727A.

Amirkhan, F., Sakata, R., Takiguchi, K., Arikawa, T., Ozaki, T., Tanaka, K. & Blanchard, F. (2019). Characterization of thin-film optical properties by THz near-field imaging method. *JOSA B*, 36(9), 2593–2601.

Amirkhan, F., Robichaud, A., Ropagnol, X., Gratuze, M., Ozaki, T., Nabki, F. & Blanchard, F. (2020). Active terahertz time differentiator using piezoelectric micromachined ultrasonic transducer array. *Optics Letters*, 45(13), 3589–3592.

Asghari, M. H. & Azaña, J. (2009). All-optical Hilbert transformer based on a single phase-shifted fiber Bragg grating: design and analysis. *Optics letters*, 34(3), 334–336.

Ashrafi, R. & Azaña, J. (2012). Figure of merit for photonic differentiators. *Optics Express*, 20(3), 2626–2639.

Auston, D. H., Cheung, K. P. & Smith, P. R. (1984). Picosecond photoconducting Hertzian dipoles. *Applied physics letters*, 45(3), 284–286.

Azad, A. K., Taylor, A. J., Smirnova, E. & O'Hara, J. F. (2008). Characterization and analysis of terahertz metamaterials based on rectangular split-ring resonators. *Applied Physics Letters*, 92(1), 011119.

Azaña, J. (2010). Ultrafast analog all-optical signal processors based on fiber-grating devices. *IEEE Photonics Journal*, 2(3), 359–386.

Bagiante, S., Enderli, F., Fabiańska, J., Sigg, H. & Feurer, T. (2015). Giant electric field enhancement in split ring resonators featuring nanometer-sized gaps. *Scientific Reports*, 5, 8051.

Bakker, H., Cho, G., Kurz, H., Wu, Q. & Zhang, X.-C. (1998). Distortion of terahertz pulses in electro-optic sampling. *JOSA B*, 15(6), 1795–1801.

Baxter, J. B. & Guglietta, G. W. (2011). Terahertz spectroscopy. *Analytical chemistry*, 83(12), 4342–4368.

Bell, G. (2017). *A terahertz emission spectrometer for the study of ultrafast carrier dynamics in semiconductors*. McGill University (Canada).

Berrier, A., Schaafsma, M. C., Nonglaton, G., Bergquist, J. & Rivas, J. G. (2012). Selective detection of bacterial layers with terahertz plasmonic antennas. *Biomedical optics express*, 3(11), 2937–2949.

Bharadwaj, P., Deutsch, B. & Novotny, L. (2009). Optical antennas. *Advances in Optics and Photonics*, 1(3), 438–483.

Bitzer, A., Merbold, H., Thoman, A., Feurer, T., Helm, H. & Walther, M. (2009). Terahertz near-field imaging of electric and magnetic resonances of a planar metamaterial. *Optics Express*, 17(5), 3826–3834.

Blanchard, F., Razzari, L., Bandulet, H.-C., Sharma, G., Morandotti, R., Kieffer, J.-C., Ozaki, T., Reid, M., Tiedje, H., Haugen, H. et al. (2007). Generation of 1.5 μJ single-cycle terahertz pulses by optical rectification from a large aperture ZnTe crystal. *Optics Express*, 15(20), 13212–13220.

Blanchard, F., Doi, A., Tanaka, T., Hirori, H., Tanaka, H., Kadoya, Y. & Tanaka, K. (2011). Real-time terahertz near-field microscope. *Optics Express*, 19(9), 8277–8284.

Blanchard, F., Ooi, K., Tanaka, T., Doi, A. & Tanaka, K. (2012). Terahertz spectroscopy of the reactive and radiative near-field zones of split ring resonator. *Optics express*, 20(17), 19395–19403.

Blanchard, F., Doi, A., Tanaka, T. & Tanaka, K. (2013). Real-time, subwavelength terahertz imaging. *Annual Review of Materials Research*, 43, 237–259.

Blanchard, F., Ropagnol, X., Hafez, H., Razavipour, H., Bolduc, M., Morandotti, R., Ozaki, T. & Cooke, D. G. (2014a). Effect of extreme pump pulse reshaping on intense terahertz emission in lithium niobate at multimilliJoule pump energies. *Optics letters*, 39(15), 4333–4336.

Blanchard, F., Sumida, K., Wolpert, C., Tsotsalas, M., Tanaka, T., Doi, A., Kitagawa, S., Cooke, D., Furukawa, S. & Tanaka, K. (2014b). Terahertz phase contrast imaging of sorption kinetics in porous coordination polymer nanocrystals using differential optical resonator. *Optics express*, 22(9), 11061–11069.

Blanchard, F. & Tanaka, K. (2016). Improving time and space resolution in electro-optic sampling for near-field terahertz imaging. *Optics Letters*, 41(20), 4645–4648.

Blanchard, F., Chai, X., Tanaka, T., Arikawa, T., Ozaki, T., Morandotti, R. & Tanaka, K. (2018). Terahertz microscopy assisted by semiconductor nonlinearities. *Optics Letters*, 43(20), 4997–5000.

Burford, N. M. & El-Shenawee, M. O. (2017). Review of terahertz photoconductive antenna technology. *Optical Engineering*, 56(1), 010901.

Cai, H., Huang, Q., Hu, X., Liu, Y., Fu, Z., Zhao, Y., He, H. & Lu, Y. (2018a). All-Optical and Ultrafast Tuning of Terahertz Plasmonic Metasurfaces. *Advanced Optical Materials*, 6(14).

Cai, Y., Qin, Z., Cui, F., Li, G. Y. & McCann, J. A. (2018b). Modulation and Multiple Access for 5G Networks. *IEEE Communications Surveys Tutorials*, 20(1).

Chan, W. L., Deibel, J. & Mittleman, D. M. (2007). Imaging with terahertz radiation. *Reports on progress in physics*, 70(8), 1325.

Chang, G., Divin, C. J., Liu, C.-H., Williamson, S. L., Galvanauskas, A. & Norris, T. B. (2006). Power scalable compact THz system based on an ultrafast Yb-doped fiber amplifier. *Optics Express*, 14(17), 7909–7913.

Chen, H.-T., Kersting, R. & Cho, G. C. (2003). Terahertz imaging with nanometer resolution. *Applied Physics Letters*, 83(15), 3009–3011.

Chen, Q., Jiang, Z., Xu, G. & Zhang, X.-C. (2000). Near-field terahertz imaging with a dynamic aperture. *Optics letters*, 25(15), 1122–1124.

Chen, Z., Ma, X., Zhang, B., Zhang, Y., Niu, Z., Kuang, N., Chen, W., Li, L. & Li, S. (2019). A survey on terahertz communications. *China Communications*, 16(2), 1–35.

Chuang, S. L., Schmitt-Rink, S., Greene, B. I., Saeta, P. N. & Levi, A. F. (1992). Optical rectification at semiconductor surfaces. *Physical review letters*, 68(1), 102.

Chuang, S. L., Planken, P., Brener, I., Roskos, H. & Nuss, M. (1994). Generation of terahertz electromagnetic pulses from quantum-well structures. *IEEE journal of quantum electronics*, 30(6), 1478–1488.

Cocker, T., Jelic, V., Hillenbrand, R. & Hegmann, F. (2021). Nanoscale terahertz scanning probe microscopy. *Nature Photonics*, 15(8), 558–569.

Cocker, T. L., Jelic, V., Gupta, M., Molesky, S. J., Burgess, J. A., De Los Reyes, G., Titova, L. V., Tsui, Y. Y., Freeman, M. R. & Hegmann, F. A. (2013). An ultrafast terahertz scanning tunnelling microscope. *Nature Photonics*, 7(8), 620–625.

Cooke, D. G. (2007). *Time-resolved terahertz spectroscopy of bulk and nanoscale semiconductors*. (Ph.D. thesis).

Cooper, G. & Cowan, D. (2004). Filtering using variable order vertical derivatives. *Computers & Geosciences*, 30(5), 455–459.

Coutaz, J.-L., Garet, F. & Wallace, V. P. (2018). *Principles of Terahertz time-domain spectroscopy: an introductory textbook*. CRC Press.

Cowen, A., Hames, G., Glukh, K. & Hardy, B. (2014). PiezoMUMPs design handbook. *MEMSCAP Inc*, 1.

Cowley, J. (1995). *Diffraction Physics*. Elsevier Science.

Cui, T., Smith, D. & Liu, R. (2010). Metamaterials: Theory, Design, and Applications. 12 Springer. *New York*, 13.

Danciu, M., Alexa-Stratulat, T., Stefanescu, C., Dodi, G., Tamba, B. I., Mihai, C. T., Stanciu, G. D., Luca, A., Spiridon, I. A., Ungureanu, L. B. et al. (2019). Terahertz spectroscopy and imaging: a cutting-edge method for diagnosing digestive cancers. *Materials*, 12(9), 1519.

Datta, S. & Das, B. (1990). Electronic analog of the electro-optic modulator. *Applied Physics Letters*, 56(7), 665–667.

Dekorsy, T., Auer, H., Bakker, H. J., Roskos, H. G. & Kurz, H. (1996). THz electromagnetic emission by coherent infrared-active phonons. *Physical Review B*, 53(7), 4005.

Dexheimer, S. L. (2007). *Terahertz spectroscopy: principles and applications*. CRC press.

Doi, A., Blanchard, F., Tanaka, T. & Tanaka, K. (2011). Improving spatial resolution of real-time terahertz near-field microscope. *Journal of Infrared, Millimeter, and Terahertz Waves*, 32(8), 1043–1051.

Dubrovkin, I. (1983). Spectrometry by recording derivatives. *Journal of Applied Spectroscopy*, 39(6), 1341–1353.

Elayan, H., Amin, O., Shihada, B., Shubair, R. M. & Alouini, M.-S. (2019). Terahertz band: The last piece of RF spectrum puzzle for communication systems. *IEEE Open Journal of the Communications Society*, 1, 1–32.

Enami, Y., Derose, C., Mathine, D., Loychik, C., Greenlee, C., Norwood, R. A., Kim, T., Luo, J., Tian, Y., Jen, A.-Y. et al. (2007). Hybrid polymer/sol–gel waveguide modulators with exceptionally large electro–optic coefficients. *Nature Photonics*, 1(3), 180.

Fang, Y., Lou, Y. & Ruan, Z. (2017). On-grating graphene surface plasmons enabling spatial differentiation in the terahertz region. *Optics letters*, 42(19), 3840–3843.

Farman, J. C., Gardiner, B. G. & Shanklin, J. D. (1985). Large losses of total ozone in Antarctica reveal seasonal ClO x/NO x interaction. *Nature*, 315(6016), 207–210.

Federici, J. & Moeller, L. (2010). Review of terahertz and subterahertz wireless communications. *Journal of Applied Physics*, 107(11), 6.

Fellgett, P. (1949). On the ultimate sensitivity and practical performance of radiation detectors. *JOSA*, 39(11), 970–976.

Ferguson, B. & Zhang, X.-C. (2002). Materials for terahertz science and technology. *Nature materials*, 1(1), 26–33.

Feurer, T., Stoyanov, N. S., Ward, D. W., Vaughan, J. C., Statz, E. R. & Nelson, K. A. (2007). Terahertz polaritonics. *Annu. Rev. Mater. Res.*, 37, 317–350.

Filin, A., Stowe, M. & Kersting, R. (2001). Time-domain differentiation of terahertz pulses. *Optics Letters*, 26(24), 2008–2010.

Gilat, A. (2013). *Numerical methods for engineers and scientists*. Wiley Global Education.

Gonzalez, R. C. & Woods, R. E. (2002). *Digital image processing* (ed. 2nd ed). Upper Saddle River, N.J: Prentice Hall.

Gratuze, M., Alameh, A. H. & Nabki, F. (2019). Design of the squared daisy: a multi-mode energy harvester, with reduced variability and a non-linear frequency response. *Sensors*, 19(15), 3247.

Grischkowsky, D., Keiding, S., Van Exter, M. & Fattinger, C. (1990). Far-infrared time-domain spectroscopy with terahertz beams of dielectrics and semiconductors. *JOSA B*, 7(10), 2006–2015.

Gu, J., Singh, R., Tian, Z., Cao, W., Xing, Q., He, M., Zhang, J. W., Han, J., Chen, H.-T. & Zhang, W. (2010). Terahertz superconductor metamaterial. *Applied Physics Letters*, 97(7), 071102.

Gubbi, J., Buyya, R., Marusic, S. & Palaniswami, M. (2013). Internet of Things (IoT): A vision, architectural elements, and future directions. *Future Generation Computer Systems*, 29(7), 1645–1660. doi: 10.1016/j.future.2013.01.010.

Guerboukha, H., Nallappan, K. & Skorobogatiy, M. (2018). Toward real-time terahertz imaging. *Advances in Optics and Photonics*, 10(4), 843–938.

Guo, C., Xiao, M., Minkov, M., Shi, Y. & Fan, S. (2018). Photonic crystal slab Laplace operator for image differentiation. *Optica*, 5(3), 251–256.

Hafez, H., Chai, X., Ibrahim, A., Mondal, S., Férachou, D., Ropagnol, X. & Ozaki, T. (2016). Intense terahertz radiation and their applications. *Journal of Optics*, 18(9), 093004.

Han, P. & Zhang, X. (2001). Free-space coherent broadband terahertz time-domain spectroscopy. *Measurement Science and Technology*, 12(11), 1747.

Hangyo, M., Tomozawa, S., Murakami, Y., Tonouchi, M., Tani, M., Wang, Z., Sakai, K. & Nakashima, S. (1996). Terahertz radiation from superconducting YBa2Cu3O7-δ thin films excited by femtosecond optical pulses. *Applied physics letters*, 69(14), 2122–2124.

Hangyo, M., Tani, M. & Nagashima, T. (2005). Terahertz time-domain spectroscopy of solids: a review. *International journal of infrared and millimeter waves*, 26(12), 1661–1690.

Hansen, W. N. (1973). Optical characterization of thin films: theory. *JOSA*, 63(7), 793–802.

Harde, H., Katzenellenbogen, N. & Grischkowsky, D. (1994). Terahertz coherent transients from methyl chloride vapor. *JOSA B*, 11(6), 1018–1030.

Hebling, J., Stepanov, A., Almási, G., Bartal, B. & Kuhl, J. (2004). Tunable THz pulse generation by optical rectification of ultrashort laser pulses with tilted pulse fronts. *Applied Physics B*, 78(5), 593–599.

Hebling, J., Almasi, G., Kozma, I. Z. & Kuhl, J. (2002). Velocity matching by pulse front tilting for large-area THz-pulse generation. *Optics Express*, 10(21), 1161–1166.

Heiliger, H.-M., Vossebürger, M., Roskos, H., Kurz, H., Hey, R. & Ploog, K. (1996). Application of liftoff low-temperature-grown GaAs on transparent substrates for THz signal generation. *Applied physics letters*, 69(19), 2903–2905.

Hilton, D., Prasankumar, R., Trugman, S., Taylor, A. & Averitt, R. (2006). On photo-induced phenomena in complex materials: probing quasiparticle dynamics using infrared and far-infrared pulses. *Journal of the Physical Society of Japan*, 75(1), 011006.

Hirori, H., Doi, A., Blanchard, F. & Tanaka, K. (2011). Single-cycle terahertz pulses with amplitudes exceeding $1MV$/cm generated by optical rectification in $LiNbO_3$. *Applied Physics Letters*, 98(9), 091106.

Hoerman, B., Nichols, B., Nystrom, M. & Wessels, B. W. (1999). Dynamic response of the electro-optic effect in epitaxial KNbO 3. *Applied Physics Letters*, 75(18), 2707–2709.

Holcomb, M. & Little, W. (1992). Cascading lock-in amplification: Application to wavelength modulation spectroscopy. *Review of scientific instruments*, 63(12), 5570–5575.

Howells, S. & Schlie, L. (1996). Transient terahertz reflection spectroscopy of undoped InSb from 0.1 to 1.1 THz. *Applied Physics Letters*, 69(4), 550–552.

Huang, Y., Yao, Z., He, C., Zhu, L., Zhang, L., Bai, J. & Xu, X. (2019). Terahertz surface and interface emission spectroscopy for advanced materials. *Journal of Physics: Condensed Matter*, 31(15), 153001.

Huber, A. J., Keilmann, F., Wittborn, J., Aizpurua, J. & Hillenbrand, R. (2008). Terahertz near-field nanoscopy of mobile carriers in single semiconductor nanodevices. *Nano letters*, 8(11), 3766–3770.

Hunsche, S., Koch, M., Brener, I. & Nuss, M. (1998). THz near-field imaging. *Optics communications*, 150(1-6), 22–26.

Hunsperger, R. G. (1995). *Integrated optics*. Springer.

Ikeda, T., Matsushita, A., Tatsuno, M., Minami, Y., Yamaguchi, M., Yamamoto, K., Tani, M. & Hangyo, M. (2005). Investigation of inflammable liquids by terahertz spectroscopy. *Applied Physics Letters*, 87(3), 034105.

Ilyakov, I., Kitaeva, G. K., Shishkin, B. & Akhmedzhanov, R. (2016). Terahertz time-domain electro-optic measurements by femtosecond laser pulses with an edge-cut spectrum. *Optics letters*, 41(13), 2998–3001.

Jackson, J. D. (1999). Classical electrodynamics. American Association of Physics Teachers.

Jaeger, R. C. & Blalock, T. N. (1997). *Microelectronic circuit design*. McGraw-Hill New York.

Jepsen, P. U., Jacobsen, R. H. & Keiding, S. (1996a). Generation and detection of terahertz pulses from biased semiconductor antennas. *JOSA B*, 13(11), 2424–2436.

Jepsen, P. U., Winnewisser, C., Schall, M., Schyja, V., Keiding, S. & Helm, H. (1996b). Detection of THz pulses by phase retardation in lithium tantalate. *Physical Review E*, 53(4), R3052.

Jepsen, P. U., Cooke, D. G. & Koch, M. (2011). Terahertz spectroscopy and imaging–Modern techniques and applications. *Laser & Photonics Reviews*, 5(1), 124–166.

Jiang, Z., Li, M. & Zhang, X.-C. (2000a). Dielectric constant measurement of thin films by differential time-domain spectroscopy. *Applied Physics Letters*, 76(22), 3221–3223. doi: 10.1063/1.126587. Publisher: American Institute of Physics.

Jiang, Z., Xu, X. & Zhang, X.-C. (2000b). Improvement of terahertz imaging with a dynamic subtraction technique. *Applied optics*, 39(17), 2982–2987.

Kampfrath, T., Tanaka, K. & Nelson, K. A. (2013). Resonant and nonresonant control over matter and light by intense terahertz transients. *Nature Photonics*, 7(9), 680–690.

Kang, T. D., Xiao, B., Avrutin, V., Özgür, Ü., Morkoç, H., Park, J. W., Lee, H. S., Lee, H., Wang, X. & Smith, D. J. (2008). Large electro-optic effect in single-crystal $Pb(Zr,Ti)O_3$ (001) measured by spectroscopic ellipsometry. *Journal of Applied Physics*, 104(9), 093103.

Kappa, J., Sokoluk, D., Klingel, S., Shemelya, C., Oesterschulze, E. & Rahm, M. (2019). Electrically Reconfigurable Micromirror Array for Direct Spatial Light Modulation of Terahertz Waves over a Bandwidth Wider Than 1 THz. *Scientific reports*, 9(1), 2597.

Karpińska, J. (2004). Derivative spectrophotometry—recent applications and directions of developments. *Talanta*, 64(4), 801–822.

Kawase, K., Ogawa, Y., Watanabe, Y. & Inoue, H. (2003). Non-destructive terahertz imaging of illicit drugs using spectral fingerprints. *Optics express*, 11(20), 2549–2554.

Ketterer, B., Uccelli, E. & i Morral, A. F. (2012). Mobility and carrier density in p-type GaAs nanowires measured by transmission Raman spectroscopy. *Nanoscale*, 4(5), 1789–1793.

Kim, D. & Kwok, H. (1995). Pulsed laser deposition of BaTiO3 thin films and their optical properties. *Applied Physics Letters*, 67(13), 1803–1805.

Kitaeva, G. K., Kovalev, S., Naumova, I., Akhmedzhanov, R., Ilyakov, I., Shishkin, B. & Suvorov, E. (2010). *A new method of terahertz detection: Probe-energy electro-optic sampling*. Conference Proceedings presented in Infrared Millimeter and Terahertz Waves (IRMMW-THz), 2010 35th International Conference on (pp. 1–2).

Klein, M. P. & Dratz, E. A. (1968). Derivative spectroscopy with recording spectrometers. *Review of Scientific Instruments*, 39(3), 397–399.

Kloos, G. (2018). Applications of Lock-in Amplifiers in Optics. *Applications of Lock-in Amplifiers in Optics*.

Klos, M., Bartholdt, R., Klier, J., Lampin, J.-F. & Beigang, R. (2015). Photoconductive antennas based on low temperature grown GaAs on silicon substrates for broadband terahertz generation and detection. *2015 40th International Conference on Infrared, Millimeter, and Terahertz waves (IRMMW-THz)*, pp. 1–1.

Koch, M. (2005). Terahertz-technology. *Quo Vadis Photonik*, 4, 1–5.

Kong, D.-Y., Wu, X.-J., Wang, B., Gao, Y., Dai, J., Wang, L., Ruan, C.-J. & Miao, J.-G. (2018). High resolution continuous wave terahertz spectroscopy on solid-state samples with coherent detection. *Optics express*, 26(14), 17964–17976.

Kozlov, G. & Volkov, A. (1998). Coherent source submillimeter wave spectroscopy. *Millimeter and submillimeter wave spectroscopy of solids*, 51–109.

Kumar, N., Strikwerda, A. C., Fan, K., Zhang, X., Averitt, R. D., Planken, P. C. & Adam, A. J. (2012). *THz* near-field Faraday imaging in hybrid metamaterials. *Optics Express*, 20(10), 11277–11287.

Köhler, R., Tredicucci, A., Beltram, F., Beere, H. E., Linfield, E. H., Davies, A. G., Ritchie, D. A., Iotti, R. C. & Rossi, F. (2002). Terahertz semiconductor-heterostructure laser. *Nature*, 417(6885), 156–159.

Kübler, C., Huber, R. & Leitenstorfer, A. (2005). Ultrabroadband terahertz pulses: generation and field-resolved detection. *Semiconductor science and technology*, 20(7), S128.

Lee, A. (1992). Derivative spectroscopy and its applications in drug analysis. *Chin. Pharm. J*, 44, 87–96.

Lee, Y. S., Kim, G.-D., Kim, W.-J., Lee, S.-S., Lee, W.-G. & Steier, W. H. (2011). Hybrid Si-LiNbO $_3$ microring electro-optically tunable resonators for active photonic devices. *Optics Letters*, 36(7), 1119–1121.

Lee, Y.-S. (2009). *Principles of terahertz science and technology*. Springer Science & Business Media.

Li, J. & Li, J. (2020). Terahertz (THz) Generator and Detection. *Electrical Science & Engineering*, 2, 11–25.

Li, Z.-M., Sullivan, B. T. & Parsons, R. R. (1988). Use of the 4× 4 matrix method in the optics of multilayer magnetooptic recording media. *Applied Optics*, 27(7), 1334–1338.

Lin, H., Fischer, B. M., Mickan, S. P. & Abbott, D. (2007). Review of THz near-field methods. *Smart Structures, Devices, and Systems III*, 6414, 64140L.

Linden, S., Enkrich, C., Dolling, G., Klein, M. W., Zhou, J., Koschny, T., Soukoulis, C. M., Burger, S., Schmidt, F. & Wegener, M. (2006). Photonic metamaterials: magnetism at optical frequencies. *IEEE Journal of Selected Topics in Quantum Electronics*, 12(6), 1097–1105.

Liu, H.-B., Chen, Y., Bastiaans, G. J. & Zhang, X.-C. (2006). Detection and identification of explosive RDX by THz diffuse reflection spectroscopy. *Optics Express*, 14(1), 415–423.

Liu, W., Mak, C. & Wong, K. (2009). $Sr_{1.8}Ca_{0.2}NaNb_5O_{15}$ films for electro-optic modulator application. *Journal of Physics D: Applied Physics*, 42(10), 105114.

Lloyd-Hughes, J. & Jeon, T.-I. (2012). A review of the terahertz conductivity of bulk and nano-materials. *Journal of Infrared, Millimeter, and Terahertz Waves*, 33(9), 871–925.

Lo, S.-Z. A. & Murphy, T. E. (2009). Nanoporous silicon multilayers for terahertz filtering. *Optics letters*, 34(19), 2921–2923.

Loewenstein, E. V. (1966). The history and current status of Fourier transform spectroscopy. *Applied Optics*, 5(5), 845–854.

Lotspeich, J., Stephens, R. & Henderson, D. (1982). Electrooptic tunable filters for infrared wavelengths. *IEEE J. of Quantum Electron.*, 18(8), 1253–1258.

Lu, Y., Jin, G.-H., Cronin-Golomb, M., Liu, S.-W., Jiang, H., Wang, F.-L., Zhao, J., Wang, S.-Q. & Drehman, A. (1998). Fabrication and optical characterization of $Pb(Mg_{1/3}Nb_{2/3})O_3$-$PbTiO_3$ planar thin film optical waveguides. *Applied Physics Letters*, 72(23), 2927–2929.

Ma, J., Shrestha, R., Adelberg, J., Yeh, C.-Y., Hossain, Z., Knightly, E., Jornet, J. M. & Mittleman, D. M. (2018). Security and eavesdropping in terahertz wireless links. *Nature*, 563(7729).

Ma, Z., Geng, Z., Fan, Z., Liu, J. & Chen, H. (2019). Modulators for terahertz communication: The current state of the art. *Research*, 2019.

Mathanker, S. K., Weckler, P. R. & Wang, N. (2013). Terahertz (THz) applications in food and agriculture: A review. *Transactions of the ASABE*, 56(3), 1213–1226.

Mathews, J. & Walker, R. L. (1970). *Mathematical methods of physics*. WA Benjamin New York.

McKee, R. A. & Walker, F. J. (2000). Silicon-integrated thin-film structure for electro-optic applications. Google Patents. US Patent 6,103,008.

Mitrofanov, O., Lee, M., Hsu, J. W., Brener, I., Harel, R., Federici, J. F., Wynn, J. D., Pfeiffer, L. N. & West, K. W. (2001). Collection-mode near-field imaging with 0.5-THz pulses. *IEEE Journal of Selected Topics in Quantum Electronics*, 7(4), 600–607.

Mittleman, D. (2003). Terahertz imaging. *Sensing with terahertz radiation*, 85, 117–117.

Mittleman, D. (2013). *Sensing with terahertz radiation*. Springer.

Mittleman, D. M. (2018). Twenty years of terahertz imaging. *Optics express*, 26(8), 9417–9431.

Mittleman, D. M., Jacobsen, R. H., Neelamani, R., Baraniuk, R. G. & Nuss, M. C. (1998). Gas sensing using terahertz time-domain spectroscopy. *Applied Physics B*, 67(3), 379–390.

Møller, U., Cooke, D. G., Tanaka, K. & Jepsen, P. U. (2009). Terahertz reflection spectroscopy of Debye relaxation in polar liquids. *JOSA B*, 26(9), A113–A125.

Mu, X., Zotova, I. B. & Ding, Y. J. (2008). Power scaling on efficient generation of ultrafast terahertz pulses. *IEEE Journal of Selected Topics in Quantum Electronics*, 14(2), 315–332.

Möller, K. D. & Rothschild, W. G. (1971). Far-infrared spectroscopy. *New York: Wiley, 1971*.

Naftaly, M., Molloy, J., Magnusson, B., Andreev, Y. & Lanskii, G. (2016). Silicon carbide—a high-transparency nonlinear material for THz applications. *Optics express*, 24(3), 2590–2595.

Naftaly, M., Vieweg, N. & Deninger, A. (2019). Industrial applications of terahertz sensing: state of play. *Sensors*, 19(19), 4203.

Nagai, N. & Fukasawa, R. (2004). Abnormal dispersion of polymer films in the THz frequency region. *Chemical Physics Letters*, 388(4), 479–482.

Nagai, N., Imai, T., Fukasawa, R., Kato, K. & Yamauchi, K. (2004). Analysis of the intermolecular interaction of nanocomposites by THz spectroscopy. *Applied physics letters*, 85(18), 4010–4012.

Nagai, N., Sumitomo, M., Imaizumi, M. & Fukasawa, R. (2006). Characterization of electron-or proton-irradiated Si space solar cells by THz spectroscopy. *Semiconductor science and technology*, 21(2), 201.

Nagatsuma, T., Ducournau, G. & Renaud, C. C. (2016). Advances in terahertz communications accelerated by photonics. *Nature Photonics*, 10(6), 371–379.

Nahata, A., Auston, D. H., Heinz, T. F. & Wu, C. (1996a). Coherent detection of freely propagating terahertz radiation by electro-optic sampling. *Applied physics letters*, 68(2), 150–152.

Nahata, A., Weling, A. S. & Heinz, T. F. (1996b). A wideband coherent terahertz spectroscopy system using optical rectification and electro-optic sampling. *Applied physics letters*, 69(16), 2321–2323.

Nashima, S., Morikawa, O., Takata, K. & Hangyo, M. (2001). Temperature dependence of optical and electronic properties of moderately doped silicon at terahertz frequencies. *Journal of applied physics*, 90(2), 837–842.

Neu, J. & Schmuttenmaer, C. A. (2018). Tutorial: An introduction to terahertz time domain spectroscopy (THz-TDS). *Journal of Applied Physics*, 124(23), 231101.

Neu, J., Krolla, B., Paul, O., Reinhard, B., Beigang, R. & Rahm, M. (2010). Metamaterial-based gradient index lens with strong focusing in the THz frequency range. *Optics express*, 18(26), 27748–27757.

Neu, J., Nikonow, H. & Schmuttenmaer, C. A. (2018). Terahertz spectroscopy and density functional theory calculations of DL-Norleucine and DL-Methionine. *The Journal of Physical Chemistry A*, 122(28), 5978–5982.

Ngo, N., Yu, S. F., Tjin, S. & Kam, C. (2004). A new theoretical basis of higher-derivative optical differentiators. *Optics Communications*, 230(1-3), 115–129.

Nikogosyan, D. N. (2006). *Nonlinear optical crystals: a complete survey*. Springer Science & Business Media.

Novotny, L. & Van Hulst, N. (2011). Antennas for light. *Nature photonics*, 5(2), 83–90.

Nuss, M. C. & Orenstein, J. (1998). Terahertz time-domain spectroscopy. In *Millimeter and submillimeter wave spectroscopy of solids* (pp. 7–50). Springer.

O'Haver, T. C., Fell, A. F., Smith, G., Gans, P., Sneddon, J., Bezur, L., Michel, R., Ottaway, J., Miller, J., Ahmad, T. et al. (1982). Derivative spectroscopy and its applications in analysis. *Analytical Proceedings*, 19(1), 22–46.

Olmon, R. L., Rang, M., Krenz, P. M., Lail, B. A., Saraf, L. V., Boreman, G. D. & Raschke, M. B. (2010). Determination of electric-field, magnetic-field, and electric-current distributions of infrared optical antennas: a near-field optical vector network analyzer. *Physical Review Letters*, 105(16), 167403.

Ortiz, J. D. (2011). Application of Visible/near Infrared derivative spectroscopy to Arctic paleoceanography. *IOP Conference Series: Earth and Environmental Science*, 14(1), 012011.

O'Hara, J. F., Withayachumnankul, W. & Al-Naib, I. (2012). A review on thin-film sensing with terahertz waves. *Journal of Infrared, Millimeter, and Terahertz Waves*, 33(3), 245–291.

Padilla, W. J., Taylor, A. J., Highstrete, C., Lee, M. & Averitt, R. D. (2006). Dynamical electric and magnetic metamaterial response at terahertz frequencies. *Physical review letters*, 96(10), 107401.

Palmer, R., Alloatti, L., Korn, D., Schindler, P. C., Baier, M., Bolten, J., Wahlbrink, T., Waldow, M., Dinu, R., Freude, W. et al. (2013). Low power Mach–Zehnder modulator in silicon-organic hybrid technology. *IEEE Photonics Technology Letters*, 25(13), 1226–1229.

Park, D. H. (2008). *Characterization of linear electro-optic effect of poled organic thin films*. (Ph.D. thesis).

Park, H. & Son, J.-H. (2021). Machine Learning Techniques for THz Imaging and Time-Domain Spectroscopy. *Sensors*, 21(4), 1186.

Park, S., Hong, J., Choi, S., Kim, H., Park, W., Han, S., Park, J., Lee, S., Kim, D. & Ahn, Y. (2014). Detection of microorganisms using terahertz metamaterials. *Scientific reports*, 4, 4988.

Park, S., Cha, S., Shin, G. & Ahn, Y. (2017). Sensing viruses using terahertz nano-gap metamaterials. *Biomedical optics express*, 8(8), 3551–3558.

Park, Y., Ahn, T.-J., Dai, Y., Yao, J. & Azaña, J. (2008). All-optical temporal integration of ultrafast pulse waveforms. *Optics Express*, 16(22), 17817–17825.

Pedersen, J. & Keiding, S. (1992). THz time-domain spectroscopy of nonpolar liquids. *IEEE Journal of Quantum Electronics*, 28(10), 2518–2522.

Pendry, J. B., Holden, A. J., Robbins, D. J. & Stewart, W. (1999). Magnetism from conductors and enhanced nonlinear phenomena. *IEEE transactions on microwave theory and techniques*, 47(11), 2075–2084.

Petraru, A., Schubert, J., Schmid, M., Trithaveesak, O. & Buchal, C. (2003). Integrated optical Mach Zehnder modulator based on polycrystalline BaTiO 3. *Optics Letters*, 28(24), 2527–2529.

Piesiewicz, R., Jansen, C., Wietzke, S., Mittleman, D., Koch, M. & Kürner, T. (2007). Properties of building and plastic materials in the THz range. *International Journal of Infrared and Millimeter Waves*, 28(5), 363–371.

Podzorov, A. & Gallot, G. (2008). Low-loss polymers for terahertz applications. *Applied optics*, 47(18), 3254–3257.

Porer, M., Ménard, J.-M. & Huber, R. (2014). Shot noise reduced terahertz detection via spectrally postfiltered electro-optic sampling. *Optics letters*, 39(8), 2435–2438.

Rabiei, P. & Gunter, P. (2004). Optical and electro-optical properties of submicrometer lithium niobate slab waveguides prepared by crystal ion slicing and wafer bonding. *Applied Physics Letters*, 85(20), 4603–4605.

Rahm, M., Li, J.-S. & Padilla, W. J. (2013). THz wave modulators: a brief review on different modulation techniques. *Journal of Infrared, Millimeter, and Terahertz Waves*, 34(1), 1–27.

Rana, D. S. & Tonouchi, M. (2020). Terahertz Emission Functionality of High-Temperature Superconductors and Similar Complex Systems. *Advanced Optical Materials*, 8(3), 1900892.

Razzari, L., Toma, A., Shalaby, M., Clerici, M., Zaccaria, R. P., Liberale, C., Marras, S., Al-Naib, I. A., Das, G., De Angelis, F. et al. (2011). Extremely large extinction efficiency and field enhancement in terahertz resonant dipole nanoantennas. *Optics express*, 19(27), 26088–26094.

Redo-Sanchez, A., Heshmat, B., Aghasi, A., Naqvi, S., Zhang, M., Romberg, J. & Raskar, R. (2016). Terahertz time-gated spectral imaging for content extraction through layered structures. *Nature communications*, 7(1), 1–7.

Reimann, K., Smith, R., Weiner, A., Elsaesser, T. & Woerner, M. (2003). Direct field-resolved detection of terahertz transients with amplitudes of megavolts per centimeter. *Optics letters*, 28(6), 471–473.

Reinhard, B., Schmitt, K. M., Wollrab, V., Neu, J., Beigang, R. & Rahm, M. (2012). Metamaterial near-field sensor for deep-subwavelength thickness measurements and sensitive refractometry in the terahertz frequency range. *Applied Physics Letters*, 100(22), 221101.

Reitze, D., Haton, E., Ramesh, R., Etemad, S., Leaird, D., Sands, T., Karim, Z. & Tanguay Jr, A. (1993). Electro-optic properties of single crystalline ferroelectric thin films. *Applied Physics Letters*, 63(5), 596–598.

Ren, A., Zahid, A., Fan, D., Yang, X., Imran, M. A., Alomainy, A. & Abbasi, Q. H. (2019). State-of-the-art in terahertz sensing for food and water security–A comprehensive review. *Trends in food science & technology*, 85, 241–251.

Rice, A., Jin, Y., Ma, X., Zhang, X., Bliss, D., Larkin, J. & Alexander, M. (1994). Terahertz optical rectification from< 110> zinc-blende crystals. *Applied physics letters*, 64(11), 1324–1326.

Robichaud, A., Cicek, P., Deslandes, D. & Nabki, F. (2018a). Frequency Tuning Technique of Piezoelectric Ultrasonic Transducers for Ranging Applications. *Journal of Microelectromechanical Systems*, 27(3), 570–579. doi: 10.1109/JMEMS.2018.2831638. Conference Name: Journal of Microelectromechanical Systems.

Robichaud, A., Deslandes, D., Cicek, P.-V. & Nabki, F. (2018b). A novel topology for process variation-tolerant piezoelectric micromachined ultrasonic transducers. *Journal of Microelectromechanical Systems*, 27(6), 1204–1212.

Rodwell, M. J., Kamegawa, M., Yu, R., Case, M., Carman, E. & Giboney, K. S. (1991). GaAs nonlinear transmission lines for picosecond pulse generation and millimeter-wave sampling. *IEEE Transactions on Microwave Theory and Techniques*, 39(7), 1194–1204.

Sakai, K. & Tani, M. (2005). Introduction to terahertz pulses. *Terahertz optoelectronics*, 1–30.

Saleh, B. E. A. & Teich, M. C. (1991). Fundamentals of Photonics. *John Wiley & Sons*.

Salem, R., Foster, M. A. & Gaeta, A. L. (2013). Application of space–time duality to ultrahigh-speed optical signal processing. *Advances in Optics and Photonics*, 5(3), 274–317.

Salén, P., Basini, M., Bonetti, S., Hebling, J., Krasilnikov, M., Nikitin, A. Y., Shamuilov, G., Tibai, Z., Zhaunerchyk, V. & Goryashko, V. (2019). Matter manipulation with extreme terahertz light: Progress in the enabling THz technology. *Physics Reports*, 836-837, 1–74. doi: 10.1016/j.physrep.2019.09.002.

Sarychev, A. K. & Shalaev, V. M. (2007). *Electrodynamics of metamaterials*. World Scientific.

Schroder, D. K. (2006). *Semiconductor material and device characterization*. John Wiley & Sons.

Scott, J. F., De Araujo, P. & Carlos, A. (1989). Ferroelectric memories. *Science(Washington, D. C.)*, 246(4936), 1400–5.

Seo, M., Adam, A., Kang, J., Lee, J., Jeoung, S., Park, Q. H., Planken, P. & Kim, D. (2007). Fourier-transform terahertz near-field imaging of one-dimensional slit arrays: mapping of electric-field-, magnetic-field-, and Poynting vectors. *Optics Express*, 15(19), 11781–11789.

Seo, M., Yoo, J., Dayeh, S., Picraux, S., Taylor, A. & Prasankumar, R. (2012). Mapping carrier diffusion in single silicon core–shell nanowires with ultrafast optical microscopy. *Nano letters*, 12(12), 6334–6338.

Shen, Y., Upadhya, P., Beere, H., Linfield, E., Davies, A., Gregory, I., Baker, C., Tribe, W. & Evans, M. (2004). Generation and detection of ultrabroadband terahertz radiation using photoconductive emitters and receivers. *Applied Physics Letters*, 85(2), 164–166.

Sherwin, M. (2002). Terahertz power. *Nature*, 420(6912), 131–133.

Shi, Q., Huang, W., Lu, T., Zhang, Y., Yue, F., Qiao, S. & Xiao, Y. (2014). Nanostructured VO2 film with high transparency and enhanced switching ratio in THz range. *Applied Physics Letters*, 104(7), 071903.

Shuto, Y. & Amano, M. (1995). Reflection measurement technique of electro-optic coefficients in lithium niobate crystals and poled polymer films. *Journal of Applied Physics*, 77(9), 4632–4638.

Singleton, F. & Collier, G. (1956). Infra-red analysis by the derivative method. *Journal of Applied Chemistry*, 6(11), 495–510.

Skolnik, M. I. (1962). Introduction to radar. *Radar handbook*, 2, 21.

Slavík, R., Park, Y., Kulishov, M., Morandotti, R. & Azaña, J. (2006). Ultrafast all-optical differentiators. *Optics Express*, 14(22), 10699–10707.

Slavík, R., Park, Y., Kulishov, M., Morandotti, R. & Azaña, J. (2006). Ultrafast all-optical differentiators. *Optics Express*, 14(22), 10699–10707. Publisher: Optical Society of America.

Smith, D. R., Padilla, W. J., Vier, D., Nemat-Nasser, S. C. & Schultz, S. (2000). Composite medium with simultaneously negative permeability and permittivity. *Physical review letters*, 84(18), 4184.

Smith, D. R., Pendry, J. B. & Wiltshire, M. C. (2004). Metamaterials and negative refractive index. *Science*, 305(5685), 788–792.

Smith, R. M. & Arnold, M. A. (2011). Terahertz time-domain spectroscopy of solid samples: principles, applications, and challenges. *Applied Spectroscopy Reviews*, 46(8), 636–679.

Solomon, S., Garcia, R. R., Rowland, F. S. & Wuebbles, D. J. (1986). On the depletion of Antarctic ozone. *Nature*, 321(6072), 755–758.

Song, H.-J. & Nagatsuma, T. (2015). *Handbook of terahertz technologies: devices and applications*. CRC press.

Song, Q., Chai, L., Liu, W., Ma, Q., Li, Y., Wang, C. & Hu, M. (2019). Measuring effective electro-optic coefficient at 1040 nm by spectral intensity modulation with THz time-domain spectroscopy. *Infrared Physics & Technology*, 97, 54–57.

Staelin, D. H. (2011). *Electromagnetics and applications*. Open Course Ware-Massachusetts Institute of Technology.

Stauffer, F. R. & Sakai, H. (1968). Derivative spectroscopy. *Applied optics*, 7(1), 61–65.

Stellmacher, M., Schnell, J.-P., Adam, D. & Nagle, J. (1999). Photoconductivity investigation of the electron dynamics in GaAs grown at low temperature. *Applied physics letters*, 74(9), 1239–1241.

Stepanov, A. G., Hebling, J. & Kuhl, J. (2003). Efficient generation of subpicosecond terahertz radiation by phase-matched optical rectification using ultrashort laser pulses with tilted pulse fronts. *Applied physics letters*, 83(15), 3000–3002.

Storm, K., Halvardsson, F., Heurlin, M., Lindgren, D., Gustafsson, A., Wu, P. M., Monemar, B. & Samuelson, L. (2012). Spatially resolved Hall effect measurement in a single semiconductor nanowire. *Nature Nanotechnology*, 7(11), 718–722. doi: 10.1038/nnano.2012.190. Number: 11 Publisher: Nature Publishing Group.

Sze, S. M., Li, Y. & Ng, K. K. (2021). *Physics of semiconductor devices*. John wiley & sons.

Tang, P., Towner, D., Meier, A. & Wessels, B. (2004). Low-voltage, polarization-insensitive, electro-optic modulator based on a polydomain barium titanate thin film. *Applied Physics Letters*, 85(20), 4615–4617.

Tani, M., Matsuura, S., Sakai, K. & Nakashima, S.-i. (1997). Emission characteristics of photoconductive antennas based on low-temperature-grown GaAs and semi-insulating GaAs. *Applied optics*, 36(30), 7853–7859.

Teng, C. & Man, H. (1990). Simple reflection technique for measuring the electro-optic coefficient of poled polymers. *Applied Physics Letters*, 56(18), 1734–1736.

Thrane, L., Jacobsen, R. H., Jepsen, P. U. & Keiding, S. (1995). THz reflection spectroscopy of liquid water. *Chemical Physics Letters*, 240(4), 330–333.

Tompkins, H. & Irene, E. A. (2005). *Handbook of ellipsometry*. William Andrew.

Tonouchi, M. (2007). Cutting-edge terahertz technology. *Nature photonics*, 1(2), 97–105.

Ueno, Y. & Ajito, K. (2008). Analytical terahertz spectroscopy. *Analytical Sciences*, 24(2), 185–192.

Ulbricht, R., Hendry, E., Shan, J., Heinz, T. F. & Bonn, M. (2011). Carrier dynamics in semiconductors studied with time-resolved terahertz spectroscopy. *Reviews of Modern Physics*, 83(2), 543.

Van Der Valk, N. C., Wenckebach, T. & Planken, P. C. (2004). Full mathematical description of electro-optic detection in optically isotropic crystals. *JOSA B*, 21(3), 622–631.

Van Exter, M. & Grischkowsky, D. R. (1990). Characterization of an optoelectronic terahertz beam system. *IEEE Transactions on Microwave Theory and Techniques*, 38(11), 1684–1691.

Van Exter, M., Fattinger, C. & Grischkowsky, D. (1989). Terahertz time-domain spectroscopy of water vapor. *Optics letters*, 14(20), 1128–1130.

Vasić, B., Zografopoulos, D. C., Isić, G., Beccherelli, R. & Gajić, R. (2017). Electrically tunable terahertz polarization converter based on overcoupled metal-isolator-metal metamaterials infiltrated with liquid crystals. *Nanotechnology*, 28(12), 124002. doi: 10.1088/1361-6528/aa5bbd.

Veselago, V. G. (1968). The electrodynamics of substances with simultaneously negative values of and μ. *Soviet physics uspekhi*, 10(4), 509.

Vogt, F., Klocke, U., Rebstock, K., Schmidtke, G., Wander, V. & Tacke, M. (1999). Optical UV derivative spectroscopy for monitoring gaseous emissions. *Applied spectroscopy*, 53(11), 1352–1360.

Von Willisen, F. (1966). A tunable birefringent filter. *Applied Optics*, 5(1), 97–104.

Walther, M., Fischer, B. M., Ortner, A., Bitzer, A., Thoman, A. & Helm, H. (2010). Chemical sensing and imaging with pulsed terahertz radiation. *Analytical and bioanalytical chemistry*, 397(3), 1009–1017.

Wang, F., Furman, E. & Haertling, G. H. (1995). Electro-optic measurements of thin-film materials by means of reflection differential ellipsometry. *Journal of Applied Physics*, 78(1), 9–15.

Wang, J., Zhang, J., Chang, T. & Cui, H.-L. (2019a). A comparative study of non-destructive evaluation of glass fiber reinforced polymer composites using terahertz, X-ray, and ultrasound imaging. *International Journal of Precision Engineering and Manufacturing*, 20(6), 963–972.

Wang, L., Zhang, Y., Guo, X., Chen, T., Liang, H., Hao, X., Hou, X., Kou, W., Zhao, Y., Zhou, T. et al. (2019b). A review of THz modulators with dynamic tunable metasurfaces. *Nanomaterials*, 9(7), 965.

Wang, X., Cui, Y., Hu, D., Sun, W., Ye, J. & Zhang, Y. (2009). Terahertz quasi-near-field real-time imaging. *Optics Communications*, 282(24), 4683–4687.

Weigel, P. O., Zhao, J., Fang, K., Al-Rubaye, H., Trotter, D., Hood, D., Mudrick, J., Dallo, C., Pomerene, A. T., Starbuck, A. L. et al. (2018). Bonded thin film lithium niobate modulator on a silicon photonics platform exceeding 100 GHz 3-dB electrical modulation bandwidth. *Optics express*, 26(18), 23728–23739.

Weis, R. S. & Gaylord, T. K. (1989). Magnetooptic multilayered memory structure with a birefringent superstrate: a rigorous analysis. *Applied Optics*, 28(10), 1926–1930.

Weis, R. & Gaylord, T. (1985). Lithium niobate: summary of physical properties and crystal structure. *Applied Physics A*, 37(4), 191–203.

Werley, C. A., Wu, Q., Lin, K.-H., Tait, C. R., Dorn, A. & Nelson, K. A. (2010). Comparison of phase-sensitive imaging techniques for studying terahertz waves in structured LiNbO 3. *JOSA B*, 27(11), 2350–2359.

Wiley, P. R., Tanner, G. J., Chandler, P. M. & Anderssen, R. S. (2009). Molecular classification of barley (Hordeum vulgare L.) mutants using derivative NIR spectroscopy. *Journal of agricultural and food chemistry*, 57(10), 4042–4050.

Wilk, R., Vieweg, N., Kopschinski, O. & Koch, M. (2009). Liquid crystal based electrically switchable Bragg structure for THz waves. *Optics express*, 17(9), 7377–7382.

Wiltshire, M., Pendry, J., Young, I., Larkman, D., Gilderdale, D. & Hajnal, J. (2001). Microstructured magnetic materials for RF flux guides in magnetic resonance imaging. *Science*, 291(5505), 849–851.

Winnewisser, C., Jepsen, P. U., Schall, M., Schyja, V. & Helm, H. (1997a). Electro-optic detection of THz radiation in $LiTaO_3$, $LiNbO_3$ and *ZnTe*. *Applied Physics Letters*, 70(23), 3069–3071.

Winnewisser, C., Jepsen, P. U., Schall, M., Schyja, V. & Helm, H. (1997b). Electro-optic detection of THz radiation in \textbackslashemphLiTaO_3\$, \textbackslashemphLiNbO_3\$ and \textbackslashemphZnTe. *Applied Physics Letters*, 70(23), 3069–3071.

Wooten, E. L., Kissa, K. M., Yi-Yan, A., Murphy, E. J., Lafaw, D. A., Hallemeier, P. F., Maack, D., Attanasio, D. V., Fritz, D. J., McBrien, G. J. et al. (2000). A review of lithium niobate modulators for fiber-optic communications systems. *IEEE Journal of Sel. Top. in Quantum Electron.*, 6(1), 69–82.

Wu, Q. & Zhang, X.-C. (1996a). Ultrafast electro-optic field sensors. *Applied physics letters*, 68(12), 1604–1606.

Wu, Q. & Zhang, X.-C. (1997). Free-space electro-optics sampling of mid-infrared pulses. *Applied physics letters*, 71(10), 1285–1286.

Wu, Q., Hewitt, T. & Zhang, X.-C. (1996a). Two-dimensional electro-optic imaging of THz beams. *Applied Physics Letters*, 69(8), 1026–1028.

Wu, Q., Litz, M. & Zhang, X.-C. (1996b). Broadband detection capability of ZnTe electro-optic field detectors. *Applied Physics Letters*, 68(21), 2924–2926.

Wu, Q. & Zhang, X.-C. (1995). Free-space electro-optic sampling of terahertz beams. *Applied Physics Letters*, 67(24), 3523–3525.

Wu, Q. & Zhang, X.-C. (1996b). Design and characterization of traveling-wave electrooptic terahertz sensors. *IEEE Journal of Selected Topics in Quantum Electronics*, 2(3), 693–700.

Xiao, Z., Yang, Q., Huang, J., Huang, Z., Zhou, W., Gao, Y., Shu, R. & He, Z. (2018). Terahertz communication windows and their point-to-point transmission verification. *Applied optics*, 57(27), 7673–7680.

Xie, J., Zhu, X., Zhang, H., Zang, X., Chen, L., Balakin, A. V., Shkurinov, A. P. & Zhu, Y. (2020). Terahertz-frequency temporal differentiator enabled by a high-Q resonator. *Optics express*, 28(6), 7898–7905.

Xie, L., Yao, Y. & Ying, Y. (2014). The application of terahertz spectroscopy to protein detection: a review. *Applied Spectroscopy Reviews*, 49(6), 448–461.

Xin, X., Altan, H., Saint, A., Matten, D. & Alfano, R. (2006). Terahertz absorption spectrum of para and ortho water vapors at different humidities at room temperature. *Journal of applied physics*, 100(9), 094905.

Yang, K., Richards, P. & Shen, Y. (1971). Generation of far-infrared radiation by picosecond light pulses in LiNbO3. *Applied Physics Letters*, 19(9), 320–323.

Yariv, A. (1989). Quantum Electronics' John Wiley. *New York*.

Ye, H., Zhang, Y. & Shen, W. (2006). Carrier transport and optical properties in GaAs far-infrared/terahertz mirror structures. *Thin solid films*, 514(1), 310–315.

Yen, T.-J., Padilla, W., Fang, N., Vier, D., Smith, D., Pendry, J., Basov, D. & Zhang, X. (2004). Terahertz magnetic response from artificial materials. *Science*, 303(5663), 1494–1496.

Yu, B., Zeng, F., Yang, Y., Xing, Q., Chechin, A., Xin, X., Zeylikovich, I. & Alfano, R. (2004). Torsional vibrational modes of tryptophan studied by terahertz time-domain spectroscopy. *Biophysical Journal*, 86(3), 1649–1654.

Yu, C., Fan, S., Sun, Y. & Pickwell-MacPherson, E. (2012). The potential of terahertz imaging for cancer diagnosis: A review of investigations to date. *Quantitative imaging in medicine and surgery*, 2(1), 33.

Yu, S., Wu, X., Wang, Y., Guo, X. & Tong, L. (2017). 2D Materials for Optical Modulation: Challenges and Opportunities. *Advanced Materials*, 29(14), 1606128. Consulted at https://onlinelibrary.wiley.com/doi/abs/10.1002/adma.201606128. _eprint: https://onlinelibrary.wiley.com/doi/pdf/10.1002/adma.201606128.

Yuan, T., Xu, J. & Zhang, X.-C. (2004). Development of terahertz wave microscopes. *Infrared physics & technology*, 45(5-6), 417–425.

Zhang, B., Ma, Z., Ma, J., Wu, X., Ouyang, C., Kong, D., Hong, T., Wang, X., Yang, P., Chen, L. et al. (2021a). 1.4-mJ High Energy Terahertz Radiation from Lithium Niobates. *Laser & Photonics Reviews*, 15(3), 2000295.

Zhang, L., Chen, X. Q., Liu, S., Zhang, Q., Zhao, J., Dai, J. Y., Bai, G. D., Wan, X., Cheng, Q. & Castaldi, G. (2018a). Space-time-coding digital metasurfaces. *Nature communications*, 9(1), 4334.

Zhang, M., Wang, C., Kharel, P., Zhu, D. & Lončar, M. (2021b). Integrated lithium niobate electro-optic modulators: when performance meets scalability. *Optica*, 8(5), 652–667.

Zhang, X. C., Shkurinov, A. & Zhang, Y. (2017). Extreme terahertz science. *Nature Photonics*, 11(1), 16–18.

Zhang, X., Wang, C., Zhang, W., Ai, S., Liao, W., Hsieh, J.-C., He, B., Chen, Z., Hu, Z., Zhang, N. et al. (2021c). High-speed all-optical processing for spectrum. *Optics Express*, 29(1), 305–314.

Zhang, X. & Wu, X. (2021). Preface to the special issue on “Terahertz Science and Applications”. Higher Education Press.

Zhang, Y., Zhao, Y., Liang, S., Zhang, B., Wang, L., Zhou, T., Kou, W., Lan, F., Zeng, H. & Han, J. (2018b). Large phase modulation of THz wave via an enhanced resonant active HEMT metasurface. *Nanophotonics*, 8(1), 153–170.

Zhang, Z., Hirori, H., Sekiguchi, F., Shimazaki, A., Iwasaki, Y., Nakamura, T., Wakamiya, A. & Kanemitsu, Y. (2021d). Ultrastrong coupling between THz phonons and photons caused by an enhanced vacuum electric field. *Physical Review Research*, 3(3), L032021.

Zhong, S. (2019). Progress in terahertz nondestructive testing: A review. *Frontiers of Mechanical Engineering*, 14(3), 273–281.

Zhu, T., Zhou, Y., Lou, Y., Ye, H., Qiu, M., Ruan, Z. & Fan, S. (2017). Plasmonic computing of spatial differentiation. *Nature communications*, 8, 15391.

Zhuldybina, M., Ropagnol, X., Bois, C., Zednik, R. J. & Blanchard, F. (2020). Printing accuracy tracking with 2D optical microscopy and super-resolution metamaterial-assisted 1D terahertz spectroscopy. *npj Flexible Electronics*, 4(1), 1–7.